CHALMERS

Musculoskeletal Driver Model for the Steering Feedback Controller

Master's thesis in Mechanical Engineering

LYDIA SCHENK

Musculoskeletal Driver Model for the Steering Feedback Controller

LYDIA SCHENK

Musculoskeletal Driver Model for the Steering Feedback Controller
LYDIA SCHENK

Abstract

Haptic feedback from the steering wheel is one of the most important cues for driver to vehicle interaction. The right feedback is provided by ensuring that the haptic controller provides the required steering feel. Steering feel assessment and design is divided into a subjective and objective approach. The subjective approach entails experiments on the proving ground during which steering parameters can be tuned by steering experts. However, using only subjective assessment is time-consuming, costly and non-repetitive. Since there is no direct method to tune the steering feel objectively, a driver model is required to find a mathematical justification in the mechanical interaction between driver and vehicle during steering. A 3-dimensional multibody arm model is constructed to investigate the influence of driving posture on the nonlinear steering response. It was found that the torque acting in the shoulder joint is higher than in the elbow. The relation between joint torque and joint angles is linear in the shoulder, whereas nonlinearities were found in the elbow joint. Nevertheless, a change of driving posture (i.e. a change of haptic interface) leads to a different steering response. Findings from the driver model were validated by two steering experiments. Muscle contraction was measured in order to analyse the forces acting on the joints.

This study shows promise to lead to a different approach for tuning steering parameters. Further investigation and detailed experiments are required to convert this driver model into a method to tune steering feel objectively.

Acknowledgements

Lydia Schenk
Delft, August 2020

"Awareness of ignorance is the beginning of wisdom."

— *Socrates*

Nomenclature

All quantities are given in SI units and angles in radians, unless stated otherwise.

Symbol	Description
C_k	Kinematic constraints
C_x	Joint constraints
$C_{xx}\dot{x}\dot{x}$	Convective acceleration terms
F_{ext}	External force vector
F_{rack}	Steering rack force from tire dynamics
F_{lh}, F_{rh}	Forces acting on the left and right hand
F_{sw}	Applied steering wheel force
H_{adm}	Driver arm admittance transfer function
J_{arm}	Driver arm inertia
J_{str}	Steering wheel inertia
J_{tot}	Total inertia of the system
K_j	Rotational joint stiffness
M_{ij}	Mass matrix
M_{in}	Motor assist torque
M_j	Joint torque
M_{str}	Driver applied torque measured by torsion bar
P	Virtual power
Q_i	Initial joint torques
R_p	Effective pinion radius
T	Kinetic energy
T_i	Transformation matrix
T_x, T_y, T_z	Joint torque in x-, y- and z-direction
V	Potential energy
b_{arm}	Driver arm damping
b_{str}	Steering wheel damping
b_{tot}	Total damping of the system
c_{arm}	Driver arm stiffness
c_{str}	Steering wheel stiffness

Symbol	Description
c_{sw}	Steering wheel center point
g	Gravitational acceleration
h	Convective inertia terms
j	Imaginary unit
l_1,l_2,l_3,l_4,l_5	Lengths of the separate rigid bodies
m_1,m_2,m_3,m_4,m_5	Masses of the separate rigid bodies
n_{sw}	Steering wheel normal
p_{sw}	Steering wheel envelope
$q,\dot{q},\ddot{q}$	Angular position, velocity and acceleration
r_{CoM}	CoM position vector
r_{sw}	Steering wheel radius
$r_{\text{SWleft}},r_{\text{SWright}}$	Position vectors of steering wheel envelope locations
t	Time domain operator
$x,\dot{x},\ddot{x}$	CoM position, velocity and acceleration
α_1,α_4	Joint angular position in x-direction
$\beta_1,\beta_2,\beta_3,\beta_4$	Joint angular position in y-direction
γ_2,γ_3	Joint angular position in z-direction
θ_{lh},θ_{rh}	Steering wheel envelope angular positions of the hands
θ_{str}	Steering wheel angle
λ_k	Lagrange multipliers
ϕ_j	Joint angles
ϕ_{sw}	Array for steering wheel envelope
ω_e	Eigenfrequency
ω_{str}	Steering wheel angular velocity
$\mathcal{N}$	Global frame
$\mathcal{U}$	Local body-fixed upper arm frame
$\mathcal{F}$	Local body-fixed forearm frame

Table of Contents

Chapter 1

Introduction

Due to the development of advanced steering systems like Electric Power-Assisted Steering (EPAS) and Steer-by-Wire (SbW), the state-of-the-art vehicles don't require a complete mechanical steering system anymore. Therefore the driver doesn't mechanically experience the changes in applied torque, friction and damping over varying steering wheel angles as a result of the variations in road surface and velocity. One of the most important cues for driver to vehicle interaction is the haptic feedback from the steering wheel [1]. Therefore the need for a steering system with artificial haptic feedback from the steering wheel is required to provide the desired steering feel.

The steering feel is created by the haptic controller, which is a part of the steering system. The haptic controller consists of various functionalities to meet the required steering feel. One of those functionalities is basic steering assist. This is a nonlinear map between the steering wheel angle and the steering torque (Figure 1-1).
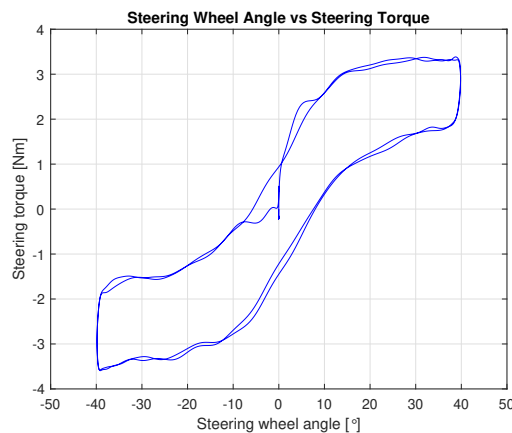
Figure 1-1: Typical on-center nonlinear relation between steering wheel angle and driver applied torque

1-1   Objective: Need for a Musculoskeletal Driver Model

Conventionally, the basic steering assist function is tuned in an empirical manner during subjective steering feel assessments on the proving ground. The typical on-center steering response is also nonlinear; such that the rate of steering torque effort reduces with increasing steering angle (Figure 1-1).

The problem under investigation is to find a mathematical justification between the nonlinear steering response and driver's musculoskeletal arm posture (constrained via wrist, elbow and shoulder joints).

1-2   Literature Research Question

With the problem statement described in the previous section, the following literature research question is defined:

What are the existing musculoskeletal driver models in literature for basic steering assist in case of a nonlinear steady-state steering response?

If such driver models don't exist in literature, the state-of-the-art steering driver models and information on the basic steering assist function are to be gathered to develop such driver models. The research question can be answered by dividing the overall question into the following two subquestions:

1. What's the mathematical explanation for the basic steering assist function in the context of driving posture?

2. What are the existing musculoskeletal driver models in literature for steering?

Additionally more information on human motion control, muscle and arm dynamics is required. Therefore the relevant information on these topics is gathered from literature as well.

Chapter 2

Steering Assist Function

The steering system consists of several software components, one of those is the haptic controller. The basic steering assist function is an important part of the the haptic controller. It provides the desired steering feel and is therefore one of the most important cues in driver to vehicle interaction [1]. The basic steering functions are (1) basic steering assist, (2) friction compensation, (3) inertia compensation and (4) active damping [2].

1. **Basic steering assist** applies motor torque as a function of the driver applied torque and the longitudinal velocity to the steering wheel and therefore reduces a driver's steering effort.

2. **Friction compensation** reduces effects of friction in the steering.

3. **Inertia compensation** is compensation based on the known inertia and derived acceleration.

4. **Active damping** is the simplest steering assist function and it is proportional to the steering speed.

Another method to divide the basic steering functions is visualized in the scheme of Figure 2-1 below [3].

2-1 Basic Steering Assist

The basic steering assist function is defined by the relation between the steering rack force and the torsion bar torque [1]. This function ensures that the driver needs to apply less torque to the steering wheel and therefore it reduces the driver's steering effort. The amount of motor assist torque varies over different steering wheel angles (SWA). The steering stiffness reduces from the on- to the off-center steering wheel angles. The amount of applied torque is also affected by velocity. At low velocity, there is a high applied torque and at high velocity there is a relatively low applied torque.
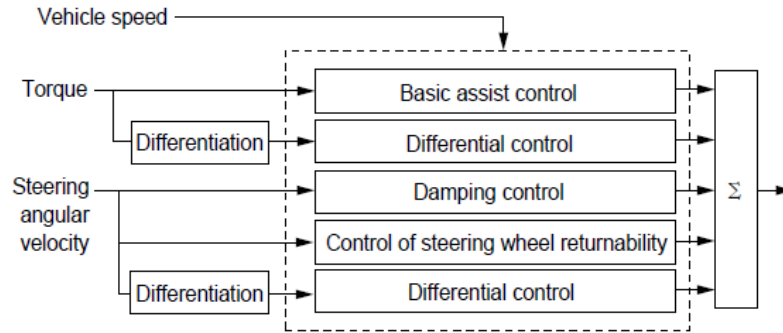
Figure 2-1: Composition of steering assist control methods [3]

2-1-1   Basic Assist Control

The basic steering assist is controlled by determining the quasi-static steering force. The motor assist torque M_{in} can be calculated using the following relation:

$$M_{in} \;=\; F_{rack} \cdot R_p - M_{str} \tag{2-1}$$

Where F_{rack} is the rack force, R_p is the effective pinion radius, and M_{str} is the torque applied by the driver on the steering wheel [3]. The rack force varies over varying velocities, with a rapid decrease in rack force F_{rack} at relatively low velocities.

2-2   Steering Feel

In the global sense, steering feel is the perception of a complex sensation while steering a vehicle [4]. The steering feel can be assessed by visualizing the vehicle test data and plotting the steering torque applied by the driver vs. the steering wheel angle, yaw rate or lateral acceleration. Steering feel has many definitions. From the objective point of view steering feel is the combined performance of steering system, chassis, tire-road contact and control system [2]. However, from a subjective point of view it is the qualitative relation between the perception of the vehicle real response and the driver steering input. From an objective point of view, steering feel can be described as a composition of three main characteristics: steering activity, steering effort and vehicle response [5, 6].

- **Steering activity** Varying steering wheel angles, steering wheel torques, longitudinal and lateral dynamics affect the steering activity. Steering wheel torques are caused by torques about the kingpin axis [7]. These torques originate from longitudinal and lateral tire forces, vertical tire forces and tire self-aligning moments.

- **Steering effort** Consists of steering friction and steering stiffness. The objective measures are the steering wheel angle and driver's applied torque.

- **Vehicle response** Time and/or phase delays in vehicle responses to a certain steering wheel input are related to the feedback torque that is experienced by the driver [8, 9].

2-2-1 Steering Feel Assessment and Design

Since the definition of steering feel depends on the point of view, steering feel assessment also has different methods for either an objective or a subjective point of view. Objective assessment is conducted by analyzing various objective metrics like steering effort, steering reversal rate, or steering entropy [2]. Subjective assessment involves human perception and is therefore often conducted using questionnaires or interviews.

In vehicles with EPAS, through steering feel assessment on the proving ground, the motor control can be tuned by experts in steering. The goal is to decrease the driver's steering effort, improve return response and improve on-centre feeling [10]. Using only objective metrics, there is no direct method to tune a vehicle's steering feel because it can result in unwanted steering feel [11]. However, using only subjective assessments is time-consuming, costly and non-repetitive.

2-2-2 Steering Tests

For the objective assessments, vehicle test data is needed. This data is obtained from steering tests. There are roughly spoken two main types of steering tests: on-center and off-center. The characteristics of the two different steering test are:

- **On-center handling** is characterized by small steering wheel angles and slow inputs. An example is steering on a highway situation.

- **Off-center handling** here large steering wheel angles and fast inputs occurr. An example is steering during a high-speed lateral control maneuver.

The transient response test and steady state cornering are other vehicle steering tests. However, these are not involved in this research.

Chapter 3

Musculoskeletal Driver Models

The first driver models were developed for aviation purposes by McRuer [12] as a result from the fast technological development from the 1950's and onwards. Other early driver models are the preview driver models which focus mainly on the control perspective using visual cues as an input for the driver model [13].

The past decades more research has been conducted on the topic of driver models. Therefore the existing driver models are investigated from three different perspectives: (1) behavioral perspective, (2) control perspective, (3) cognitive perspective [14, 15].

1. The **behavioral perspective** is investigated by looking at intradriver steering variability [16] and drivers' steering behavior [17] and the results of driver's decision making.

2. The **control perspective** is studied by McRuer [12] in the crossover model and later by Pick & Cole [18] by investigating the dynamic properties of a driver's arm holding the steering wheel. The field of study of the control perspective is also called cybernetics: describing a human in control engineering terms [19].

3. The **cognitive perspective** originates from the early research of Rasmussen's human performance models [20] where a distinction is made between skill, rule and knowledge based behavior. This concerns mainly the cognitive processess of decision making.

This literature review focusses on the driver models with a control perspective that are specifically developed for steering.

3-1   Conventional driver control perspective models

From the control perspective, the human driver is considered as a controller (or an operator) whereas the vehicle is considered as a plant. When a 'driver control perspective model' is defined as a closed-loop control system, it looks similar to the block scheme in Figure 3-1. Control theory methods can be used to describe the system.
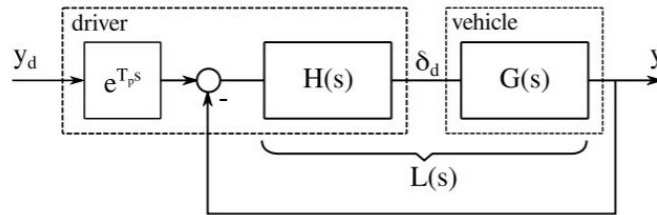
Figure 3-1: A closed-loop driver-vehicle system, where $H(s)$ is the controller, $G(s)$ is the vehicle, $L(s)$ the controller-vehicle combination, T_p the preview time, δ_d the driver steering action, and y and y_d are the actual and desired lateral positions, respectively [14].

McRuer was one of the first to come up with a driver model from a control perspective. He developed the crossover model [12] which is developed from a control point of view. The model describes a control method in which the order of control denotes the number of integrations between the human and the output of the system being controlled. The general conclusion of the crossover model is that humans can adapt their internal control behaviour to adjust their steering behavior. This can be tuned by the human brain by either basing the control behavior on position, velocity or acceleration by making use of prediction or memory. Other early driver models are the preview driver models which focus mainly on the control perspective using visual cues as an input for the driver model [13]. These models are mainly focused on the path tracking task rather than the adaptive or compensatory task. The first preview model determines steering action based on the error between the expected and desired vehicle position at a certain future moment in time [13]. More complex models making use of more than one preview point were developed later on. One of those is the MacAdam model [21] which can be used for linear systems. This model was later improved to also be able to include yaw angle error as input. Therefore the UMTRI model [22] can also be used for roads containing curves in the trajectory.

3-2 Human arm steering dynamics

When the driver models became more advanced, researchers started looking at the arm dynamics in order to understand the force interactions between driver and vehicle even better. Pick & Cole [18] contributed to this research field by investigating the dynamic properties of a driver's arm holding the steering wheel. In order to investigate the driver's steering response, a one Degree of Freedom (1 DoF) linear mass-spring-damper system is used by Pick & Cole to analyse the end-point admittance of the driver's arms [18]. Dynamics identification was done by applying random torque disturbances to the driver's arms.

The dynamic properties of the arm were also investigated by van der Helm, Schouten & de Vlugt [23, 24]. This research involved the shoulder, elbow and wrist joints and considers the 'intrinsic' and 'reflexive' dynamic arm properties [18].

- **Intrinsic properties** are generally the mass, damping and stiffness of an arm simplified as a mass-spring-damper system.

- **Reflexive properties** are caused by neural activation of the muscles via the spinal cord originated by the reflex system [18].

The steering dynamics of the human arms can be divided into translations and rotations. The rotations are caused by the rotational degrees of freedom of the joints: wrist, elbow and shoulder. The translations are caused by the translational degrees of freedom of the arms.

3-2-1 Rotational Degrees of Freedom

The rotations in the human joints are described as flexion/extension, abduction/adduction and internal/external rotation. The directions of those rotations are expressed in the 3 anatomical planes that transect the human body: sagittal, frontal and transverse plane. The anatomical planes are shown in Figure 3-2 as well as the neutral body position used to describe human body movements.
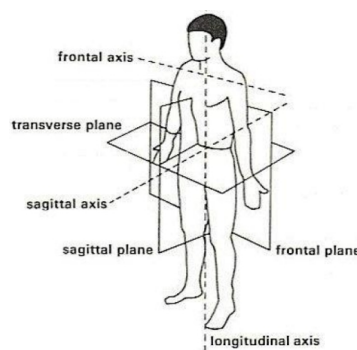

Figure 3-2: Anatomical planes of the human body [25]

1. The **shoulder** is a ball-and-socket joint between the scapula (shoulder blade) and the humerus (upper arm bone) with three rotational degrees of freedom [26]. Flexion and extension of the shoulder joint are rotations in the sagittal plane. Abduction and adduction are rotations in the frontal plane. Horizontal abduction and adduction are rotations in the transverse plane. This one ball-and-socket joint is a simplification, because in anatomy the shoulder is considered to consist of four different joints [27].

2. The **elbow** can be represented by a hinge joint between the upper arm and the forearm. Flexion and extension in the sagittal plane is the only possible rotation.

3. The **wrist** is represented best as a condyloid joint [26]. Possible rotations are flexion and extension in the sagittal plane, abduction and adduction in the frontal plane and circumdiction caused by the pivot joint in the forearm. This pivot joint makes it possible for two bones to roll over each other. This rolling movement is only possible in one direction and is a circumdiction around the forearm's axis. The only possible direction for the circumdiction is turning the thumbs towards the center of the body via the front.

3-2-2 Translational Degrees of Freedom

The translational degrees of freedom depend on the boundary conditions of the arm model. The translations are caused by the torques exerted on the bones and joints by the activated muscles or by torque disturbances originated from the environment.

3-3   Human Motor Control and Motor Learning

In order to develop a mechanical musculoskeletal arm model, it is required to understand human motion control and motor learning. An important aspect is that humans are able to rapidly adapt to disturbances from the environment (which was shown by McRuer [12]). After a disturbance in a closed-loop driver model, the arm tends to return to the desired trajectory [28]. By performing multiple trials, humans learn to control their muscles and are adapting to the disturbances. The Central Nervous System (CNS) activates the right muscles (α-activation) in the correct order with the right amount of force for the required task [29]. Internal feedforward control of the human manages to reduce errors in the task [30, 31]. This is done by activating the muscles through muscle co-contraction as well as by reflexive muscle response [32].

3-4   Muscle models

Muscles are from a technological perspective the actuators of the musculoskeletal system [29]. Each muscle can individually be seen as a biochemical plant in which chemical energy is transformed into mechanical energy. This process is controlled by neural signals from the CNS. The dynamic properties of muscles are highly nonlinear, as the muscle force depends on its length and contraction velocity. The most commonly used muscle models are the Hill- and Huxley-type models. Depending on the required detail and complexity the musculoskeletal system can be described by the basic muscle model (see Figure 3-3) or an extended version.
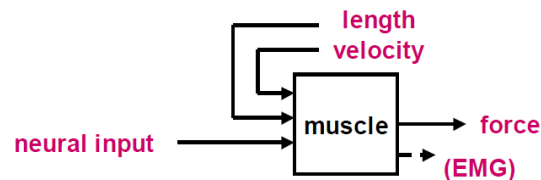

Figure 3-3: Basic muscle model [29]

The muscle model has two mechanical inputs (length and contraction velocity) and a neural input (α motor neurons) which activates the muscle [33]. The mechanical output is muscle force resulting from muscle contraction [29]. The muscle activity can be measured with Electromyography (EMG) which measures the electrical potential of the neurons that activate the muscle.

3-4-1   Hill-type muscle models

The muscle model developed in 1938 by Hill is shown in Figure 3-4. The model consists of three elements: a passive element (PE), a nonlinear contractile element (CE) and a series element (SE) [34]. The contractile element is the only element in the model that can generate energy [29]. The generated force of CE depends on its length, velocity and activation.

Hill-type muscle models are able to describe the most important nonlinear and dynamic properties of muscles. However, the underlying biochemical processes are not described by
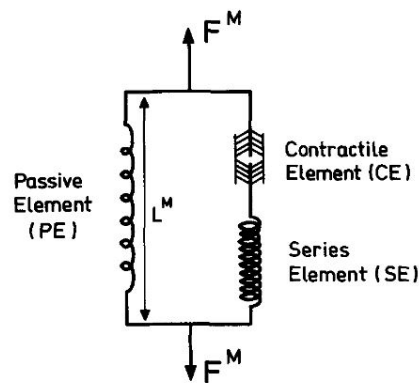
Figure 3-4: Hill-type muscle model consisting of three elements [35]

this model [29]. The Hill-type muscle model is the most widely used muscle model. This is mainly due to its simplicity and the fact that it covers the nonlinear and dynamic properties.

3-4-2 Huxley-type muscle models

Huxley-type muscle models are more complex than Hill-type muscle models as they include details about the biochemical process as well the dynamic properties of the muscles. The attachment and detachment of cross-bridges is the main process in muscle force generation (i.e. muscle contraction). Therefore the Huxley model is also sometimes referred to as cross-bridge muscle model [29]. The Huxley-type muscle model is less often used as it is more complex than the Hill-type muscle model and because in many musculoskeletal models the biochemical properties are not taken into account.

3-5 Mass-spring-damper driver models

A one Degree of Freedom (1 DoF) linear mass-spring-damper system is used by Pick & Cole to analyze the end-point admittance of the driver's arms [18]. This model was created in order to investigate the driver's steering response (Figure 3-5) and in particular the torque to angle transfer function. Dynamics identification was done by applying random torque disturbances to the driver's arms. Muscle co-contraction was found to increase the arm stiffness and damping [18].

The model of Pick & Cole [18] was later extended with an improved model of the intrinsic muscle dynamics [36]. Previously intrinsic muscle dynamics were thought to be dominated by a stiffness term [37]. However, Hoult & Cole found that the intrinsic muscle dynamics are dominated by a damping term at low frequencies [38, 39]. It is not surprising that researchers did not discover this before, because it is relatively difficult to experimentally identify the separate contributions of the intrinsic and reflexive muscle properties. Katzourakis et al. [40] developed a second-order inertia-spring-damper model. The goal was to analyze human driver's arm admittance during real world test-track driving (Figure 3-6).
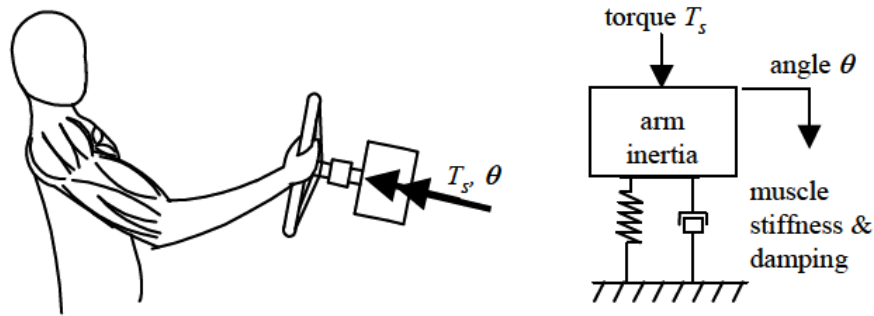
Figure 3-5: Experiment to measure torque to angle transfer function of a driver's arms [33] [18]
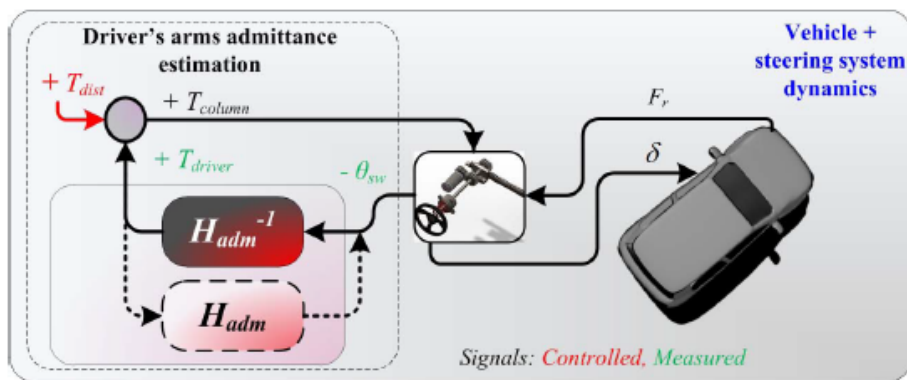

Figure 3-6: Block scheme for estimating the admittance H_{adm} from T_{driver} to θ_{sw} [40]

The focus of the experiment was curve negotiation behavior. The results showed that during cornering the arm stiffness increases. This model payed special attention to alpha-gamma co-activation in the muscles.

3-6   Neuromusculoskeletal models

Sentouh et al. [41] developed a driver model including steering torque feedback. This model does not include reflex dynamics explicitly. However, the model does include a time delay to indicate the human processing delay. The driver model is divided into two levels: preview tracking and compensatory tracking [42]. This model takes into account the driver's sensory dynamics and their effects on steering control. De Vlugt et al. [43] developed a neuromusculoskeletal (NMS) model to estimate intrinsic and reflexive properties of the arm muscles. Initially a haptic manipulator experiment was conducted to estimate the admittance of the human arm. After EMG measurement analysis, the intrinsic and reflexive properties of the arm were estimated. Abbink developed a driver model for a haptic gas pedal in a car following situation [44]. In this experiment the admittance of the ankle and foot was determined during a car-following task. The principle behind this research was that the driver's visual feedback response was separated from the driver's response to designed haptic feedback.

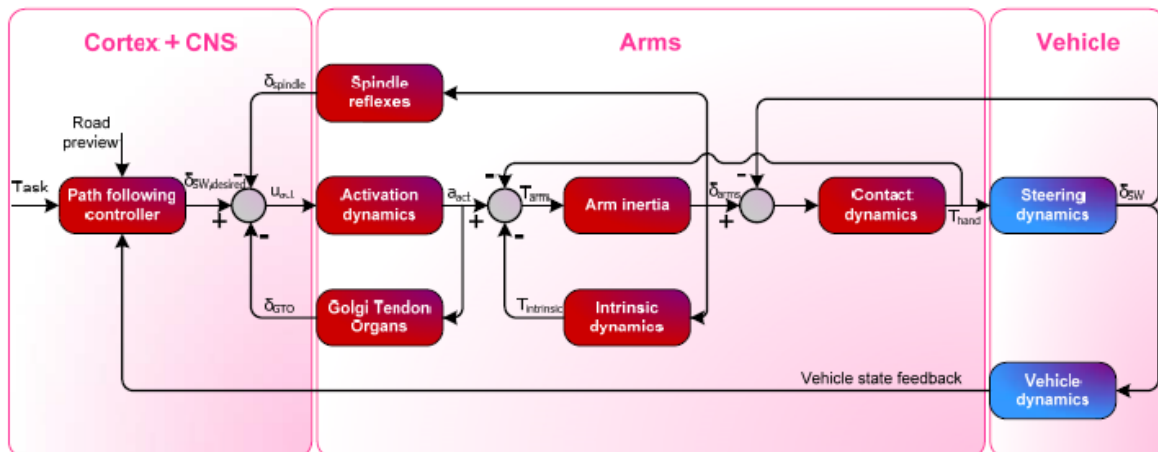Droogendijk [45] adjusted the neuromuscular models of de Vlugt [43] and Abbink [46] (see

Figure 3-7: The Abbink [44] driver model building on NMS arm models by de Vlugt [43] merged by Droogendijk [45].

Figure 3-7) to make the new model applicable for large SWA due to the adaptability to changes in muscle length. Also the model was developed to convert the desired steering angle to the desired muscle force to achieve this angle.

3-7   The Delft Shoulder and Elbow Model

The Delft Shoulder and Elbow Model (DSEM) is a three-dimensional finite-element musculoskeletal model of the upper arm [27, 47]. It considers the shoulder, elbow and many details about the four joints in the shoulder. This model is not applicable to musculoskeletal driver models since it is mainly focusing on the anatomical resemblance of the shoulder and contains therefore irrelevant details for the task.

3-8   Human sensory dynamics involved in steering

Another selection criterion that can be used for driver models is by selecting on the sensory dynamics interaction methods with the environment. This way we can distinguish between the following senses: (1) visual senses, (2) vestibular organ, (3) somatosensory system [29].

1. The **Visual senses** are in case of a human driver the eyes [12, 48]. Drivers can analyze the road curvature and other road characteristics based upon the sensory feedback of the eyes.

2. The **Vestibular organ** regulates balance and spatial orientation for movement coordination. Therefore it determines motion perception and influences driver comfort during driving [49].

3. The **Somatosensory system** informs the driver about environmental objects like the haptic feedback from the steering wheel (tactile feedback) as well as the location and

movement of one's own bodyparts (proprioception) [49]. Tactile feedback is sensed by mechanoreceptors, proprioceptive feedback by golgi tendon organs (GTO) and muscle spindles [29].

3-9   A linear approach to nonlinear modelling

The NMS model of Pick & Cole [18] describes only linear vehicle dynamics. In reality the vehicle dynamics are nonlinear and there is noise. Cole has therefore proposed an approach in which the driver can be modelled as a set of linear models [33]. Each linear model is valid on a specific operating point defined using the tire slip angles. Cole makes a distinction in describing novice and expert drivers as is shown in Figure 3-8. The model is based on lateral axle force F_y linearization.
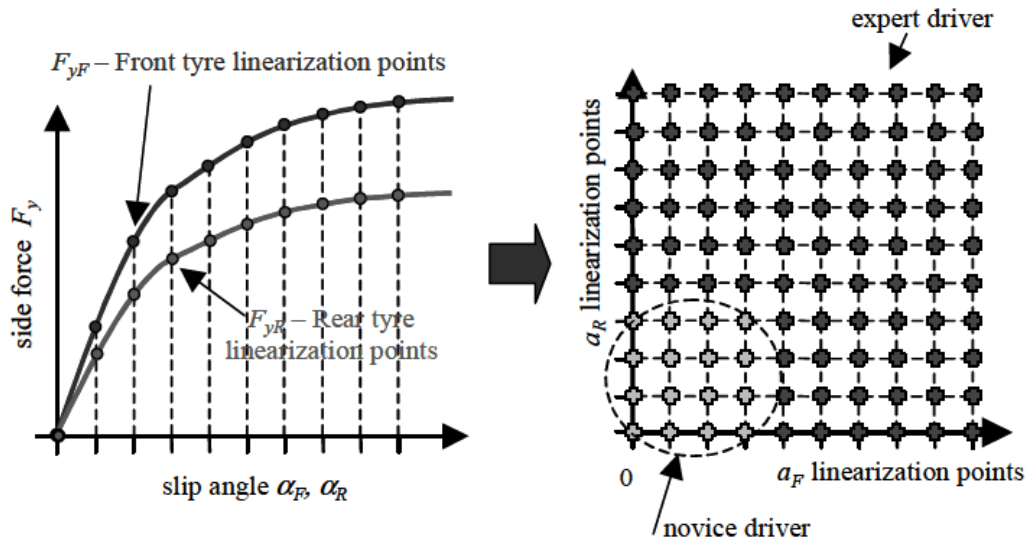

Figure 3-8: The driver's internal model of the nonlinear vehicle can be represented as a combination of linear models [33].

Cole emphasizes that a novice driver could have a smaller number of linear models over a small range of slip angles compared to an experienced driver. An experienced driver might have a larger number of linear models over the full range of slip angles.

Chapter 4

Thesis paper

The main report of this thesis is written in the form of a paper, with additional information in separate Appendices. The paper in this chapter states the driver model equations and the experimental investigation. Results of driver model and experiment are compared and the conclusions are listed. More elaborate information on the separate sections can be found in the Appendix.

Musculoskeletal Driver Model for the Steering Feedback Controller

Abstract: This paper aims to find a mathematical justification for the non-linear steady state steering feedback response as a function of drivers' musculoskeletal arm (or driving) posture. The experiments show, that the different arm postures result in a change in characteristics (in terms of effective arm inertia and stiffness) over different steering wheel angles. A 3-dimensional quasi-static driver musculoskeletal model considering wrist, elbow and shoulder joints is developed for posture analysis. The torque acting in the shoulder joint is higher than in the elbow. The relation between the joint torque and joint angle is linear in the shoulder, whereas the non-linearity occurs in the elbow joint. The simulation results are qualitatively compared with the experimental results.

1. Introduction

In the state-of-the-art steering systems, the steering feedback is manipulated by the haptic feedback controller. One of the most important cues in the driver-vehicle interaction is the haptic feedback from the steering wheel [1]. It provides the driver with a desired part of the steering feel. This steering feedback is dependent on the haptic control strategy [2,3], which further consists of various software functions. One of them is the basic steering assist function.

1.1. Basic steering assist function

The basic steering assist function creates a non-linear on-center steering response, refer Figure 1. The response is defined in terms of steering torque vs. steering wheel angle (SWA). This non-linear response is developed objectively and subjectively in an empirical manner using simulation or driving simulator experiments [4].

As a consequence, the typical on-center steering response (achieved for a desired steering feedback) is non-linear; such that the steering torque effort reduces (Figure 1) at a given vehicle speed. During this operational range (i.e. within $3 - 4\,\text{m/s}^2$ vehicle lateral acceleration), the steering rack force generated by tire forces and self-aligning moments acting on the steering rack, behaves approximately linear over steering angle (or equivalently rack displacement), refer Figure 2. The vehicle lateral acceleration behaves almost linear over steering wheel angle as can be seen in Figure 2. This implies that the non-linearity is not contributed by the front axle tire forces or moments, but rather the basic steering assist function. Therefore the research question is: How is the non-linear (on-center) steering response related to the drivers' musculoskeletal arm posture, constrained via the hand, elbow and shoulder joints?

1.2. Conventional control perspective driver models

McRuer was one of the first to come up with a driver model from a control perspective. The crossover model [5] describes a control method in which the order of control denotes the number of integrations between the human and the output of the system being controlled. The general conclusion of the crossover model is that humans can adapt their internal control behaviour to adjust their steering behavior. The human brain adapts by either basing the control behavior on position, velocity or acceleration by making use of prediction or memory. Other models are the preview driver models
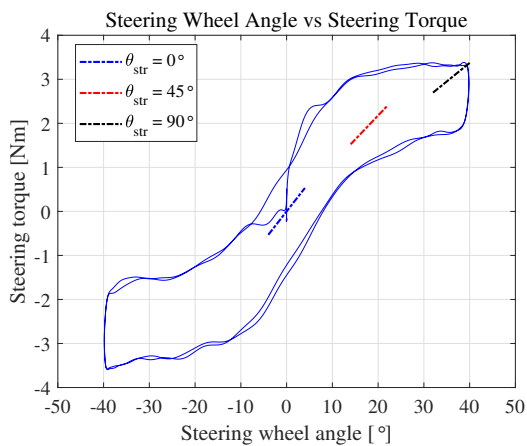
Figure 1. Typical on-center response, exhibiting the software developed non-linear relation between the steering wheel angle and the steering torque.
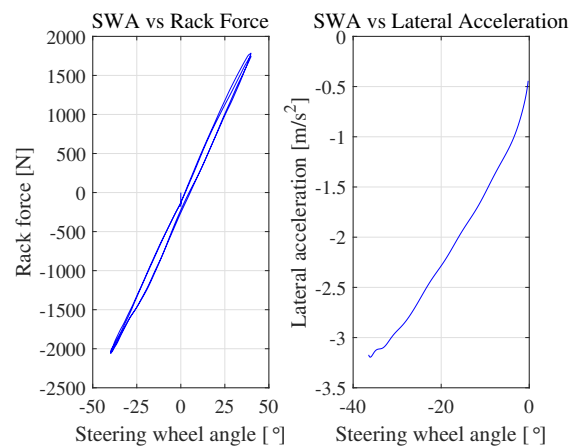

Figure 2. Linear relation between the steering wheel angle and the steering rack force as well as the lateral acceleration.

which focus mainly on using visual cues as an input for the driver model [6]. These models are mainly focused on the path tracking task rather than the haptic feedback task.

In order to investigate the driver's steering response, one Degree of Freedom linear mass-spring-damper system is used by Pick & Cole [7,8] to analyse the end-point admittance of the driver's arms. The system identification is done by applying random torque disturbances to the driver's arms. Muscle co-contraction is found to increase the arm stiffness and damping [7]. This model [7] has later been extended with an improved model of the intrinsic muscle dynamics [9]. Previously intrinsic muscle dynamics are thought to be dominated by a stiffness term [8]. However, Hoult & Cole found that the intrinsic muscle dynamics are dominated by a damping term at low frequencies [10].

1.3. Neuromusculoskeletal driver models

Sentouh et al. [11] propose a driver model including steering torque feedback. This model does not include reflex dynamics explicitly. However, the model does include a time delay to indicate the neuro-muscular processing delay. The driver model is divided into two levels: preview tracking and compensatory tracking [12]. This model takes into account the driver's sensory dynamics and their effects on steering control. De Vlugt et al. [13,14] developed a neuromusculoskeletal (NMS) model to estimate intrinsic and reflexive properties of the arm muscles. After electromyography (EMG) measurement analysis, the dynamic properties of the arm were estimated. These musculoskeletal (driver) models considered the vehicle dynamics to be linear. Katzourakis et al. [15] adjusted the neuromuscular models of de Vlugt [16] and Abbink [17,18] to make the new model applicable for large steering wheel angles due to the adaptability to changes in muscle length. Also the model was developed to convert the desired steering angle to the desired muscle force to achieve this angle.

However, none of these models consider the relation between the non-linear steering response and the drivers' musculoskeletal arm posture. In [15], the variation in human arm end-point admittance as a function of the road curvature is analyzed, whereas the role of driving posture is not investigated. Therefore the main contribution of this research is to find out what causes a desired steering response when investigating the steering posture from a cybernetics perspective (i.e. describing the human in control engineering terms) [19]. The hypothesis is that the musculoskeletal driver's arm posture could be responsible for the given steering response. A 3-dimensional driver model was developed to analyze joint torques and a real-time experiment was conducted for comparison of qualitative trends in data. Simulation and experimental results are analyzed to conclude on the hypothesis.

2. Musculoskeletal driver model

Typical neuro-muscular steering models show promise to understand the effect of non-linear driver arm mechanics (combination of inertia, spring and damper elements). For a comprehensive investigation of the driving posture, a model considering 3-dimensional arm mechanics was developed. Validation is ensured by means of a real-time experiment.

2.1. 3-Dimensional model characteristics

In order to obtain the relation between the arm posture and the non-linear steering response, the joint torques and angles should be known. Hence, a 3-dimensional model of the human posture is developed. The joint angles for different steering angular positions are determined, and finally used to compute the joint torques. The following assumptions are considered for the model:

- A quasi-static model is implemented to ensure a straightforward unique solution, because steady-state behavior is investigated.
- Shoulder and elbow joints are considered, neglecting wrist because of its negligible influence in terms of displacement and force on the overall system.
- In the shoulder joints only x- and y-rotation are considered. This ensures sufficient reachability while not including extra degrees of freedom (resulting in a set of non-unique solutions) and realizing a less computationally demanding model.
- The shoulder joint rotation in x-direction is fixed to a constant value to ensure a unique quasi-static solution, because these angles are expected to vary the least (compared to the other joint angles) during steering.
- The elbow joints are limited to moving in y- and z-direction only to ensure a unique solution while retaining the required reachability on the steering wheel trajectory.
- The mass between the shoulders is fixed in x-, y- and z-direction at the center of mass.
- The endpoints of the forearms (i.e. the hands) are fixed to the steering wheel trajectory in a ten-to-three steering posture.
- The upper arm is constrained which prevents independent movement with respect to the mass between the shoulders.
- Forearm and upper arm are constrained so they are not allowed to move independent from each other.
- The centers of mass are positioned according to anthropometric standards [20] and therefore not located exactly in the middle of each body. All other parameters describing limb lengths and masses follow the same anthropometric standards.

2.2. Multibody arm model

Each arm consists of two rigid bodies connected at the shoulders by a mass representing the head, neck and shoulders. This adds up to a total of five bodies connected by eight hinge joints as shown in Figure 3.

The gravity is assumed to work in the negative z-direction. The independent coordinates $\phi_j = (\alpha_1, \alpha_4, \beta_1, \beta_2, \beta_3, \beta_4, \gamma_2, \gamma_3)$ and their time derivatives are used to describe the rotations. In order to express the Euler angles (xyz) α, β, and γ the rotation matrices R_α, R_β, and R_γ can be written as follows.

$$R_\alpha = \begin{bmatrix} 1 & 0 & 0 \\ 0 & cos\alpha & -sin\alpha \\ 0 & sin\alpha & cos\alpha \end{bmatrix}, R_\beta = \begin{bmatrix} cos\beta & 0 & sin\beta \\ 0 & 1 & 0 \\ -sin\beta & 0 & cos\beta \end{bmatrix}, R_\gamma = \begin{bmatrix} cos\gamma & -sin\gamma & 0 \\ sin\gamma & cos\gamma & 0 \\ 0 & 0 & 1 \end{bmatrix} \tag{1}$$
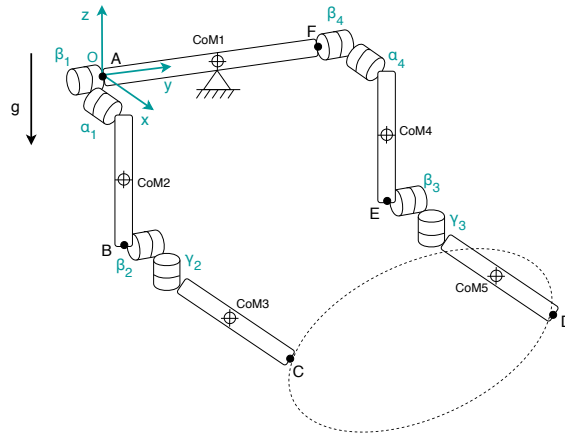
Figure 3. Free body diagram of the human arms

2.3. Joint and CoM position vectors

The locations of the five bodies can be described by the corresponding CoM position vectors numbered 1 to 5. The hinge locations are described by the joint position vectors labeled in alphabetical order from A to F, refer Figure 3. Each position vector contains an x-, y- and z- component. The joint and CoM position vectors are expressed in the inertial frame making use of local body-fixed frames shown in the example of Figure 4. The position $^{\mathcal{N}}x_P$ of point P expressed in the inertial $\mathcal{N}$-frame is expressed as stated below.
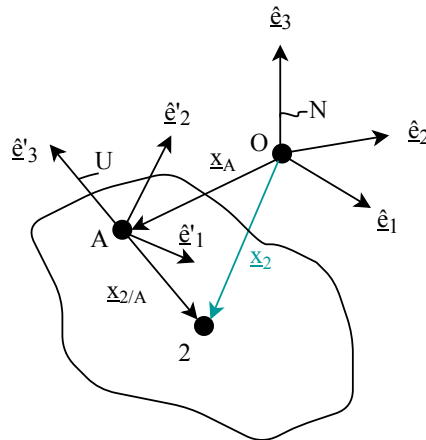
Figure 4. Sketch of the right upper arm containing point A, center of mass 2, body-fixed frame $\mathcal{U}$ and the point's position vectors with respect to the origin O of a coordinate system associated with inertial $\mathcal{N}$-frame.

$$
\begin{aligned}
^{\mathcal{N}}\boldsymbol{x}_1 &= {}^{\mathcal{N}}\boldsymbol{x}_{1/O} \\
^{\mathcal{N}}\boldsymbol{x}_2 &= {}^{\mathcal{N}}\boldsymbol{x}_A + {}^{\mathcal{N}}\boldsymbol{x}_{2/A} \\
&= {}^{\mathcal{N}}\boldsymbol{x}_A + {}^{\mathcal{N}}\mathbf{R}_{\mathcal{U}}\,{}^{\mathcal{U}}\boldsymbol{x}_{2/A}
\end{aligned} \tag{2}
$$

$$
\begin{aligned}
^{\mathcal{N}}\boldsymbol{x}_3 &= {}^{\mathcal{N}}\boldsymbol{x}_B + {}^{\mathcal{N}}\boldsymbol{x}_{3/B} \\
&= {}^{\mathcal{N}}\boldsymbol{x}_B + {}^{\mathcal{N}}\mathbf{R}_{\mathcal{F}}\,{}^{\mathcal{F}}\boldsymbol{x}_{3/B} \\
&= {}^{\mathcal{N}}\boldsymbol{x}_B + {}^{\mathcal{N}}\mathbf{R}_{\mathcal{U}}\,{}^{\mathcal{U}}\mathbf{R}_{\mathcal{F}}\,{}^{\mathcal{F}}\boldsymbol{x}_{3/B}
\end{aligned} \tag{3}
$$

These equations are for the right arm describing bodies 1, 2 and 3. Where ${}^{\mathcal{N}}\mathbf{R}_{\mathcal{U}}$ is the rotation matrix in terms of the body-fixed frame $\mathcal{U}$ expressed in the inertial frame $\mathcal{N}$. The initial positions in the local upper-arm $\mathcal{U}$-frame and forearm $\mathcal{F}$-frame are expressed in the global reference frame $\mathcal{N}$. In order to describe the motion of the right upper arm ${}^{\mathcal{N}}x_2$, the local position vector of the CoM of body 2 is rotated from body 1 to body 2 using the rotation matrices connected to the global $\mathcal{N}$-frame. For the position vector ${}^{\mathcal{N}}x_3$ describing the forearm, the body-fixed frame of the forearm is affected by the rotations of the upper arm (the $\mathcal{U}$-frame) as well as the rotation of its own fixed body frame $\mathcal{F}$ around the y- and z-axis with respect to the inertial frame $\mathcal{N}$. The same method is applied to the left arm (bodies 4 and 5) resulting in the rotation matrices for the individual frame mappings (see Appendix A-1). For consistency, all motions are expressed in the global $\mathcal{N}$-frame. This results in the following position vectors for the initial position considering upper arm (body 2) vertical in negative z-direction and forearm (body 3) horizontal in positive x-direction. These vectors are only describing the CoM positions of the right arm.

$$
{}^{\mathcal{N}}x_1 = \begin{bmatrix} 0 \\ \frac{l_1}{2} \\ 0 \end{bmatrix}
$$

$$
{}^{\mathcal{N}}x_2 = {}^{\mathcal{N}}x_A + R_{\alpha_1} R_{\beta_1} \begin{bmatrix} 0 \\ 0 \\ -\mathrm{cg}_2 \end{bmatrix} \tag{4}
$$

$$
{}^{\mathcal{N}}x_3 = {}^{\mathcal{N}}x_B + R_{\alpha_1} R_{\beta_1} R_{\gamma_2} R_{\beta_2} \begin{bmatrix} \mathrm{cg}_3 \\ 0 \\ 0 \end{bmatrix}
$$

The left end of body 1 (point A) is fixed in the origin, and therefore the position vector ${}^{\mathcal{N}}x_A$ is zero for all xyz. The vectors describing the joint positions of the right arm are stated below.

$$
{}^{\mathcal{N}}x_A = \mathbf{0}
$$

$$
{}^{\mathcal{N}}x_B = {}^{\mathcal{N}}x_A + R_{\alpha_1} R_{\beta_1} \begin{bmatrix} 0 \\ 0 \\ -l_2 \end{bmatrix} \tag{5}
$$

$$
{}^{\mathcal{N}}x_C = {}^{\mathcal{N}}x_B + R_{\alpha_1} R_{\beta_1} R_{\gamma_2} R_{\beta_2} \begin{bmatrix} l_3 \\ 0 \\ 0 \end{bmatrix}
$$

An identical process was conducted for the left arm, resulting in the following complete set of joint and CoM position vectors.

$$r_{CoM1} = \begin{bmatrix} 0 \\ \frac{l_1}{2} \\ 0 \end{bmatrix}$$

$$r_{CoM2} = \begin{bmatrix} 0 \\ 0 \\ 0 \end{bmatrix} + R_{\alpha_1} R_{\beta_1} \begin{bmatrix} 0 \\ 0 \\ -cg_2 \end{bmatrix}$$

$$r_{CoM3} = \begin{bmatrix} 0 \\ 0 \\ 0 \end{bmatrix} + R_{\alpha_1} R_{\beta_1} \begin{bmatrix} 0 \\ 0 \\ -l_2 \end{bmatrix} + R_{\alpha_1} R_{\beta_1} R_{\gamma_2} R_{\beta_2} \begin{bmatrix} cg_3 \\ 0 \\ 0 \end{bmatrix} \tag{6}$$

$$r_{CoM4} = \begin{bmatrix} 0 \\ l_1 \\ 0 \end{bmatrix} + R_{\alpha_4} R_{\beta_4} \begin{bmatrix} 0 \\ 0 \\ -cg_4 \end{bmatrix}$$

$$r_{CoM5} = \begin{bmatrix} 0 \\ l_1 \\ 0 \end{bmatrix} + R_{\alpha_4} R_{\beta_4} \begin{bmatrix} 0 \\ 0 \\ -l_4 \end{bmatrix} + R_{\alpha_4} R_{\beta_4} R_{\gamma_3} R_{\beta_3} \begin{bmatrix} cg_5 \\ 0 \\ 0 \end{bmatrix}$$

$$r_A = \begin{bmatrix} 0 \\ 0 \\ 0 \end{bmatrix}$$

$$r_B = \begin{bmatrix} 0 \\ 0 \\ 0 \end{bmatrix} + R_{\alpha_1} R_{\beta_1} \begin{bmatrix} 0 \\ 0 \\ -l_2 \end{bmatrix}$$

$$r_C = \begin{bmatrix} 0 \\ 0 \\ 0 \end{bmatrix} + R_{\alpha_1} R_{\beta_1} \begin{bmatrix} 0 \\ 0 \\ -l_2 \end{bmatrix} + R_{\alpha_1} R_{\beta_1} R_{\gamma_2} R_{\beta_2} \begin{bmatrix} l_3 \\ 0 \\ 0 \end{bmatrix}$$

$$r_D = \begin{bmatrix} 0 \\ l_1 \\ 0 \end{bmatrix} + R_{\alpha_4} R_{\beta_4} \begin{bmatrix} 0 \\ 0 \\ -l_4 \end{bmatrix} + R_{\alpha_4} R_{\beta_4} R_{\gamma_3} R_{\beta_3} \begin{bmatrix} l_5 \\ 0 \\ 0 \end{bmatrix} \tag{7}$$

$$r_E = \begin{bmatrix} 0 \\ l_1 \\ 0 \end{bmatrix} + R_{\alpha_4} R_{\beta_4} \begin{bmatrix} 0 \\ 0 \\ -l_4 \end{bmatrix}$$

$$r_F = \begin{bmatrix} 0 \\ l_1 \\ 0 \end{bmatrix}$$

Now the expressions for the CoM coordinates of the five bodies, $x_i = (x_1, y_1, z_1 \; ... \; x_5, y_5, z_5)$, expressed in terms of the system parameters and angles of rotation can be constructed (see Appendix A-2).

2.4. Generating the mass and force matrices

The eight initial hinge torques, which are the generalized forces $Q = (M_\alpha, M_\beta, M_\gamma)$ for the initial configuration (all angles zero) can be determined using the TMT-method [21] together with the eight generalized coordinates $q = (\alpha_1, \alpha_4, \beta_1, \beta_2, \beta_3, \beta_4, \gamma_2, \gamma_3)$. The mass matrix M_{ij} and external force vector f_i are defined as follows.

$$M_{ij} = \text{diag} \left(\begin{bmatrix} m_1 & m_1 & m_1 & ... & m_5 & m_5 & m_5 \end{bmatrix} \right) \tag{8}$$

$$f_i = \begin{bmatrix} 0 & 0 & -m_1 g & \dots & 0 & 0 & -m_5 g \end{bmatrix}^\mathrm{T} \tag{9}$$

2.5. TMT-method

The CoM-based mass term M_{ij} is rewritten into the generalized mass matrix $\bar{M}_{ij}$ [21].

$$\bar{M}_{ij} = T_i^T M_{ij} T_i \tag{10}$$

T_i is the transformation matrix which is the Jacobian matrix $x_{i,k}$. Assuming static equilibrium (the sum of the forces is zero) this results in the following relation for the EoM.

$$\begin{aligned} \bar{M}_{ij} \ddot{q}_j &= T_i^T \left(f_i - M_{ij} T_{i,j} \dot{q}_j \dot{q}_i \right) - Q_i \\ 0 &= T_i^T \left(f_i - M_{ij} T_{i,j} \dot{q}_j \dot{q}_i \right) - Q_i \end{aligned} \tag{11}$$

With Q_i representing the generalized forces that were introduced by the generalized coordinates. So in this case Q_i represents the eight hinge torques.

$$Q_i = T_i^T \left(f_i - M_{ij} T_{i,j} \dot{q}_j \dot{q}_i \right) \tag{12}$$

Solving the equation for the initial configuration, this results in the following values for the eight hinge torques.

$$\boldsymbol{Q} = \begin{bmatrix} Q_{\alpha_1} & Q_{\alpha_4} & Q_{\beta_1} & Q_{\beta_2} & Q_{\beta_3} & Q_{\beta_4} & Q_{\gamma_2} & Q_{\gamma_3} \end{bmatrix}^\mathrm{T} \tag{13}$$

2.6. Energy and Lagrange equations of motion

The potential energy V and the kinetic energy T of the masses in motion are:

$$\begin{aligned} V &= mgh \\ T &= \tfrac{1}{2} \dot{q}_k \bar{M}_{kl} \dot{q}_l, \quad i,j = 1...n, \quad k,l = 1...d \end{aligned} \tag{14}$$

For a conservative system where all forces can be derived from a potential energy function the sum of the potential and kinetic energy is constant.

$$T + V = \text{constant} \tag{15}$$

The equations of motion are then obtained by differentiating the energy equation with respect to the CoM coordinate displacements $dx_i = \dot{x}_i \, dt$.

$$-\frac{\partial V}{\partial x_i} + F_i = \frac{\mathrm{d}}{\mathrm{d}t} \left(\frac{\partial T}{\partial \dot{x}_i} \right) \tag{16}$$

The velocities of the CoM coordinates in terms of the generalized coordinates and their rates are stated below.

$$\dot{x}_i = \frac{\partial x_i}{\partial q_j} \dot{q}_j \quad i,j = 1...n, \quad j = 1...d \tag{17}$$

Rewriting these terms eventually results in Lagrange's equations of motion.

$$Q_j = \frac{\mathrm{d}}{\mathrm{d}t} \left(\frac{\partial T}{\partial \dot{q}_j} \right) - \frac{\partial T}{\partial q_j} + \frac{\partial V}{\partial q_j} \quad j = 1...d \tag{18}$$

With Q_j representing the generalized forces that were introduced by the generalized coordinates. The CoM-based mass terms M_{ij} and mass matrix $\mathbf{M}$ can be rewritten into the generalized mass matrix $\bar{\mathbf{M}}$.

$$\bar{\mathbf{M}} = \mathbf{T}^T \mathbf{M} \mathbf{T} \tag{19}$$

Where $\mathbf{T}$ is the transformation matrix which is equal to the Jacobian matrix $x_{i,k}$. Substituting the expression for the kinetic energy in terms of the generalized mass matrix for the generalized inertia forces results in:

$$
\begin{aligned}
\frac{\mathrm{d}}{\mathrm{d}t}\left(\frac{\partial T}{\partial \dot{q}_i}\right) - \frac{\partial T}{\partial q_i} &= \frac{\mathrm{d}}{\mathrm{d}t}\left(\bar{M}_{ij}\dot{q}_j\right) - \tfrac{1}{2}\bar{M}_{jk,i}\dot{q}_j\dot{q}_k \\
&= \bar{M}_{ij}\ddot{q}_j + \bar{M}_{ij,k}\dot{q}_j\dot{q}_k - \tfrac{1}{2}\bar{M}_{jk,i}\dot{q}_j\dot{q}_k \\
&= \bar{M}_{ij}\ddot{q}_j + \left(\bar{M}_{ij,k} - \tfrac{1}{2}\bar{M}_{jk,i}\right)\dot{q}_j\dot{q}_k \\
&= \bar{M}_{ij}\ddot{q}_j + h_i\left(q_j, \dot{q}_j\right)
\end{aligned}
\tag{20}
$$

In the above equation, h_i represents the convective inertia terms as described below.

$$h_i\left(q_j, \dot{q}_j\right) = \left(\bar{M}_{ij,k} - \tfrac{1}{2}\bar{M}_{jk,i}\right)\dot{q}_j\dot{q}_k \tag{21}$$

The constrained equations of motion derived using the method of Lagrange, including some additional kinematic constraints C_k are stated as:

$$
\begin{bmatrix} \bar{M}_{ij} & C_{k,i} \\ C_{k,j} & 0_{kk} \end{bmatrix}
\begin{bmatrix} \ddot{q}_j \\ \lambda_k \end{bmatrix}
=
\begin{bmatrix} Q_i - \frac{\partial V}{\partial q_i} - h_i \\ -C_{k,ij}\dot{q}_i\dot{q}_j - 2C_{k,it}\dot{q}_i - C_{k,tt} \end{bmatrix},
\tag{22}
$$
$$i, j = 1...d, \ \ k = 1...m$$

Where t refers to a partial derivative to time. Therefore it is now possible to initiate motions which vary over time.

2.7. Constraint equations

The geometrical constraint vector $\mathbf{C}_x$ contains three constraints with each an x, y and z component. The first two constraints are the hinges in the shoulder and elbow joints preventing independent motion between the bodies. The upper arm (mass 2) is connected to the shoulder mass (mass 1) and the forearm (mass 3) is constrained from moving separately from the upper arm (mass 2). The third constraint is the position of the right hand fixed on the steering wheel envelope in x, y and z direction. The same can be done for the left arm, which adds three more constraints resulting in a total of six constraint equations. The constraint equations are expressed in the global $\mathcal{N}$-frame and are given below.

$$
\begin{aligned}
\mathbf{x}_{A/1} &= \mathbf{x}_{A/2} \\
\mathbf{x}_{B/2} &= \mathbf{x}_{B/3} \\
\mathbf{x}_{C/3} &= \mathbf{x}_{C/\text{SWright}} \\
\mathbf{x}_{F/1} &= \mathbf{x}_{F/4} \\
\mathbf{x}_{E/4} &= \mathbf{x}_{E/5} \\
\mathbf{x}_{D/5} &= \mathbf{x}_{D/\text{SWleft}}
\end{aligned}
\tag{23}
$$

The notation $\mathbf{x}_{A/1}$ is used to specify the position vector (containing an x-, y- and z-component) of point A starting from the Center of Mass (CoM) of body 1.

$$
\begin{aligned}
x_1 + x_{A/CoM1} &= x_2 - x_{CoM2/A} \\
x_2 + x_{B/CoM2} &= x_3 - x_{CoM3/B} \\
x_3 + x_{C/CoM3} &= x_{SWright} \\
x_1 + x_{F/CoM1} &= x_4 - x_{CoM4/F} \\
x_4 + x_{E/CoM4} &= x_5 - x_{CoM5/E} \\
x_5 + x_{D/CoM5} &= x_{SWleft}
\end{aligned}
\tag{24}
$$

The terms $x_{SWright}$ and x_{SWleft} are representing the position vectors of the locations on the steering wheel envelope where the left and right hand are positioned for a certain θ_{str}. These position vectors are derived in section 2-8.

$$
\begin{aligned}
x_1 + (x_A + x_1) &= x_2 - (x_{CoM2} - x_A) \\
x_2 + (x_B + x_2) &= x_3 - (x_{CoM3} - x_B) \\
x_3 + (x_{CoM3} - x_B) &= x_{SWright} \\
x_1 + (x_F + x_1) &= x_4 - (x_{CoM4} - x_F) \\
x_4 + (x_E + x_4) &= x_5 - (x_{CoM5} - x_E) \\
x_5 + (x_{CoM5} - x_E) &= x_{SWleft}
\end{aligned}
\tag{25}
$$

Rewriting the terms results in the following set of constraint equations. These six constraint equations each contain an x-, y- and z-component and are all equal to zero.

$$
\begin{aligned}
x_2 - x_{CoM2} &= 0 \\
x_3 - x_{CoM3} &= 0 \\
x_3 + x_{CoM3} - x_B - x_{SWright} &= 0 \\
x_4 - x_{CoM4} &= 0 \\
x_5 - x_{CoM5} &= 0 \\
x_5 + x_{CoM5} - x_E - x_{SWleft} &= 0
\end{aligned}
\tag{26}
$$

The joint constraints combined in one vector C_x are:

$$
C_x = \begin{bmatrix}
x_2 - r_{CoM2}(x) \\
y_2 - r_{CoM2}(y) \\
z_2 - r_{CoM2}(z) \\
x_3 - r_{CoM3}(x) \\
y_3 - r_{CoM3}(y) \\
z_3 - r_{CoM3}(z) \\
x_3 + r_{CoM3}(x) - x_B - r_{SWright}(x) \\
y_3 + r_{CoM3}(y) - y_B - r_{SWright}(y) \\
z_3 + r_{CoM3}(x) - z_B - r_{SWright}(z) \\
x_4 - r_{CoM4}(x) \\
y_4 - r_{CoM4}(y) \\
z_4 - r_{CoM4}(z) \\
x_5 - r_{CoM5}(x) \\
y_5 - r_{CoM5}(y) \\
z_5 - r_{CoM5}(z) \\
x_5 + r_{CoM5}(x) - x_E - r_{SWleft}(x) \\
y_5 + r_{CoM5}(y) - y_E - r_{SWleft}(y) \\
z_5 + r_{CoM5}(x) - z_E - r_{SWleft}(z)
\end{bmatrix} = 0
\tag{27}
$$

Substituting the joint and CoM position vectors, this results in the constraint vector (see Appendix A-3).

The convective acceleration terms $C_{xx}\dot{x}\dot{x}$ are calculated by computing their partial derivatives and multiplying with the state derivative vector $\dot{x}_i$ (both were done twice). The partial derivatives are calculated using the Jacobian. When incorporating all constraints in the model, the 3-dimensional multibody driver model from Figure 5 was developed.
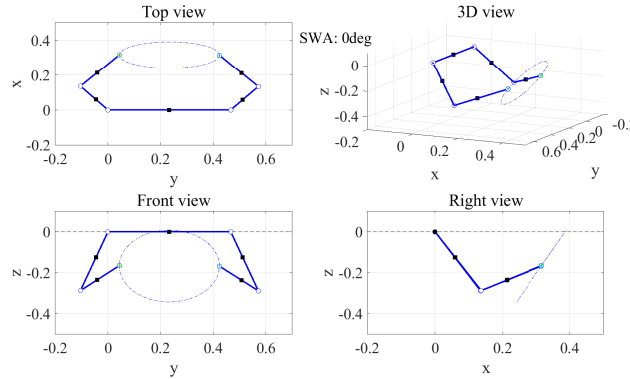

Figure 5. 3D Multibody driver model with $(\alpha_1, \alpha_4) = (-20°, 20°)$

2.8. Adding steering wheel torque on the hands

When adding a reaction torque from the steering wheel on the hands (points C and D), regular xyz coordinates x_i are used instead of generalized coordinates q. This is because the applied torque on the hands can't be expressed in generalized coordinates, as it is determined by the steering wheel torque direction. The direction of the steering wheel torque acting on the hands is independent of the joint angles of the arms as it is an input to the multibody model. Therefore the method of virtual power and Lagrange multipliers is used, describing all motions with regular coordinates.

The virtual power of a force on a system is the scalar product of the force vector F with the virtual velocity vector $\dot{x}$ of the point of application of that force.

$$\delta P = F^T \delta \dot{x} \tag{28}$$

The dynamic equilibrium yields the equations of motion. In contrast to the static equilibrium, the dynamic equilibrium includes inertial effects in the system using d'Alembert forces. Integrating over all infinitesimal mass elements dm and using a fixed coordinate system, this leads to the following virtual power expression.

$$\delta P = \left(F_i - M_{ij}\ddot{x}_j \right) \delta \dot{x}_i, \qquad i, j = 1...n \tag{29}$$

This equation sums over the number of coordinates i and j of the center of mass of the rigid bodies. When using Lagrange multipliers, the modified version of the previous equation is:

$$F_i - M_{ij}\ddot{x}_j - C_{k,i}\lambda_k = 0, \qquad i, j = 1...n, \ k = 1...m \tag{30}$$

These are the constrained equations of motion: a set of differential equations that describe the dynamic equilibrium of the system, expressed in the unknown center of mass accelerations $\ddot{x}_j$ and the unknown Lagrange multipliers λ_k. When adding constraint equations, the set of Differential Algebraic Equations (DAE's) becomes:

$$\begin{bmatrix} M & C_x^T \\ C_x & 0 \end{bmatrix} \begin{bmatrix} \ddot{x} \\ \lambda \end{bmatrix} = \begin{bmatrix} F \\ -C_{xx}\dot{x}\dot{x} \end{bmatrix} \tag{31}$$

Where M is the mass matrix, C_x is the vector containing all constraint equations and $C_{xx}\dot{x}\dot{x}$ represents the convective acceleration terms. The F-vector contains all external forces acting on the

system. These forces are gravity and the added torque on the hands, resulting in the following external force vector.

$$F_{ext} = \begin{bmatrix} F_1 & F_{\alpha 1} & F_{\beta 1} & F_2 & F_{\beta 2} & F_{\gamma 2} & F_3 & F_{\beta 3} & F_{\gamma 3} & F_4 & F_{\alpha 4} & F_{\beta 4} & F_5 \end{bmatrix}^T$$

$$F_1 = \begin{bmatrix} 0 & 0 & -m_1 g \end{bmatrix}^T$$

$$F_2 = \begin{bmatrix} 0 & 0 & -m_2 g \end{bmatrix}^T$$

$$F_3 = \begin{bmatrix} F_{rhx} & F_{rhy} & F_{rhz} - m_3 g \end{bmatrix}^T \tag{32}$$

$$F_4 = \begin{bmatrix} 0 & 0 & -m_4 g \end{bmatrix}^T$$

$$F_5 = \begin{bmatrix} F_{lhx} & F_{lhy} & F_{lhz} - m_5 g \end{bmatrix}^T$$

$$\begin{bmatrix} F_{\alpha 1} & F_{\beta 1} & F_{\beta 2} & F_{\gamma 2} & F_{\beta 3} & F_{\gamma 3} & F_{\alpha 4} & F_{\beta 4} \end{bmatrix}^T = \mathbf{0}$$

F_{rh} and F_{lh} are the forces acting on the right and left hand respectively. The forces are originated from the steering wheel torque expressed in the local $\mathcal{F}$-frame of the forearm. First, the force acting at the steering wheel in the direction of the steering column F_{sw} (acting in the direction of the steering wheel) is calculated using the applied steering torque T_{sw} and the steering wheel radius r_{sw}.

When expressing F_{sw} in the direction of the forearm, the tilt angle of the steering wheel needs to be known. This way, the angle between the applied steering wheel force and the global x-axis in the xz plane can be calculated in the global $\mathcal{N}$-frame. The force can be expressed in xyz using the angle between the steering wheel force and the global x-axis $\theta_{sw/x}$. Since the steering wheel force is acting in the xz plane, the y-component of the force vector is equal to zero.

$$^{\mathcal{N}}F_{sw} = F_{sw} \begin{bmatrix} cos(\theta_{sw/x}) \\ 0 \\ sin(\theta_{sw/x}) \end{bmatrix} \tag{33}$$

The position vector of the reaction force at the right hand coming from the steering wheel $^{\mathcal{F}}x_{C/B}$ expressed in the body fixed frame $\mathcal{F}$ is now calculated as follows.

$$\begin{aligned} ^{\mathcal{F}}x_{B/C} &= {}^{\mathcal{F}}\mathbf{R}_{\mathcal{N}} \, {}^{\mathcal{N}}x_{B/C} \\ &= \left({}^{\mathcal{N}}\mathbf{R}_{\mathcal{F}} \right)^T {}^{\mathcal{N}}x_{B/C} \\ &= \left({}^{\mathcal{N}}\mathbf{R}_{\mathcal{U}} \, {}^{\mathcal{U}}\mathbf{R}_{\mathcal{F}} \right)^T {}^{\mathcal{N}}x_{B/C} \end{aligned} \tag{34}$$

The force acting on the right and left hand expressed in the local $\mathcal{F}$-frame can be calculated as follows. The total steering wheel force is distributed over the two hands.

$$\begin{aligned} ^{\mathcal{F}}F_{lh} &= \left({}^{\mathcal{N}}\mathbf{R}_{\mathcal{U}} \, {}^{\mathcal{U}}\mathbf{R}_{\mathcal{F}} \right)^T \frac{{}^{\mathcal{N}}F_{sw}}{2} \\ &= \left(R_{\alpha 4} R_{\beta 4} R_{\gamma 3} R_{\beta 3} \right)^{-1} \frac{{}^{\mathcal{N}}F_{sw}}{2} \\ ^{\mathcal{F}}F_{rh} &= - \left({}^{\mathcal{N}}\mathbf{R}_{\mathcal{U}} \, {}^{\mathcal{U}}\mathbf{R}_{\mathcal{F}} \right)^T \frac{{}^{\mathcal{N}}F_{sw}}{2} \\ &= - \left(R_{\alpha 1} R_{\beta 1} R_{\gamma 2} R_{\beta 2} \right)^{-1} \frac{{}^{\mathcal{N}}F_{sw}}{2} \end{aligned} \tag{35}$$

The rotation matrices are not the same for the left and right arm due to different joint rotations involved.

2.9. Deriving joint angles from steering wheel envelope

The steering wheel trajectory in 3D space is created using the centerpoint c_{sw}, radius r_{sw} and normal n_{sw} which describe driving posture [22] and tilt angle of the steering wheel.

$$c_{sw} = \begin{bmatrix} 1.2l_3 \\ \frac{l_1}{2} \\ -\frac{l_2}{2} \end{bmatrix}, \quad n_{sw} = \begin{bmatrix} 3l_3 \\ 0 \\ -l_2 \end{bmatrix} \tag{36}$$

Using a nullspace, the trajectory is computed from the normal n_{sw}. The number of points ϕ_{sw} is created out of an array ranging from 0 to 2π. The final steering wheel envelope p_{sw} containing all coordinates in the global $\mathcal{N}$-frame is computed. The positions of the left and right hand for a given steering wheel angle θ_{str} are calculated using the following formula's to calculate the index of the array of p_{sw} assuming a quarter to three steering posture.

$$\theta_{lh} = \frac{\theta_{sw}}{2\pi}, \quad \theta_{rh} = \frac{\theta_{sw} + \pi}{2\pi} \tag{37}$$

Where θ_{lh} and θ_{rh} are the angles of the left and right hand relative to the starting point of the circular trajectory. The position vectors x_{SWleft} and $x_{SWright}$ are now calculated using these angles as an index for selecting the corresponding positions from the total array of points p_{sw} on the trajectory.

$$\mathcal{N}x_{SWleft} = \begin{bmatrix} p_{sw}(\theta_{lh})_x \\ p_{sw}(\theta_{lh})_y \\ p_{sw}(\theta_{lh})_z \end{bmatrix}, \quad \mathcal{N}x_{SWright} = \begin{bmatrix} p_{sw}(\theta_{rh})_x \\ p_{sw}(\theta_{rh})_y \\ p_{sw}(\theta_{rh})_z \end{bmatrix} \tag{38}$$

Because the driver's posture is varying over steering wheel angle θ_{str}, the joint angles $\phi_j = (\alpha_1, \alpha_4, \beta_1, \beta_2, \beta_3, \beta_4, \gamma_2, \gamma_3)$ are changing accordingly. The joint angles for a certain θ_{str} are calculated. This is done by stating that the position vectors of the steering wheel envelope p_{sw} for the hand positions x_{SWleft} and $x_{SWright}$ are equal to the position vectors of the hands x_D and x_C.

$$
\begin{aligned}
\mathcal{N}x_{SWleft} &= \mathcal{N}x_D \\
&= \mathcal{N}x_E + R_{\alpha_4} R_{\beta_4} R_{\gamma_3} R_{\beta_3} \begin{bmatrix} l_5 \\ 0 \\ 0 \end{bmatrix} \\
&= \begin{bmatrix} 0 \\ l_1 \\ 0 \end{bmatrix} + R_{\alpha_4} R_{\beta_4} \begin{bmatrix} 0 \\ 0 \\ -l_4 \end{bmatrix} + R_{\alpha_4} R_{\beta_4} R_{\gamma_3} R_{\beta_3} \begin{bmatrix} l_5 \\ 0 \\ 0 \end{bmatrix} \\
\mathcal{N}x_{SWright} &= \mathcal{N}x_C \\
&= \mathcal{N}x_B + R_{\alpha_1} R_{\beta_1} R_{\gamma_2} R_{\beta_2} \begin{bmatrix} l_3 \\ 0 \\ 0 \end{bmatrix} \\
&= \begin{bmatrix} 0 \\ 0 \\ 0 \end{bmatrix} + R_{\alpha_1} R_{\beta_1} \begin{bmatrix} 0 \\ 0 \\ -l_2 \end{bmatrix} + R_{\alpha_1} R_{\beta_1} R_{\gamma_2} R_{\beta_2} \begin{bmatrix} l_3 \\ 0 \\ 0 \end{bmatrix}
\end{aligned}
\tag{39}
$$

By solving the above equations for a given θ_{str}, the joint angles are calculated, refer Appendix A-5. The angles α_1 and α_4 are given an initial value of either $0°$, $10°$ or $20°$. This ensures that the number of joint DoF is equal to the number of geometrical constraint equations which results in a unique quasi-static solution.

3. Experiment and Parameter Estimation

In order to analyze the influence of changes in driving posture on the steering response, two experiments involving a steering test rig were performed. The first experiment compares driving posture for varying steering wheel angles, estimating the musculoskeletal arm admittance parameters (J_{arm}, b_{arm} & c_{arm}). The goal of the second experiment is to analyze changes in muscle activity during a low frequency sinus motion applied to the steering wheel by the driver.

3.1. Position task for varying steering wheel angles

A set of measurement data was used to analyze the effect of postural changes during driving. The experiment was conducted using the force-feedback (FFb) steering test rig. It was equipped with a direct drive of the steer to the force-feedback motor. The motor torque was requested externally using a dSPACE real-time (MicroAutoBox) machine via CAN interface at 1 ms communication time step. The muscle activation of the participant was measured using surface EMG electrodes (pairs of two, equally spaced). All EMG electrodes were placed according to SENIAM standards. The measured currents were recorded by Vitaport using eight channels. The four measured muscles are listed in Table 1 below, including their functionalities for the left arm.

Table 1. Measured muscles and their functionalities [17]

Muscle name	Location	Functionality left arm
Biceps Brachii (BB)	Upper arm	Aids in steering left
Flexor Carpi Radialis (FC)	Lower arm	Gripping the wheel
Deltoideus Anterior (DA)	Shoulder	Aids in steering right
Deltoideus Posterior (DP)	Shoulder	Aids in steering right

The first experiment was done by exciting the motor with a sinus sweep (input) signal linearly increasing from 0.1 to 20 Hz, where the driver acts as a steering wheel angle position controller with maximum possible resistance (i.e. high arm impedance) and thus minimizing the steering angle deviations.

Figure 6. Participant holding the steer in quarter-to-three hand to steering wheel position

For consistency of the experiment, the following were ensured: (a) quarter-to-three driving position (see Figure 6) of the hands at all times, (b) measurement repeatability with multiple runs considering driver arms' fatigue, (c) two motor (excitation) torque amplitudes, 1 and 2 Nm and (d) upright posture with only moving hands and arms when applying torque. The inference is as follows.

1. Test results almost independent of the torque levels.

2. A similar frequency response behavior for the same positive and negative steering angular position tests.

3.2. Sinus motion applied by driver

In the second measurement scenario, multiple low frequency sinus movements were applied to the steering wheel by the participant. There was no other disturbance applied to the steering wheel. In this case the motor torque was described by a linear spring stiffness. This implies that the steering stiffness was constant at all steering wheel angles.

The variables measured in this experiment were eight EMG signals (four for each arm, see Table 1), the steering wheel angle θ_{str}, the driver applied torque M_{str} and the motor torque M_{in}. The steering wheel diameter d_{str} was 0.315 m and the inertia J_{str} was equal to 0.03 kgm^2. The steering wheel damping b_{str} was 0.065 Nms/rad. The system was rigid and therefore the stiffness c_{str} approaches infinity as there was no compliance.

To estimate the parameters, the frequency response function (FRF) from steering torque to steering angular velocity is defined as admittance in Equation (40), containing information regarding the effective (or 1 DoF) inertia-spring-damper parameters for each test respectively. The measured FRF admittance function is given as:

$$H_{\text{adm}}(j\omega) = \frac{\omega_{\text{str}}(j\omega)}{M_{\text{str}}(j\omega)} = \frac{j\omega}{c_{\text{arm}} - J_{\text{tot}}\omega^2 + b_{\text{tot}}j\omega}. \tag{40}$$

The total inertia J_{tot} and total damping b_{tot} are determined as:

$$J_{\text{tot}} = J_{\text{arm}} + J_{\text{str}}, \quad b_{\text{tot}} = b_{\text{arm}} + b_{\text{str}} \tag{41}$$

The unknown effective driver arm parameters: inertia, damping and stiffness ($J_{\text{arm}}, b_{\text{arm}}$ and c_{arm}), were estimated by minimizing the root mean square error in gain and phase between the model ($\hat{H}_{\text{adm}}$) and the measured (H_{adm}) functions [3]. An inertia-spring-damper model is sufficient to fit the arm dynamics [7].

4. Results and discussion

The model is limited to eight rotational degrees of freedom which result in a unique solution for every θ_{str}, whereas the real-life human arm posture does not result in a unique solution as there are more rotational degrees of freedom. Therefore the results are analyzed from a qualitative perspective and all values are normalized.

The overall arm end-point admittance H_{adm} from the experimental data was estimated with high coherence and is therefore considered to be reliable for all participants. The EMG data contains very large deviations between participants due to differences in electrode placement. Due to a low-frequency drift over time caused by motor learning [23], the EMG activity in terms of magnitude cannot be compared. Cross-talk between muscles, surrounding (electro)magnetic fields and poor skin conductivity could cause noise in EMG measurement data [24]. Therefore the model is merely qualitatively comparable to the experimental data. Due to COVID-19 the experiments were performed with only two participants, who completed all scenarios. For clarity purposes, the results in muscle activity are illustrated by the results of a typical participant.

4.1. Simulation approach

Given a linear torque profile with a maximum of 3 Nm, the relation between M_{str} and θ_{str} is known. In section 3.1.8 the relation between θ_{str} and ϕ_j is calculated. Using the applied torque from section 3.1.7 and the Energy and Lagrange EoM from section 3.1.5, the relation between applied torque M_{str} and joint torque M_j is calculated. Therefore the following relations are known.

$$\frac{\partial M_{str}}{\partial \theta_{str}}, \quad \frac{\partial \theta_{str}}{\partial \phi_j} \quad \text{and} \quad \frac{\partial M_{str}}{\partial M_j} \tag{42}$$

After completing the model describing the steady-state multibody arm model in 3D (fully constrained considering 6 rotations), the resulting joint torque M_j versus joint angle ϕ_j relation was computed. The goal was to compute the joint torques over varying joint angles (due to varying steering posture). Therefore the rate of change in joint torques over joint angles (i.e. the desired output of the driver model) is mathematically related to the rate of change in steering torque input M_{str} as:

$$\frac{\partial M_{str}}{\partial \theta_{str}} = \sum_j \frac{\partial M_{str}/\partial M_j}{\partial \theta_{str}/\partial \phi_j} \frac{\partial M_j}{\partial \phi_j} \tag{43}$$

Due to the qualitative comparison between the model and experimental data, the rate of change in joint torques and joint angles is computed. The relation between joint torque and joint angle can be defined using the rotational joint stiffness K_j.

$$M_j = K_j \phi_j \tag{44}$$

The joint stiffness can be related to the rate of change in joint torques and joint angles by deriving the derivative. The partial derivative of the joint torque M_j over joint angle ϕ_j results in the following relation.

$$\frac{\partial M_j}{\partial \phi_j} = K_j + \phi_j \frac{\partial K_j}{\partial \phi_j} \tag{45}$$

This relation ensures the change in stiffness K_j of the joints can be calculated. The joint stiffness is related to the muscle contraction, and therefore provides more information about the biomechanics of the posture for various θ_{str}.

4.2. Linear relation in shoulder joint

The experimental scenario in which the participant applies low frequency sinus movements to the steering wheel is considered. In this case the shoulders are fixed to $(\alpha_1, \alpha_4) = (-20°, 20°)$ and therefore T_x is not varying over α and remains zero as can be seen from Figure 7.
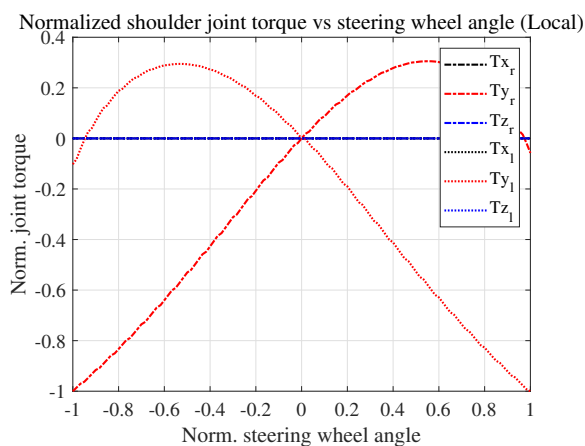
Figure 7. Shoulder joint torques over steering wheel angles
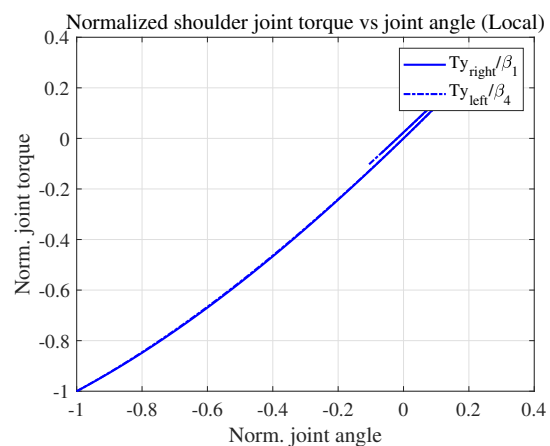
Figure 8. Shoulder joint torques over joint angles

It can be seen in Figure 8 that the stiffness in the shoulder joint is higher than the combined stiffness of the rotations in the elbow. The joint torque versus joint angle relation is almost linear in the

shoulder. The rotation stiffness is 0.0529 Nm/deg and the slope in the joint torque vs joint angle plot is constant.

The EMG activity of the DA muscle during the low frequency sinus measurement is shown in Figure 9. As the quantitative EMG data is containing bias and random errors due to muscle memory and measurement noise, only trends in these values are analyzed.
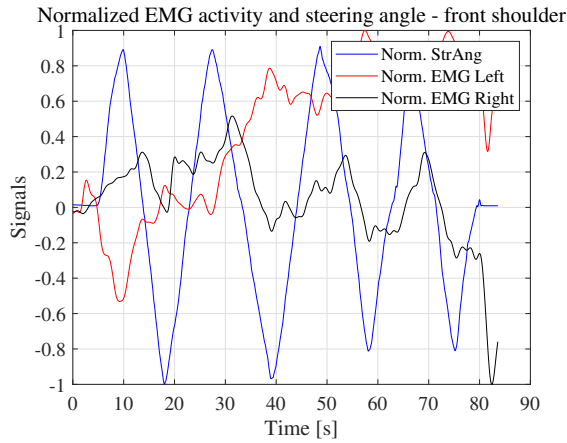
Figure 9. EMG activity DA (i.e. front shoulder) muscle over time
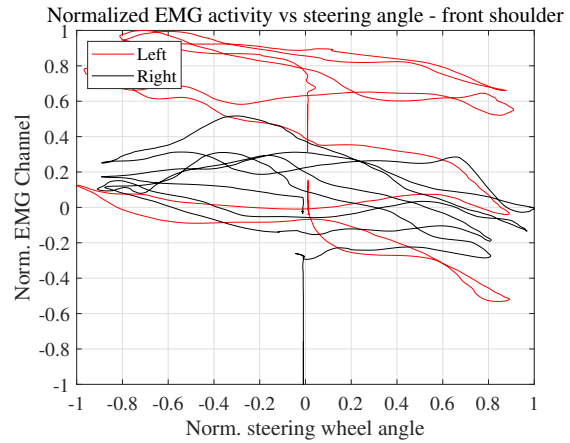
Figure 10. Muscle activity over steering wheel angle

The muscle activity of the front shoulder muscle (Figure 10) resembles the shoulder joint torque. The change in EMG activity over varying steering wheel angle is approximately linear. This is notable, since the change in torque over steering wheel angle from the driver model simulation was for the largest contribution linear as well (Figure 7). In terms of magnitude, the data shows relatively high values in shoulder joint torque compared to the elbow data.

4.3. Non-linear relation in elbow joint

The stiffness in the elbow joint is varying over θ_{str} (i.e. varying joint angles). The initial position at $\theta_{str} = 0°$ is quarter to three. The driver model simulation results are shown in Figure 11 and 12. The values in joint torque versus steering wheel angle graphs are normalized for qualitative analysis.
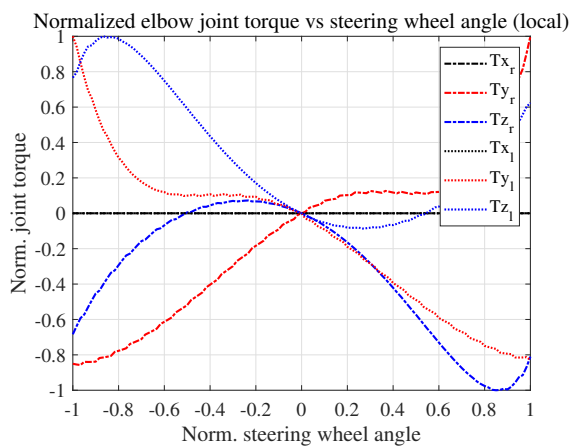
Figure 11. Normalized elbow joint torques over steering wheel angles
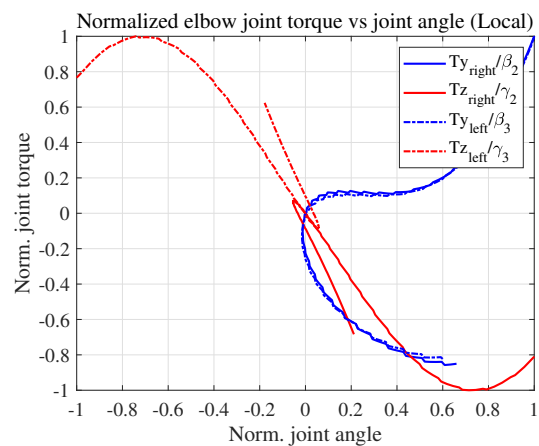
Figure 12. Normalized elbow joint torques over joint angles

The rotational degrees of freedom in the driver model are limited to y- and z-axis rotation. Therefore the rotational joint torque in x-direction T_x remains zero for all steering wheel angles (Figure 11). The rotational torques in y- and z-direction in the elbow joint show a non-linear symmetric behaviour over varying steering wheel angle.

In Figure 12 the joint torque over joint angle graph shows a non-linear relation as well. For the postures where the hand is moving from side to top of the steering wheel, the torque over angle relation is close to linear for both β_2 and γ_2 rotations (see Figures 11 and 12). In the postures where the hand is moving from side to bottom of the steering wheel, the torque over angle relation is non-linear for β_2 and γ_2. The same holds for the left arm and the joint rotations β_3 and γ_3.
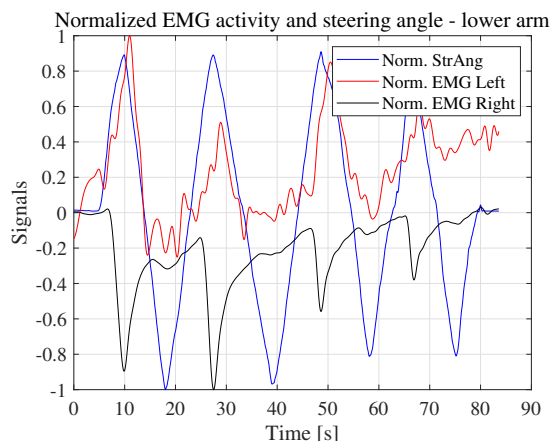
Figure 13. EMG activity FC (i.e. lower arm) over time
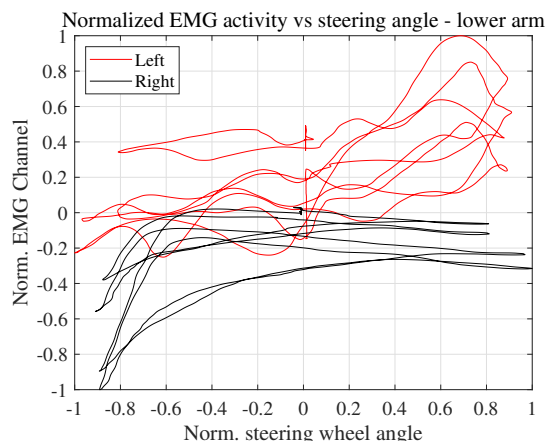
Figure 14. Muscle activity over steering wheel angle

The EMG activity of the FC muscle during the sine sweep maneuver is shown in Figure 13 for the lower arm muscle, which generates a force acting on the elbow. Therefore this muscle's data is compared to the elbow joint torque from the driver model simulation results.

In Figure 14, the muscle activity of the lower arm muscle is shown over steering wheel angle. The change in EMG activity over varying steering wheel angle demonstrates non-linear trends for off-centre steering wheel angles. Similar behaviour was seen in the joint torque versus steering wheel angle results from the driver model (Figure 11). In terms of magnitude, the data shows relatively small values in shoulder joint torque compared to the shoulder data.

4.4. Frequency Response Function results

The frequency response plot corresponding to Equation (40), is given in Figure 15.
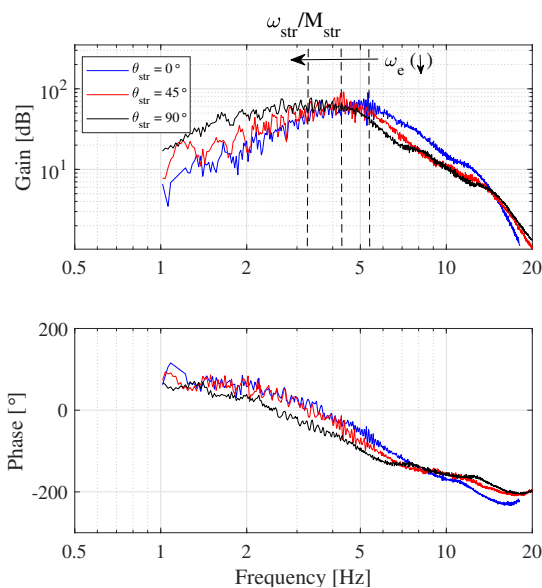
Figure 15. Measured FRF for three steering angular positions ($0°, 45°$ and $90°$) from steering angular speed to steering torque.

The FRF gain, phase and coherence are plotted over 1 to 20 Hz frequency range. It includes the data from three different steering angular positions (i.e. $0°, 45°$ and $90°$) with an excitation torque level of 1 Nm.

The main observation from this result is the drop in first FRF eigenfrequency with increasing steering angular position, particularly from $45°$ to $90°$. The cause is either decreasing c_{arm} or increasing J_{arm} or both simultaneously. The inertia J_{arm} remains the same for a physical driver arm (considering the same participant) because of conservation of mass. Therefore the drop in eigenfrequency ω_e is primarily caused by the drop in effective arm stiffness c_{arm} with an increasing steering angle. This can be observed in the steady state gain response of θ_{str}/M_{str} FRF plot.

5. Conclusions

The experimental results show that the maximum effective estimated driver arm stiffness reduces with an increasing steering angular position. This impacts the entire frequency response (especially the steady state gain of the steering admittance function). Hence it is concluded that this is caused by the driving arm posture, which was investigated by the 3-dimensional driver model. It further implies that the decreasing muscular arm stiffness with an increasing steering wheel angle, requires an increasing assistance from the servo motor (in conventional systems) for a desired and a consistent steering feel. The rate of steering torque drop over steering wheel angle is intentional (within linear vehicle and tire operating range), as the changes in driving arm posture cause a reduction in the arms' stiffness.

The 3-dimensional driver model data shows similar qualitative trends as in the experimental results. The following conclusions can be drawn from the simulation and experimental results:

- The torque distribution over the joints is matching the expectation that a large number of muscles or a relatively large physiological cross-sectional area (PCSA) generates a high muscle torque.
- The change in joint torque over steering wheel angle is found to be approximately linear in the shoulder joint in both simulation and experimental results.
- Non-linearity in joint torque over steering wheel angle are present in the elbow joint. This result was noticeable in simulation as well as experimental data.
- Decreased arm stiffness required the driver to be aided more at higher steering wheel angles. This can be explained by the joint torques which is dependent on driving posture.
- A change in haptic interface results in a different steering response due to changed posture. The steering feedback should therefore be re-designed for new methods of haptic steering interfaces.

Abbreviations

The following abbreviations are used in this manuscript:

SWA	Steering Wheel Angle
NMS	Neuromusculoskeletal
EMG	Electromyography
DoF	Degree of Freedom
CoM	Center of Mass
DAE	Differential Algebraic Equation
FFb	Force-Feedback
SENIAM	Surface Electromyography for the Non-Invasive Assessment of Muscles
BB	Biceps Brachii
FC	Flexor Carpi Radialis
DA	Deltoideus Anterior
CP	Deltoideus Posterior
FRF	Frequency Response Function
PCSA	Physiological Cross-Sectional Area

References

1. Chugh, T. *Haptic Feedback Control Methods for Steering Systems*; Chalmers University of Technology, 2019.
2. Chugh, T.; Bruzelius, F.; Klomp, M.; Shyrokau, B. Design of haptic feedback control for steer-by-wire. 2018 21st International Conference on Intelligent Transportation Systems (ITSC). IEEE, 2018, pp. 1737–1744.
3. Chugh, T.; Bruzelius, F.; Klomp, M.; Shyrokau, B. An approach to develop haptic feedback control reference for steering systems using open-loop driving manoeuvres. *Vehicle System Dynamics* **2019**, pp. 1–24.
4. Damian, M.; Shyrokau, B.; Ocariz, A.; Akutain, X.C. Torque control for more realistic hand-wheel haptics in a driving simulator. *Driving Simulation Conference Europe* **2019**.
5. McRuer, D.T.; Jex, H.R. A review of quasi-linear pilot models. *IEEE transactions on human factors in electronics* **1967**, pp. 231–249.
6. Kondo, M.; Ajimine, A. Driver's sight point and dynamics of the driver-vehicle-system related to it. Technical report, SAE Technical Paper, 1968.
7. Pick, A.; Cole, D.J. Dynamic properties of a driver's arms holding a steering wheel. *Proceedings of the Institution of Mechanical Engineers, Part D: Journal of Automobile Engineering* **2007**, *221*, 1475–1486.
8. Pick, A.J.; Cole, D.J. A mathematical model of driver steering control including neuromuscular dynamics. *Journal of Dynamic Systems, Measurement, and Control* **2008**, *130*, 031004.
9. Cole, D.J. A path-following driver–vehicle model with neuromuscular dynamics, including measured and simulated responses to a step in steering angle overlay. *Vehicle system dynamics* **2012**, *50*, 573–596.
10. Hoult, W.; Cole, D.J. A neuromuscular model featuring co-activation for use in driver simulation. *Vehicle System Dynamics* **2008**, *46*, 175–189.
11. Sentouh, C.; Chevrel, P.; Mars, F.; Claveau, F. A Human-Centered Approach of Steering Control Modeling. Proceedings of the 21st IAVSD Symposium on Dynamics of Vehicles on Roads and Tracks, Stockholm, Sweden. Citeseer, 2009, pp. 1–12.
12. Donges, E. A two-level model of driver steering behavior. *Human factors* **1978**, *20*, 691–707.
13. de Vlugt, E.; Schouten, A.C.; van der Helm, F.C. Closed-loop multivariable system identification for the characterization of the dynamic arm compliance using continuous force disturbances: a model study. *Journal of neuroscience methods* **2003**, *122*, 123–140.
14. Van der Helm, F.C.; Schouten, A.C.; de Vlugt, E.; Brouwn, G.G. Identification of intrinsic and reflexive components of human arm dynamics during postural control. *Journal of neuroscience methods* **2002**, *119*, 1–14.
15. Katzourakis, D.I.; Abbink, D.A.; Velenis, E.; Holweg, E.; Happee, R. Driver's arms' time-variant neuromuscular admittance during real car test-track driving. *IEEE Transactions on Instrumentation and Measurement* **2013**, *63*, 221–230.
16. De Vlugt, E.; Schouten, A.C.; Van Der Helm, F.C. Quantification of intrinsic and reflexive properties during multijoint arm posture. *Journal of neuroscience methods* **2006**, *155*, 328–349.
17. Abbink, D.A.; Mulder, M.; Van Paassen, M.M. Measurements of muscle use during steering wheel manipulation. 2011 IEEE International Conference on Systems, Man, and Cybernetics. IEEE, 2011, pp. 1652–1657.
18. Abbink, D.A. Neuromuscular analysis of haptic gas pedal feedback during car following **2006**.

19. Mulder, M.; Pool, D.M.; Abbink, D.A.; Boer, E.R.; Zaal, P.M.; Drop, F.M.; van der El, K.; van Paassen, M.M. Manual control cybernetics: State-of-the-art and current trends. *IEEE Transactions on Human-Machine Systems* **2017**, *48*, 468–485.

20. Winter, D. Anthropometry. *Biomechanics and motor control of human movement* **1990**.

21. Vallery, H.; Schwab, A.L. *Advanced Dynamics*; Delft University of Technology, 2018.

22. Andreoni, G.; Santambrogio, G.C.; Rabuffetti, M.; Pedotti, A. Method for the analysis of posture and interface pressure of car drivers. *Applied ergonomics* **2002**, *33*, 511–522.

23. Schmidt, R.A.; Wrisberg, C.A. *Motor learning and performance: A situation-based learning approach*; Human kinetics, 2008.

24. De Luca, C.J. The use of surface electromyography in biomechanics. *Journal of applied biomechanics* **1997**, *13*, 135–163.

3-Dimensional Driver model

This chapter contains more detailed information about the driver model and the simulation results. The rotation matrices, CoM coordinates, constraint vector, the linear torque profile and the simulation results are shown.

A-1 Rotation matrices

For the right arm (bodies 2 and 3) the rotation matrices are the following for the individual frame mappings.

$$
\begin{aligned}
{}^{\mathcal{N}}\mathbf{R}_{\mathcal{U}} &= R_{\alpha_1}R_{\beta_1} \\
&= \begin{bmatrix} 1 & 0 & 0 \\ 0 & cos\alpha_1 & -sin\alpha_1 \\ 0 & sin\alpha_1 & cos\alpha_1 \end{bmatrix} \begin{bmatrix} cos\beta_1 & 0 & sin\beta_1 \\ 0 & 1 & 0 \\ -sin\beta_1 & 0 & cos\beta_1 \end{bmatrix} \\
&= \begin{bmatrix} \cos\beta_1 & 0 & \sin\beta_1 \\ \sin\alpha_1\sin\beta_1 & \cos\alpha_1 & -\cos\beta_1\sin\alpha_1 \\ -\cos\alpha_1\sin\beta_1 & \sin\alpha_1 & \cos\alpha_1\cos\beta_1 \end{bmatrix} \\
{}^{\mathcal{U}}\mathbf{R}_{\mathcal{F}} &= R_{\gamma_2}R_{\beta_2} \\
&= \begin{bmatrix} cos\gamma_2 & -sin\gamma_2 & 0 \\ sin\gamma_2 & cos\gamma_2 & 0 \\ 0 & 0 & 1 \end{bmatrix} \begin{bmatrix} cos\beta_2 & 0 & sin\beta_2 \\ 0 & 1 & 0 \\ -sin\beta_2 & 0 & cos\beta_2 \end{bmatrix} \\
&= \begin{bmatrix} \cos\beta_2\cos\gamma_2 & -\sin\gamma_2 & \cos\gamma_2\sin\beta_2 \\ \cos\beta_2\sin\gamma_2 & \cos\gamma_2 & \sin\beta_2\sin\gamma_2 \\ -\sin\beta_2 & 0 & \cos\beta_2 \end{bmatrix}
\end{aligned}
\tag{A-1}
$$

For consistency, all motions are expressed in the global $\mathcal{N}$-frame. The position of the forearm is described using ${}^{\mathcal{N}}\mathbf{R}_{\mathcal{F}}$ being the rotation matrix mapping the position from body-fixed $\mathcal{F}$-frame of the forearm to the inertial frame.

$$
\begin{aligned}
{}^{\mathcal{N}}\mathbf{R}_{\mathcal{F}} &= {}^{\mathcal{N}}\mathbf{R}_{\mathcal{U}} \, {}^{\mathcal{U}}\mathbf{R}_{\mathcal{F}} \\
&= R_{\alpha_1} R_{\beta_1} R_{\gamma_2} R_{\beta_2}
\end{aligned}
$$

$$
= \left[\begin{array}{l}
\cos\beta_1 \, \cos\beta_2 \, \cos\gamma_2 - \sin\beta_1 \, \sin\beta_2 \\
\cos\alpha_1 \, \cos\beta_2 \, \sin\gamma_2 + \cos\beta_1 \, \sin\alpha_1 \, \sin\beta_2 + \cos\beta_2 \, \cos\gamma_2 \, \sin\alpha_1 \, \sin\beta_1 \quad \dots \\
\cos\beta_2 \, \sin\alpha_1 \, \sin\gamma_2 - \cos\alpha_1 \, \cos\beta_1 \, \sin\beta_2 - \cos\alpha_1 \, \cos\beta_2 \, \cos\gamma_2 \, \sin\beta_1 \\[4pt]
\qquad - \cos\beta_1 \, \sin\gamma_2 \\
\cos\alpha_1 \, \cos\gamma_2 - \sin\alpha_1 \, \sin\beta_1 \, \sin\gamma_2 \quad \dots \\
\cos\gamma_2 \, \sin\alpha_1 + \cos\alpha_1 \, \sin\beta_1 \, \sin\gamma_2 \\[4pt]
\qquad \cos\beta_2 \, \sin\beta_1 + \cos\beta_1 \, \cos\gamma_2 \, \sin\beta_2 \\
\cos\alpha_1 \, \sin\beta_2 \, \sin\gamma_2 - \cos\beta_1 \, \cos\beta_2 \, \sin\alpha_1 + \cos\gamma_2 \, \sin\alpha_1 \, \sin\beta_1 \, \sin\beta_2 \\
\cos\alpha_1 \, \cos\beta_1 \, \cos\beta_2 + \sin\alpha_1 \, \sin\beta_2 \, \sin\gamma_2 - \cos\alpha_1 \, \cos\gamma_2 \, \sin\beta_1 \, \sin\beta_2
\end{array} \right]
\tag{A-2}
$$

A-2 CoM coordinates

Using the set of joint and CoM position vectors, the CoM coordinates of the five bodies, $x_i = (x_1, y_1, z_1 \dots x_5, y_5, z_5)$, expressed in terms of the system parameters and angles of rotation can be constructed as follows.

$$
x_i =
\begin{bmatrix}
x_1 \\ y_1 \\ z_1 \\
x_2 \\ y_2 \\ z_2 \\
x_3 \\ y_3 \\ z_3 \\
x_4 \\ y_4 \\ z_4 \\
x_5 \\ y_5 \\ z_5
\end{bmatrix}
=
\begin{bmatrix}
0 \\[4pt]
\tfrac{l_1}{2} \\[4pt]
0 \\[4pt]
-cg_2 \sin(\beta_1) \\[4pt]
cg_2 \cos(\beta_1) \sin(\alpha_1) \\[4pt]
-cg_2 \cos(\alpha_1) \cos(\beta_1) \\[4pt]
-l_2 \sin(\beta_1) - cg_3 \left(\sin(\beta_2)\left(\cos(\alpha_1)\sin(\gamma_2) + \cos(\gamma_2)\sin(\alpha_1)\sin(\beta_2)\right) - \cos(\beta_1)\cos(\beta_2)\cos(\gamma_2)\right) \\[4pt]
cg_3 \left(\cos(\beta_2)\left(\cos(\alpha_1)\sin(\gamma_2) + \cos(\gamma_2)\sin(\alpha_1)\sin(\beta_2)\right) - \cos(\beta_1)\cos(\beta_2)\cos(\gamma_2)\right) + l_2 \cos(\beta_1)\sin(\alpha_1) \\[4pt]
cg_3 \left(\cos(\beta_2)\left(\sin(\alpha_1)\sin(\gamma_2) - \cos(\alpha_1)\cos(\gamma_2)\sin(\beta_2)\right) - \cos(\alpha_1)\cos(\beta_1)\cos(\beta_2)\right) - l_2 \cos(\alpha_1)\cos(\beta_1) \\[4pt]
-cg_4 \sin(\beta_4) \\[4pt]
l_1 + cg_4 \cos(\beta_4) \sin(\alpha_4) \\[4pt]
-cg_4 \cos(\alpha_4) \cos(\beta_4) \\[4pt]
-l_4 \sin(\beta_4) - cg_5 \left(\sin(\beta_3)\left(\cos(\alpha_4)\sin(\gamma_3) + \cos(\gamma_3)\sin(\alpha_4)\sin(\beta_3)\right) - \cos(\beta_4)\cos(\beta_3)\cos(\gamma_3)\right) \\[4pt]
l_1 + cg_5 \left(\cos(\beta_3)\left(\cos(\alpha_4)\sin(\gamma_3) + \cos(\gamma_3)\sin(\alpha_4)\sin(\beta_3)\right) + \cos(\beta_4)\sin(\alpha_4)\sin(\beta_3)\right) + l_4 \cos(\beta_4)\sin(\alpha_4) \\[4pt]
cg_5 \left(\cos(\beta_3)\left(\sin(\alpha_4)\sin(\gamma_3) - \cos(\alpha_4)\cos(\gamma_3)\sin(\beta_3)\right) - \cos(\alpha_4)\cos(\beta_4)\cos(\beta_3)\right) - l_4 \cos(\alpha_4)\cos(\beta_4)
\end{bmatrix}
\tag{A-3}
$$

A-3 Constraint vector

The joint constraints combined in one vector $\boldsymbol{C}_x$ are

$$
\boldsymbol{C}_x = \begin{bmatrix}
x_2 - \mathrm{r}_{\mathrm{CoM2}}(x) \\
y_2 - \mathrm{r}_{\mathrm{CoM2}}(y) \\
z_2 - \mathrm{r}_{\mathrm{CoM2}}(z) \\
x_3 - \mathrm{r}_{\mathrm{CoM3}}(x) \\
y_3 - \mathrm{r}_{\mathrm{CoM3}}(y) \\
z_3 - \mathrm{r}_{\mathrm{CoM3}}(z) \\
x_3 + \mathrm{r}_{\mathrm{CoM3}}(x) - x_{\mathrm{B}} - \mathrm{r}_{\mathrm{SWright}}(x) \\
y_3 + \mathrm{r}_{\mathrm{CoM3}}(y) - y_{\mathrm{B}} - \mathrm{r}_{\mathrm{SWright}}(y) \\
z_3 + \mathrm{r}_{\mathrm{CoM3}}(x) - z_{\mathrm{B}} - \mathrm{r}_{\mathrm{SWright}}(z) \\
x_4 - \mathrm{r}_{\mathrm{CoM4}}(x) \\
y_4 - \mathrm{r}_{\mathrm{CoM4}}(y) \\
z_4 - \mathrm{r}_{\mathrm{CoM4}}(z) \\
x_5 - \mathrm{r}_{\mathrm{CoM5}}(x) \\
y_5 - \mathrm{r}_{\mathrm{CoM5}}(y) \\
z_5 - \mathrm{r}_{\mathrm{CoM5}}(z) \\
x_5 + \mathrm{r}_{\mathrm{CoM5}}(x) - x_{\mathrm{E}} - \mathrm{r}_{\mathrm{SWleft}}(x) \\
y_5 + \mathrm{r}_{\mathrm{CoM5}}(y) - y_{\mathrm{E}} - \mathrm{r}_{\mathrm{SWleft}}(y) \\
z_5 + \mathrm{r}_{\mathrm{CoM5}}(x) - z_{\mathrm{E}} - \mathrm{r}_{\mathrm{SWleft}}(z)
\end{bmatrix} = \boldsymbol{0} \tag{A-4}
$$

Substituting the joint and CoM position vectors using the Symbolic Math Toolbox, this results in the following constraint vector.

$$
C_x =
\begin{bmatrix}
x_2 + \mathrm{cg}_2 \sin(\beta_1) \\
y_2 - \mathrm{cg}_2 \cos(\beta_1) \sin(\alpha_1) \\
z_2 + \mathrm{cg}_2 \cos(\alpha_1) \cos(\beta_1) \\
x_3 + l_2 \sin(\beta_1) + \mathrm{cg}_3 \left(\sin(\beta_1)\sin(\beta_2) - \cos(\beta_1)\cos(\beta_2)\cos(\gamma_2)\right) \\
y_3 - \mathrm{cg}_3 \left(\cos(\beta_2)\left(\cos(\alpha_1)\sin(\gamma_2) + \cos(\gamma_2)\sin(\alpha_1)\sin(\beta_1)\right) + \cos(\beta_1)\sin(\alpha_1)\sin(\beta_2)\right) - \cos(\alpha_1)\cos(\beta_1)\sin(\beta_2)) - l_2 \cos(\beta_1)\sin(\alpha_1) \\
z_3 - \mathrm{cg}_3 \left(\cos(\beta_2)\left(\sin(\alpha_1)\sin(\gamma_2) - \cos(\alpha_1)\cos(\gamma_2)\sin(\beta_1)\right) - \cos(\alpha_1)\cos(\beta_1)\sin(\beta_2)\right) + l_2 \cos(\alpha_1)\cos(\beta_1) \\
x_3 - \mathrm{cg}_3 \left(\sin(\beta_1)\sin(\beta_2) - \cos(\beta_1)\cos(\beta_2)\cos(\gamma_2)\right) - \mathrm{rSWright}(x) \\
y_3 + \mathrm{cg}_3 \left(\cos(\beta_2)\left(\cos(\alpha_1)\sin(\gamma_2) + \cos(\gamma_2)\sin(\alpha_1)\sin(\beta_1)\right) + \cos(\beta_1)\sin(\alpha_1)\sin(\beta_2)\right) - \mathrm{rSWright}(y) \\
z_3 + \mathrm{cg}_3 \left(\sin(\alpha_1)\sin(\gamma_2) - \cos(\alpha_1)\cos(\gamma_2)\sin(\beta_1)\right) - \cos(\alpha_1)\cos(\beta_1)\sin(\beta_2)) - \mathrm{rSWright}(z) \\
x_4 + \mathrm{cg}_4 \sin(\beta_4) \\
y_4 - l_1 - \mathrm{cg}_4 \cos(\beta_4)\sin(\alpha_4) \\
z_4 + \mathrm{cg}_4 \cos(\alpha_4)\cos(\beta_4) \\
x_5 + l_4 \sin(\beta_4) + \mathrm{cg}_5 \left(\sin(\beta_3)\sin(\beta_4) - \cos(\beta_3)\cos(\beta_4)\cos(\gamma_3)\right) \\
y_5 - l_1 - \mathrm{cg}_5 \left(\cos(\beta_3)\left(\cos(\alpha_4)\sin(\gamma_3) + \cos(\gamma_3)\sin(\alpha_4)\sin(\beta_4)\right) + \cos(\alpha_4)\sin(\beta_4)\sin(\beta_3)\right) - l_4 \cos(\beta_4)\sin(\alpha_4) \\
z_5 - \mathrm{cg}_5 \left(\cos(\beta_3)\left(\sin(\alpha_4)\sin(\gamma_3) - \cos(\alpha_4)\cos(\gamma_3)\sin(\beta_4)\right) - \cos(\alpha_4)\cos(\beta_4)\sin(\beta_3)\right) + l_4 \cos(\alpha_4)\cos(\beta_4) \\
x_5 - \mathrm{cg}_5 \left(\sin(\beta_3)\sin(\beta_4) - \cos(\beta_3)\cos(\beta_4)\cos(\gamma_3)\right) - \mathrm{rSWleft}(x) \\
y_5 + \mathrm{cg}_5 \left(\cos(\beta_3)\left(\cos(\alpha_4)\sin(\gamma_3) + \cos(\gamma_3)\sin(\alpha_4)\sin(\beta_4)\right) + \cos(\alpha_4)\sin(\beta_4)\sin(\beta_3)\right) - \mathrm{rSWleft}(y) \\
z_5 + \mathrm{cg}_5 \left(\cos(\beta_3)\left(\sin(\alpha_4)\sin(\gamma_3) - \cos(\alpha_4)\cos(\gamma_3)\sin(\beta_4)\right) - \cos(\alpha_4)\cos(\beta_4)\sin(\beta_3)\right) - \mathrm{rSWleft}(z)
\end{bmatrix}
= \mathbf{0}
\tag{A-5}
$$

A-4   Linear torque profile

The method of virtual power and Lagrange multipliers is used for adding the linear torque profile on the hands. The maximum torque level applied is 3 Nm, varying linearly over steering wheel angle (see Figure A-1). The steering wheel diameter is 0.38 m. Therefore the steering wheel force is shown in Figure A-2.
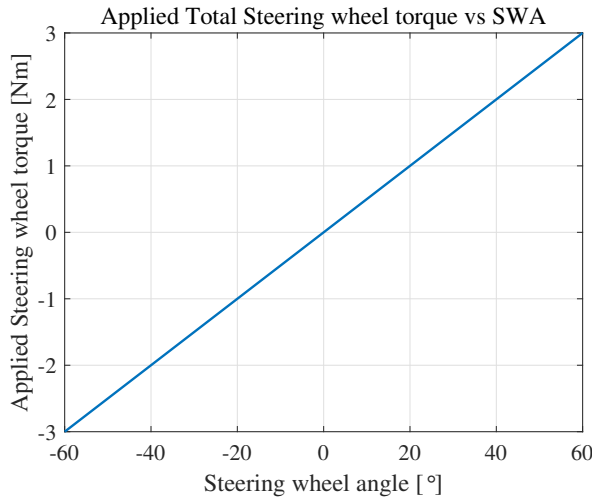
Figure A-1: Applied total steering wheel torque over steering wheel angle
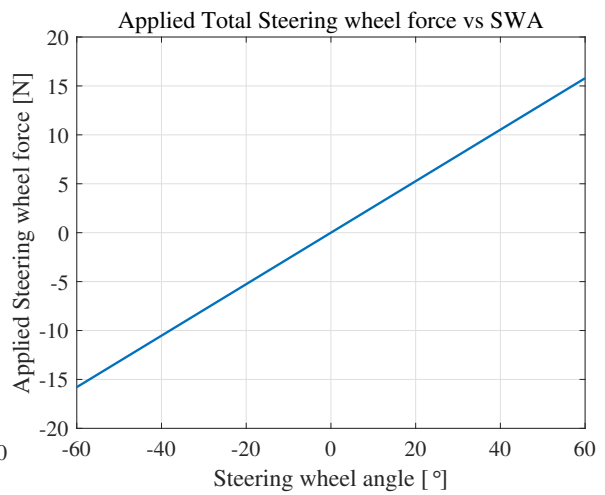
Figure A-2: Applied total steering wheel force over steering wheel angle

The force components expressed in global x, y and z coordinates are as follows for both left and right arm, refer Figures A-3 and A-4.

Figure A-3: Reaction force at the left hand over varying steering wheel angle

Figure A-4: Reaction force at the right hand over varying steering wheel angle

Next, the global reaction forces are expressed in the local forearm frame of each arm. The total applied steering wheel force is distributed evenly over both hands. As can be seen from the above figures, the components of the total force vector are mirrored for each hand accordingly. The y-component is mirrored in both x- and y-axis whereas the x- and z-components are mirrored in the y-axis only.

Figure A-5: Reaction force at the left hand expressed in local forearm frame
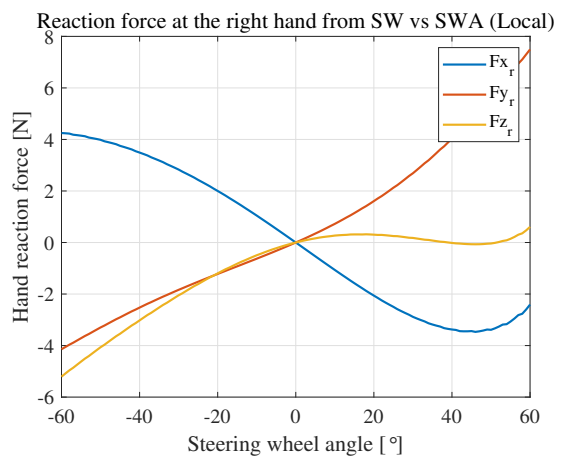
Figure A-6: Reaction force at the right hand expressed in local forearm frame

In Figure A-7, the reaction forces on both hands are visualized in the same graph.
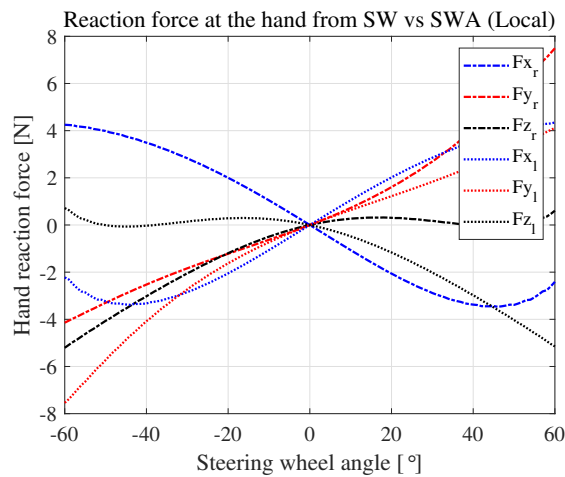
Figure A-7: Reaction force at the hands expressed in local forearm frame

A-5 Joint angles derived from steering wheel envelope

As a reference for the results in this chapter, the free body diagram can be seen in Figure A-8.
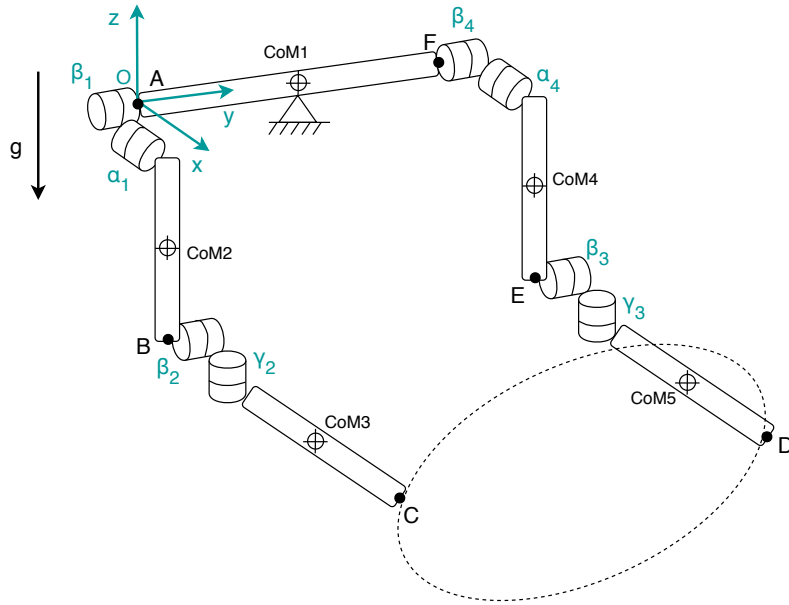
Figure A-8: Free body diagram of the human arms

The joint angles are calculated for the steering wheel angles up to 60°, refer Figure A-10. In this case the shoulders are fixed to $(\alpha_1, \alpha_4) = (-0°, 0°)$.
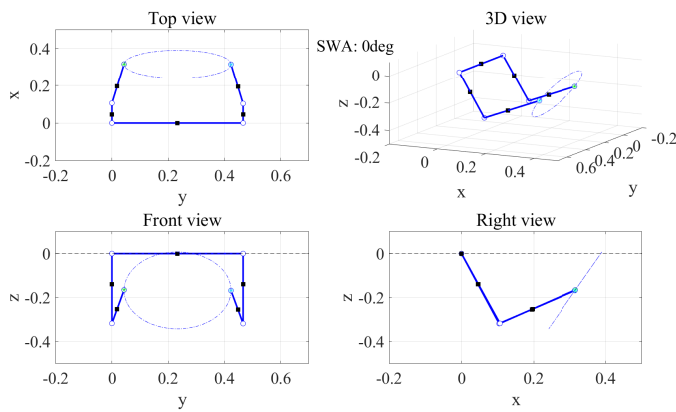
Figure A-9: 3D Multibody driver model with $(\alpha_1, \alpha_4) = (-0°, 0°)$
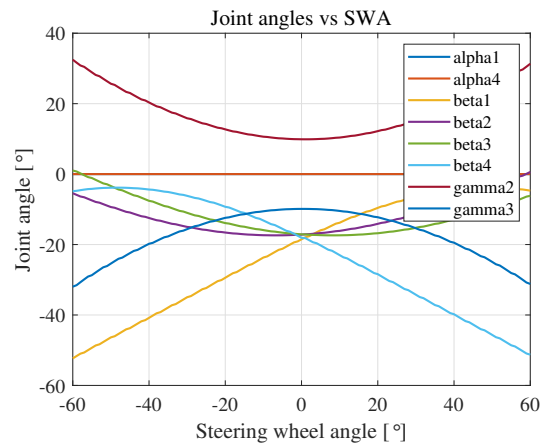
Figure A-10: Joint angles for various steering wheel angle positions for $(\alpha_1, \alpha_4) = \pm\ 0°$

Figure A-12 shows the joint angles for shoulders fixed to $(\alpha_1, \alpha_4) = (-10°, 10°)$.
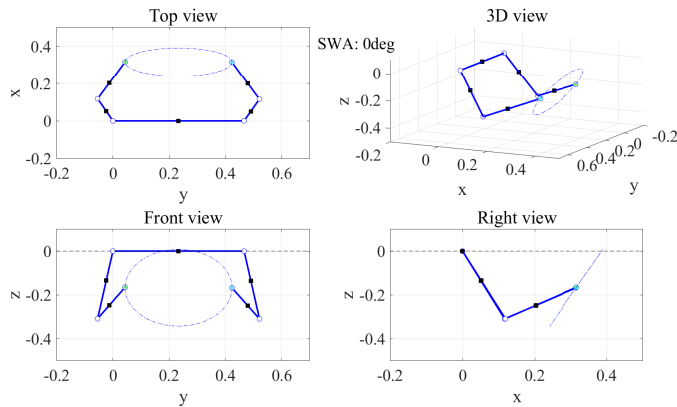
Figure A-11: 3D Multibody driver model with (α_1, α_4) = (-10°, 10°)
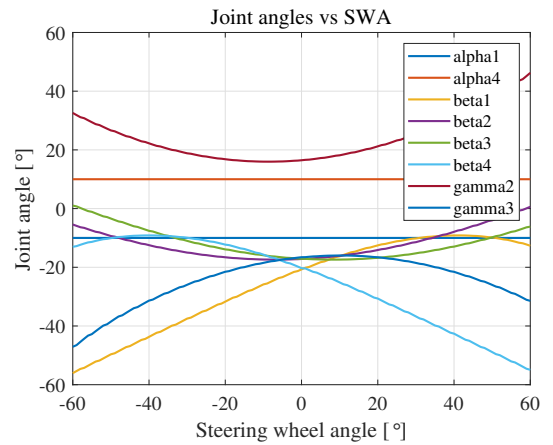
Figure A-12: Joint angles for various steering wheel angle positions for $(\alpha_1, \alpha_4) = \pm 10°$

Figure A-14 shows the joint angles for shoulders fixed to (α_1, α_4) = (-20°, 20°).
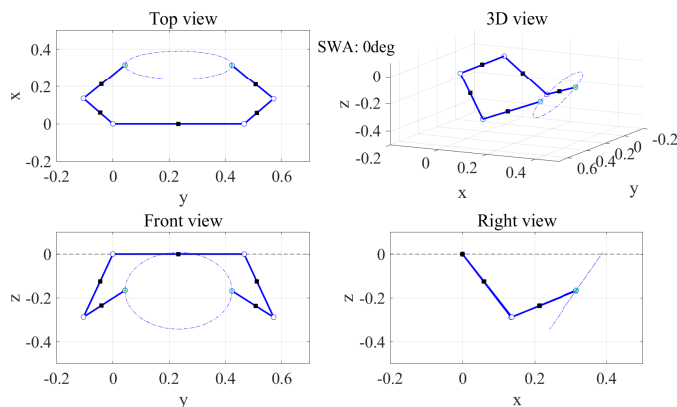
Figure A-13: 3D Multibody driver model with (α_1, α_4) = (-20°, 20°)
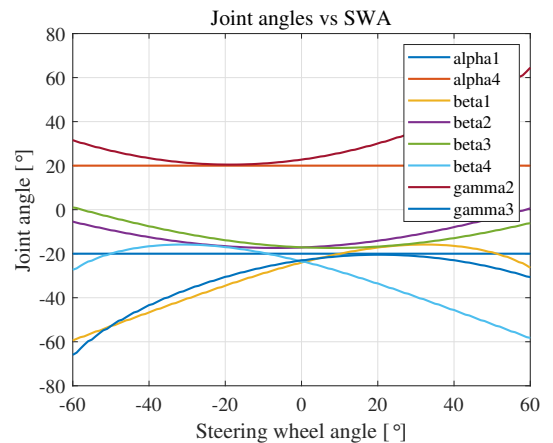
Figure A-14: Joint angles for various steering wheel angle positions for $(\alpha_1, \alpha_4) = \pm 20°$

A-6 Joint reaction forces and torques

The experimental scenario in which the participant applies low frequency sinus movements to the steering wheel is considered. The resulting joint reaction forces are shown below for different values of α_1 and α_4. In this case the shoulders are fixed to (α_1, α_4) = (-0°, 0°) and the results can be seen in Figures A-15 and A-16.
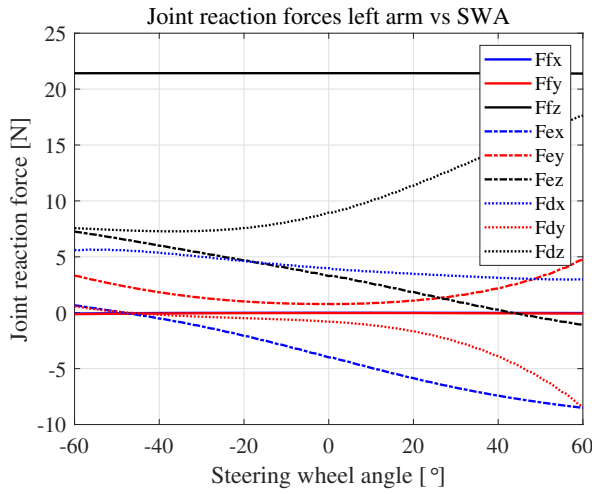
Figure A-15: Reaction forces at the left arm expressed in the global frame for $(\alpha_1, \alpha_4) = \pm\ 0°$
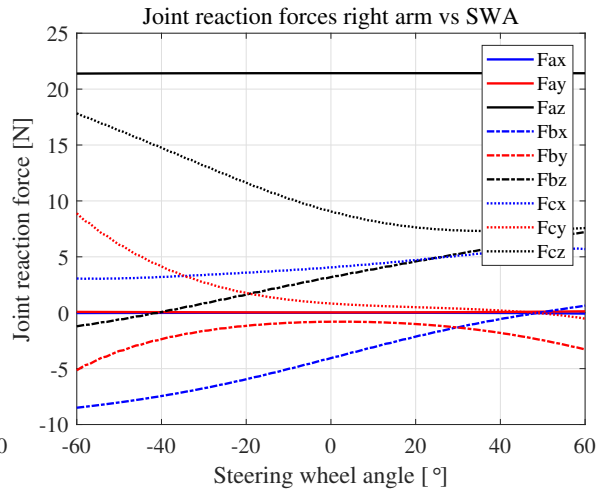
Figure A-16: Reaction force at the right arm expressed in the global frame for $(\alpha_1, \alpha_4) = \pm\ 0°$

Figures A-17 and A-18 show the joint reaction forces for shoulders fixed to $(\alpha_1, \alpha_4) = $ (-10°, 10°).
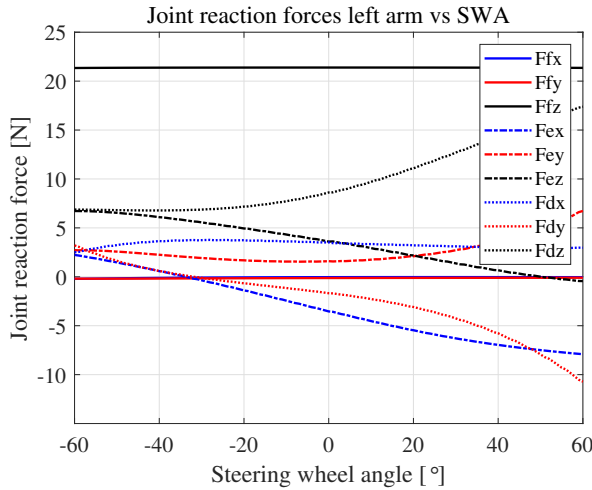
Figure A-17: Reaction forces at the left arm expressed in the global frame for $(\alpha_1, \alpha_4) = \pm\ 10°$
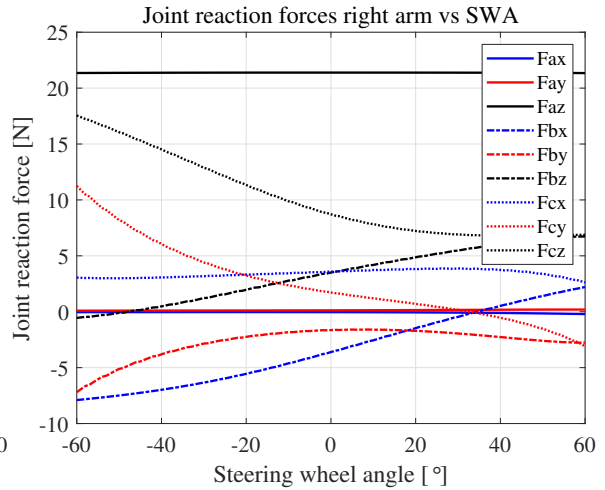
Figure A-18: Reaction force at the right arm expressed in the global frame for $(\alpha_1, \alpha_4) = \pm\ 10°$

Figures A-19 and A-20 show the joint reaction forces for shoulders fixed to $(\alpha_1, \alpha_4) = $ (-20°, 20°).
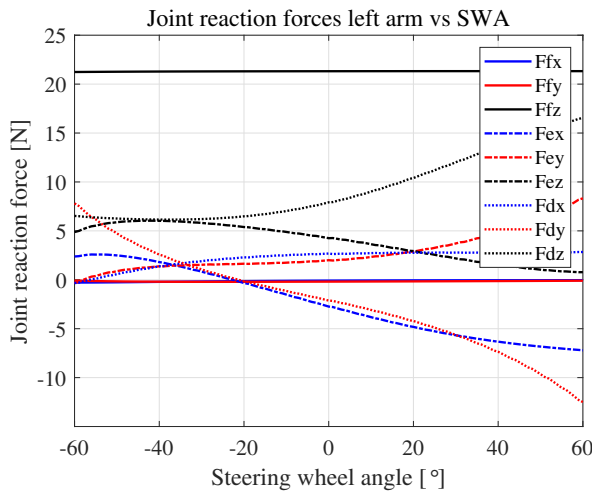
Figure A-19: Reaction forces at the left arm expressed in the global frame for $(\alpha_1, \alpha_4) = \pm\, 20°$
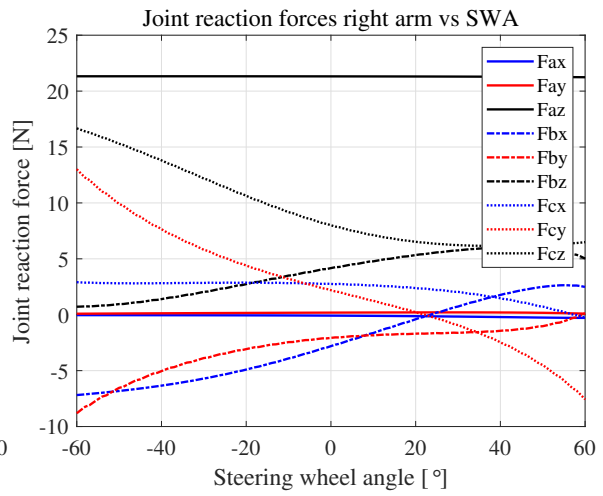
Figure A-20: Reaction force at the right arm expressed in the global frame for $(\alpha_1, \alpha_4) = \pm\, 20°$

The above graphs show all forces per arm, while the goal is to find something about the posture from the separate joints. Therefore the following figures visualize the forces acting on the separate joints in the global frame, refer Figures A-21 and A-22 for $(\alpha_1, \alpha_4) = (-0°, 0°)$.
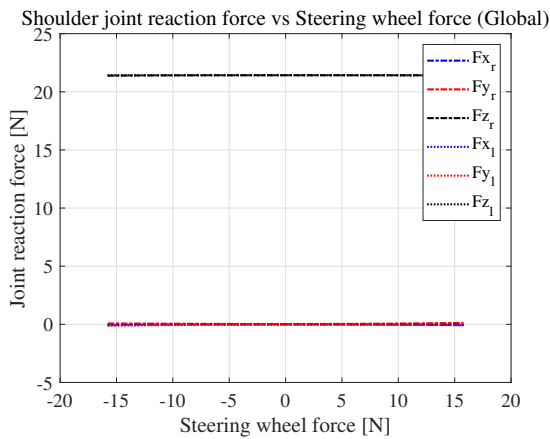
Figure A-21: Shoulder reaction force over steering wheel angle expressed in the global frame for $(\alpha_1, \alpha_4) = \pm\, 0°$
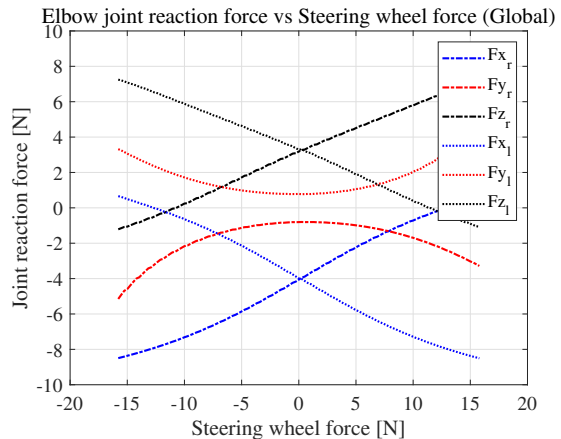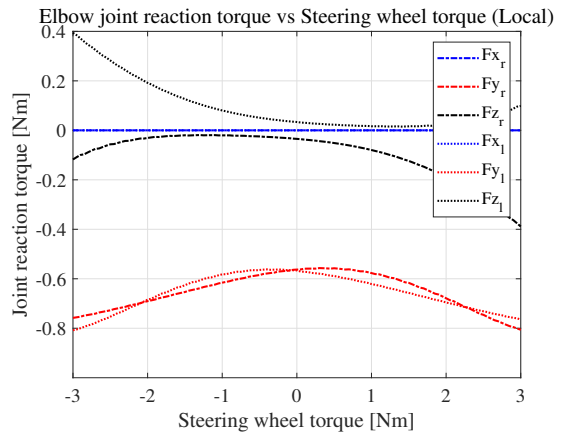
Figure A-22: Elbow reaction force over steering wheel angle expressed in the global frame for $(\alpha_1, \alpha_4) = \pm\, 0°$

Figures A-23 and A-24 show the reaction forces on each joint for shoulders fixed to $(\alpha_1, \alpha_4) = (-10°, 10°)$.
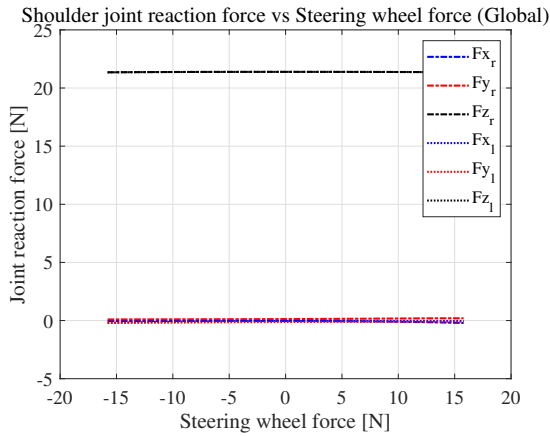
Figure A-23: Shoulder reaction force over steering wheel angle expressed in the global frame for $(\alpha_1, \alpha_4) = \pm 10°$
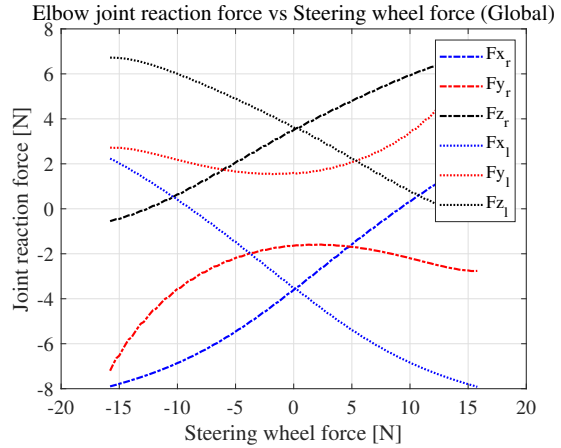
Figure A-24: Elbow reaction force over steering wheel angle expressed in the global frame for $(\alpha_1, \alpha_4) = \pm 10°$

Figures A-25 and A-26 show the reaction forces on each joint for shoulders fixed to (α_1, α_4) = (-20°, 20°).
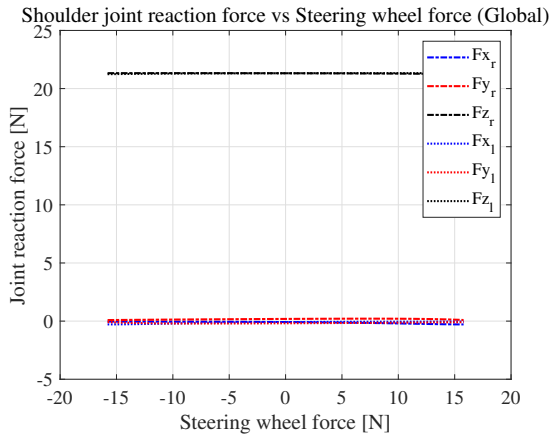
Figure A-25: Shoulder reaction force over steering wheel angle expressed in the global frame for $(\alpha_1, \alpha_4) = \pm 20°$
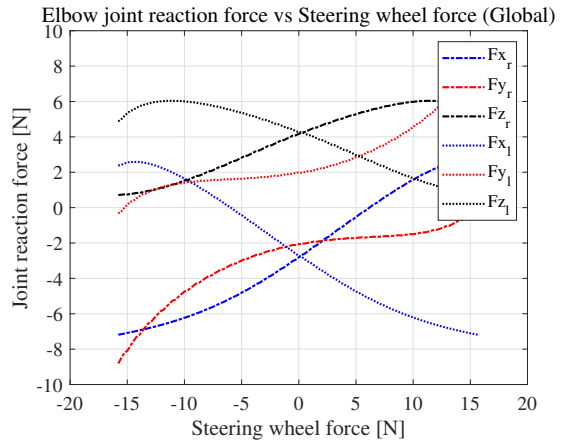
Figure A-26: Elbow reaction force over steering wheel angle expressed in the global frame for $(\alpha_1, \alpha_4) = \pm 20°$

The joint torques, calculated using the moment arms from the CoM of the body to the accompanying joint, are visualized in Figures A-27 and A-28 for $(\alpha_1, \alpha_4) = (-0°, 0°)$. These torques are rotated so they are expressed in the local frames of respectively the upper arm and the forearm.
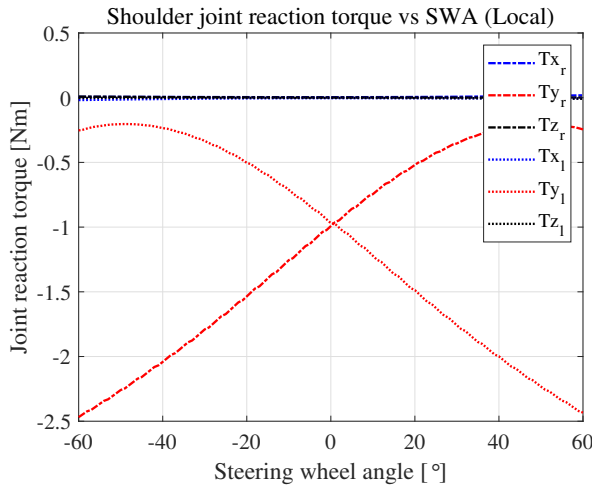
Figure A-27: Shoulder reaction torque over steering wheel angle expressed in the local upper arm frame for $(\alpha_1, \alpha_4) = \pm\ 0°$
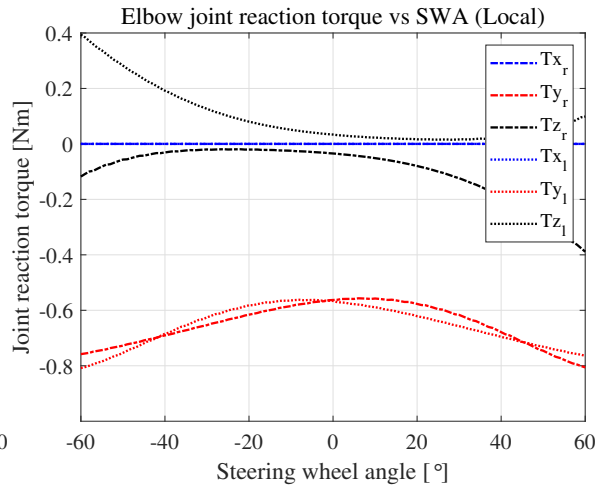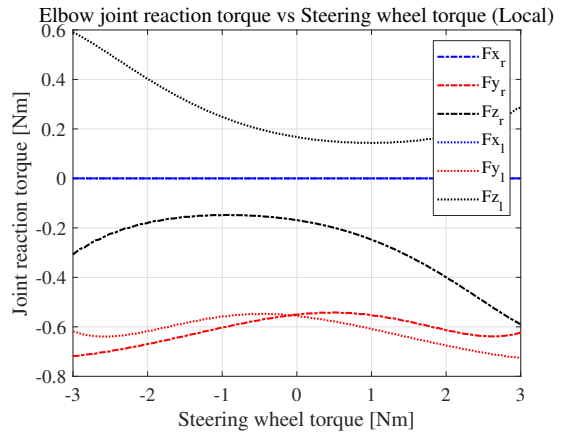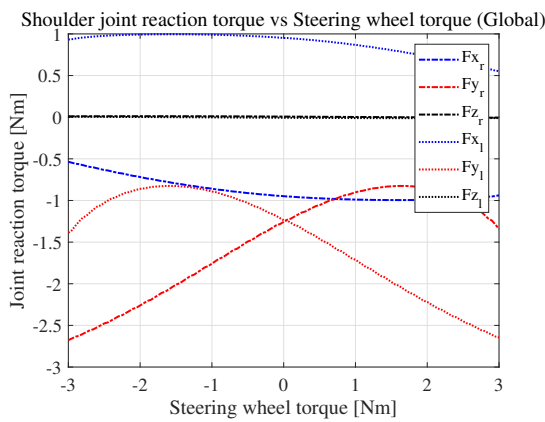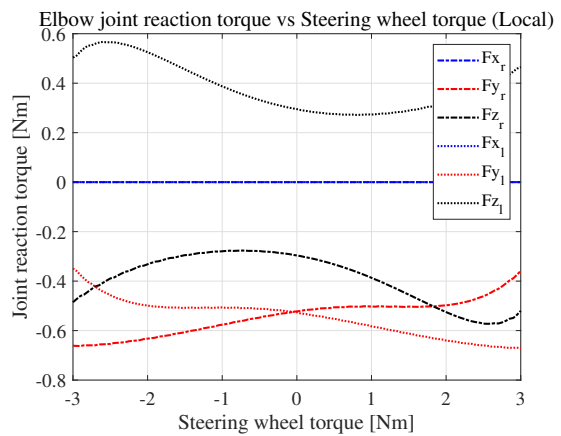

Figure A-28: Elbow reaction torque over steering wheel angle expressed in the local forearm frame for $(\alpha_1, \alpha_4) = \pm\ 0°$

Figures A-29 and A-30 visualize the joint reaction torques on each joint for shoulders fixed to $(\alpha_1, \alpha_4) = (-10°, 10°)$.
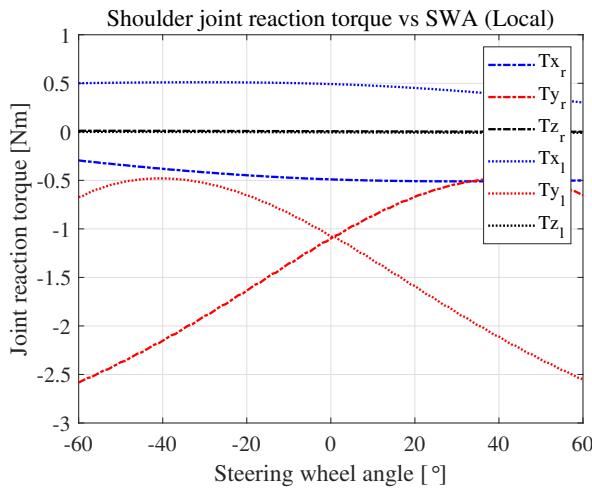
Figure A-29: Shoulder reaction torque over steering wheel angle expressed in the local upper arm frame for $(\alpha_1, \alpha_4) = \pm\ 10°$
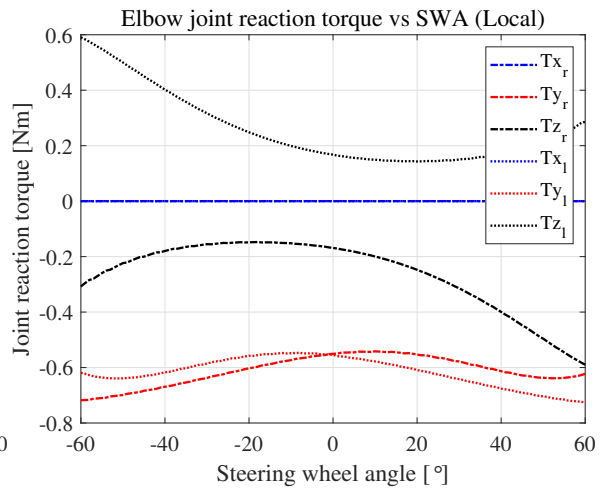
Figure A-30: Elbow reaction torque over steering wheel angle expressed in the local forearm frame for $(\alpha_1, \alpha_4) = \pm\ 10°$

Figures A-31 and A-32 visualize the joint reaction torques on each joint for shoulders fixed to $(\alpha_1, \alpha_4) = (-20°, 20°)$.
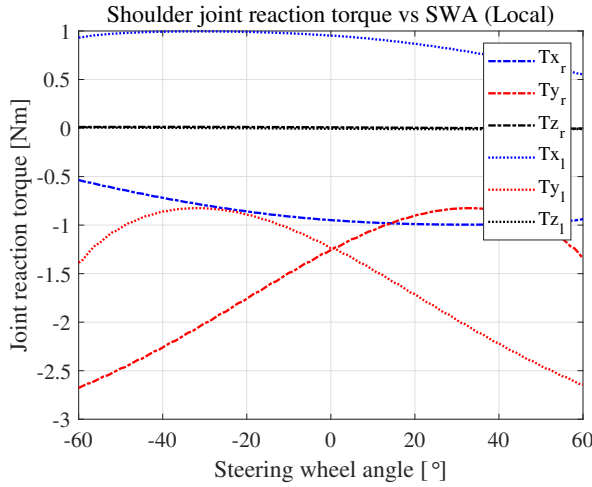
Figure A-31: Shoulder reaction torque over steering wheel angle expressed in the local upper arm frame for $(\alpha_1, \alpha_4) = \pm\ 20°$
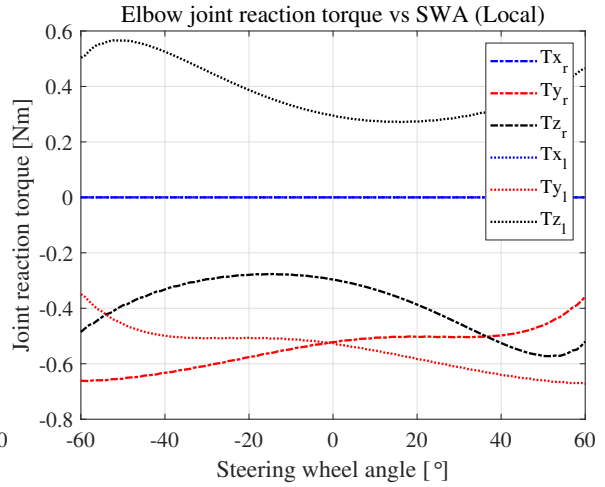
Figure A-32: Elbow reaction torque over steering wheel angle expressed in the local forearm frame for $(\alpha_1, \alpha_4) = \pm\ 20°$

Using the applied steering wheel torque from Appendix A-4, the relation between joint reaction torque M_j and applied steering wheel torque M_{str} is calculated. This is visualized in Figures A-33 and A-34 for $(\alpha_1, \alpha_4) = (\text{-}0°, 0°)$.
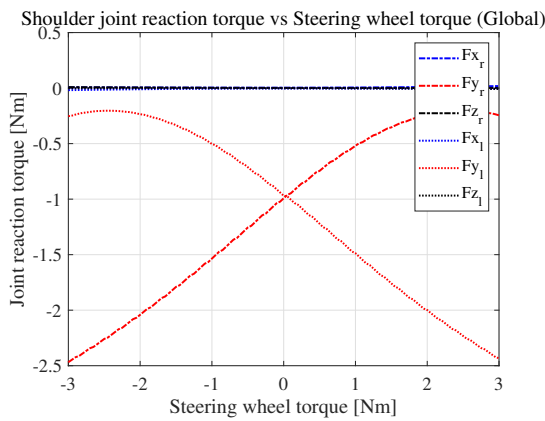
Figure A-33: Shoulder reaction torque over steering wheel torque expressed in the local upper arm frame for $(\alpha_1, \alpha_4) = \pm\ 0°$

Figure A-34: Elbow reaction torque over steering wheel torque expressed in the global frame for $(\alpha_1, \alpha_4) = \pm\ 0°$

Figures A-35 and A-36 visualize the joint reaction torques over steering wheel torque on each joint for shoulders fixed to $(\alpha_1, \alpha_4) = (\text{-}10°, 10°)$.
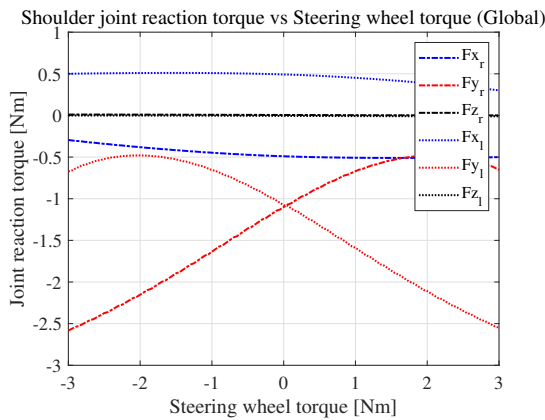
Figure A-35: Shoulder reaction torque over steering wheel torque expressed in the local upper arm frame for $(\alpha_1,\alpha_4) = \pm\ 10°$

Figure A-36: Elbow reaction torque over steering wheel torque expressed in the global frame for $(\alpha_1,\alpha_4) = \pm\ 10°$

Figures A-37 and A-38 visualize the joint reaction torques over steering wheel torque on each joint for shoulders fixed to $(\alpha_1,\alpha_4) = (-20°, 20°)$.

Figure A-37: Shoulder reaction torque over steering wheel torque expressed in the local upper arm frame for $(\alpha_1,\alpha_4) = \pm\ 20°$

Figure A-38: Elbow reaction torque over steering wheel torque expressed in the global frame for $(\alpha_1,\alpha_4) = \pm\ 20°$

The shoulder joint reaction torque has the same magnitude for the global and the local upper arm frame as the shoulder is fixed at the end of body 1 which is fixed to the origin. Therefore it does not make a difference if the shoulder joint torque is expressed in the local or global coordinate frame. The joint torques M_j over joint angles ϕ_j are calculated using the angles from Appendix A-6, and can be seen in Figures A-39 and A-40 for shoulders fixed to $(\alpha_1,\alpha_4) = (-0°, 0°)$.
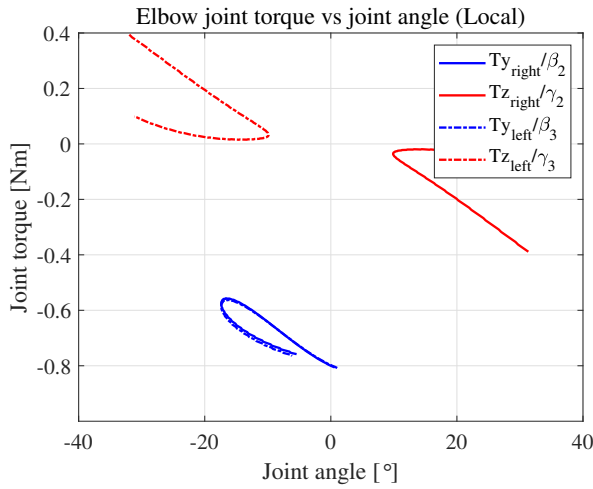
Figure A-39: Elbow reaction torque over joint angle expressed in the local upper arm frame for $(\alpha_1, \alpha_4) = \pm\ 0°$
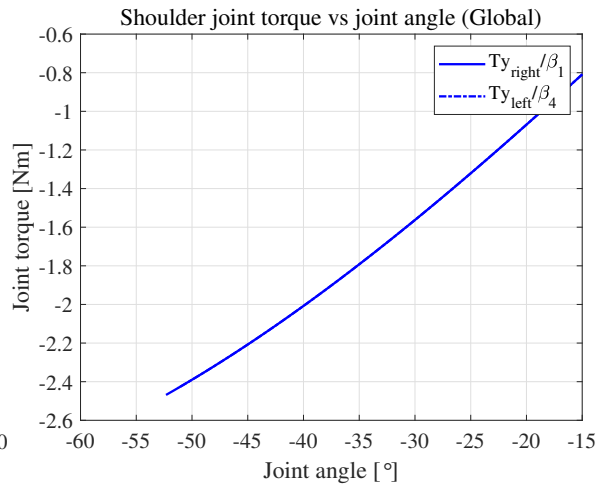
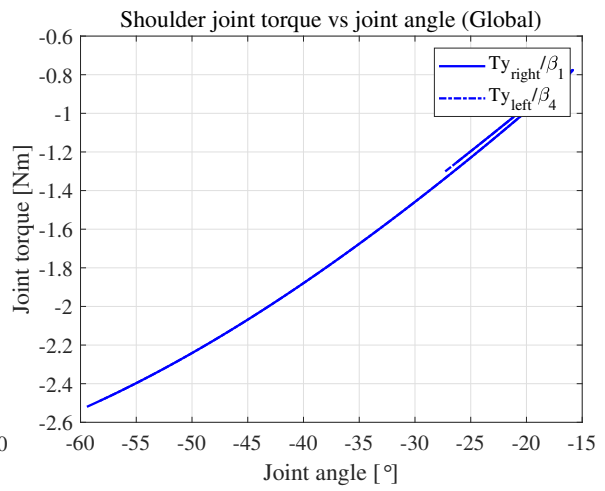**Figure A-40:** Shoulder reaction torque over joint angle expressed in the global frame for $(\alpha_1, \alpha_4) = \pm\ 0°$

Figures A-41 and A-42 visualize the joint torques over joint angle on each joint for shoulders fixed to $(\alpha_1, \alpha_4) = (-10°,\ 10°)$.
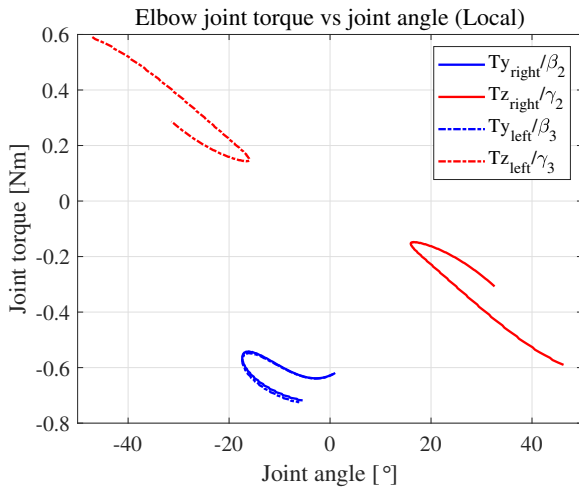
Figure A-41: Elbow reaction torque over joint angle expressed in the local upper arm frame for $(\alpha_1, \alpha_4) = \pm\ 10°$
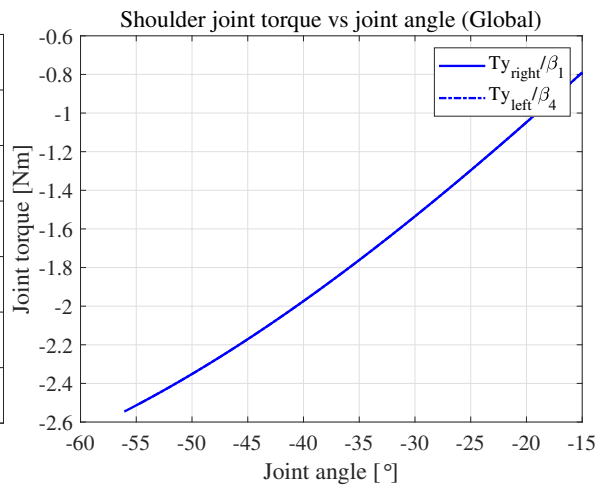
Figure A-42: Shoulder reaction torque over joint angle expressed in the global frame for $(\alpha_1, \alpha_4) = \pm\ 10°$

Figures A-43 and A-44 visualize the joint torques over joint angle on each joint for shoulders fixed to $(\alpha_1, \alpha_4) = (-20°,\ 20°)$.
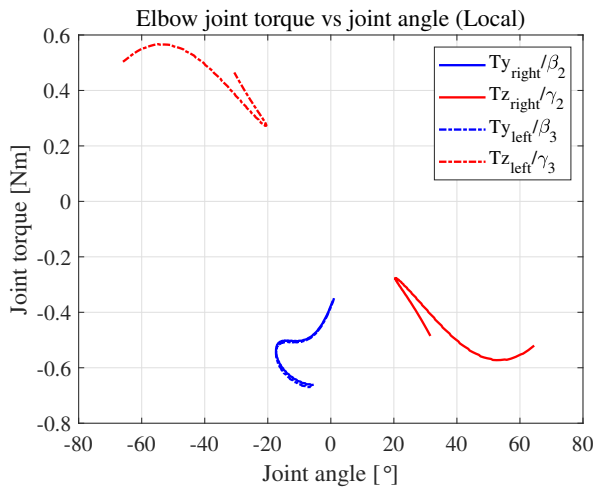
Figure A-43: Elbow reaction torque over joint angle expressed in the local upper arm frame for $(\alpha_1,\alpha_4) = \pm\,20°$

Figure A-44: Shoulder reaction torque over joint angle expressed in the global frame for $(\alpha_1,\alpha_4) = \pm\,20°$

These values are normalized as they are merely qualitatively comparable to the experiment results. Therefore the rate of change in joint torque can be investigated over steering wheel angle (Figures A-45 and A-46) for $(\alpha_1,\alpha_4) = (\text{-}0°, 0°)$.
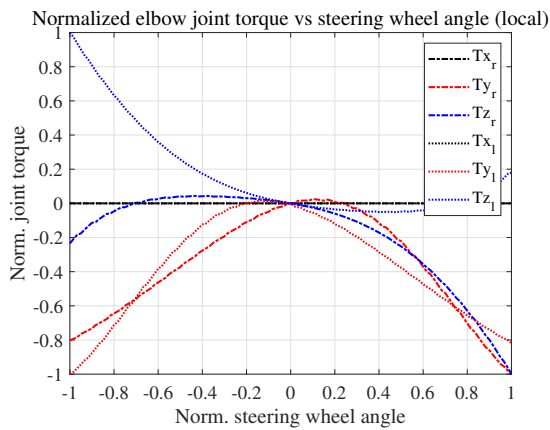
Figure A-45: Normalized elbow joint torque over normalized steering wheel angle for $(\alpha_1,\alpha_4) = \pm\,0°$
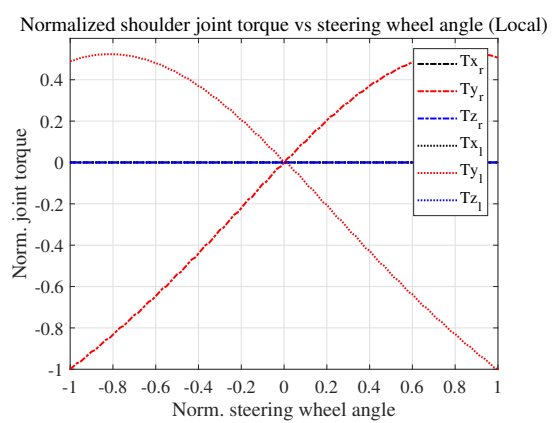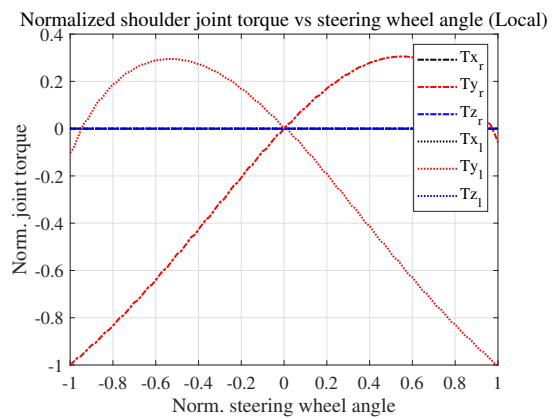
Figure A-46: Normalized shoulder joint torque over normalized steering wheel angle for $(\alpha_1,\alpha_4) = \pm\,0°$

The rate of change in joint torque over steering wheel angle is shown below in Figures A-47 and A-48 for $(\alpha_1,\alpha_4) = (\text{-}10°, 10°)$.

Normalized elbow joint torque vs steering wheel angle (local)

Normalized shoulder joint torque vs steering wheel angle (Local)
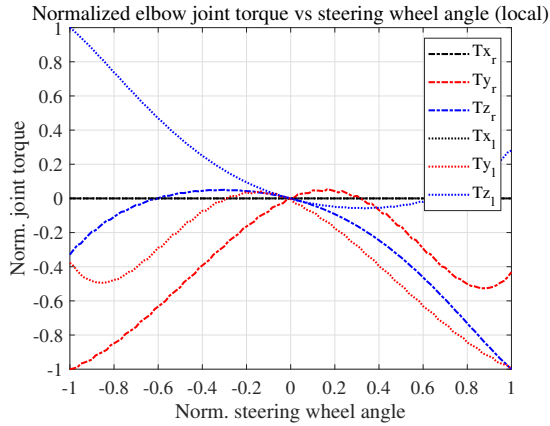
Figure A-47: Normalized elbow joint torque over normalized steering wheel angle for $(\alpha_1, \alpha_4) = \pm 10°$
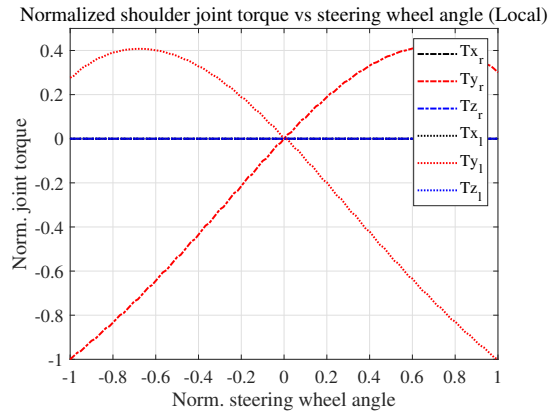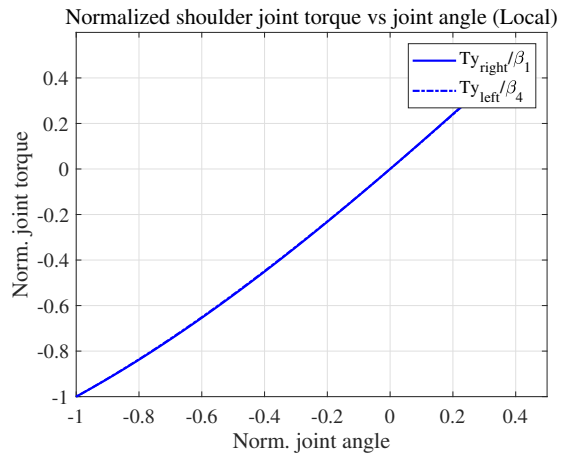
Figure A-48: Normalized shoulder joint torque over normalized steering wheel angle for $(\alpha_1, \alpha_4) = \pm 10°$

The rate of change in joint torque over steering wheel angle is shown below in Figures A-49 and A-50 for $(\alpha_1, \alpha_4) = (-20°, 20°)$.

Normalized elbow joint torque vs steering wheel angle (local)

Normalized shoulder joint torque vs steering wheel angle (Local)
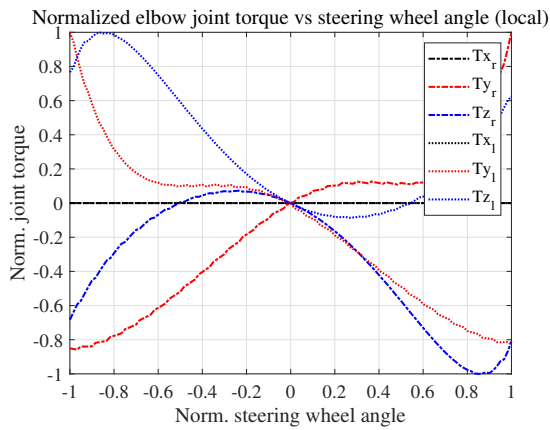
Figure A-49: Normalized elbow joint torque over normalized steering wheel angle for $(\alpha_1, \alpha_4) = \pm 20°$

Figure A-50: Normalized shoulder joint torque over normalized steering wheel angle for $(\alpha_1, \alpha_4) = \pm 20°$

The rate of change in joint torque was calculated and visualized over joint angle (Figures A-51 and A-52) for $(\alpha_1, \alpha_4) = (-0°, 0°)$.

Normalized elbow joint torque vs joint angle (Local)
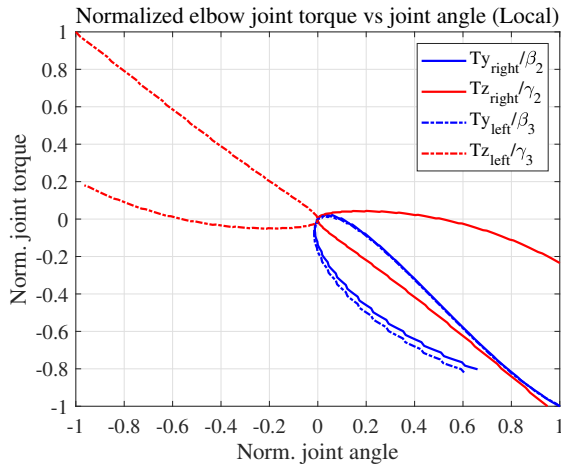
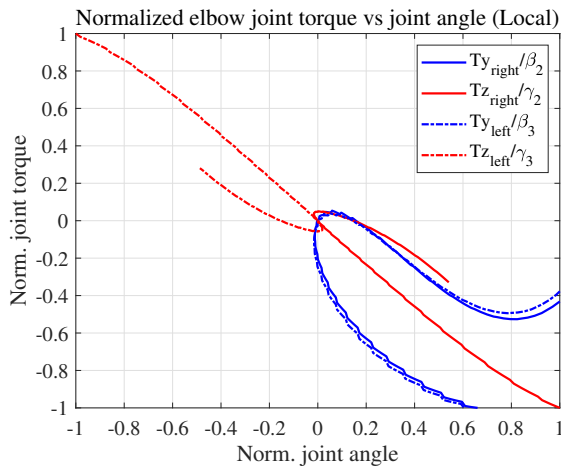**Figure A-51:** Normalized elbow joint torque over normalized joint angle for $(\alpha_1, \alpha_4) = \pm\, 0°$
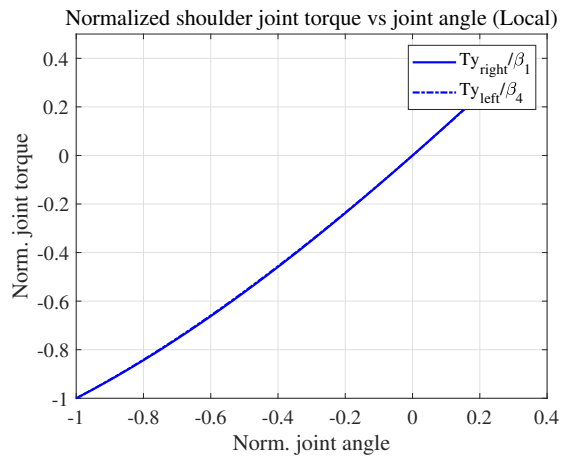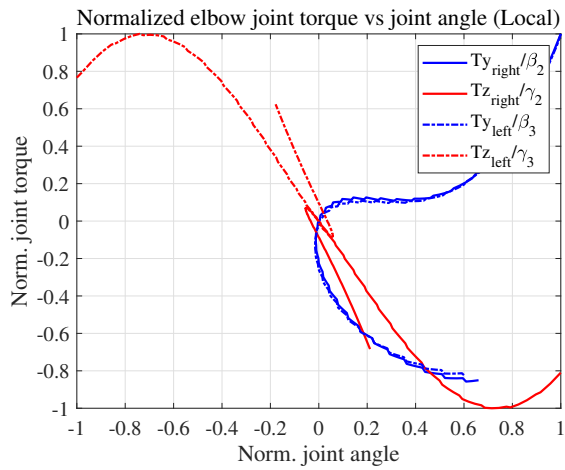
Normalized shoulder joint torque vs joint angle (Local)

Figure A-52: Normalized shoulder joint torque over normalized joint angle for $(\alpha_1, \alpha_4) = \pm\, 0°$

The rate of change in joint torque over joint angle is shown below in Figures A-53 and A-54 for $(\alpha_1, \alpha_4) = (-10°, 10°)$.

Normalized elbow joint torque vs joint angle (Local)

Figure A-53: Normalized elbow joint torque over normalized joint angle for $(\alpha_1, \alpha_4) = \pm\, 10°$

Normalized shoulder joint torque vs joint angle (Local)

Figure A-54: Normalized shoulder joint torque over normalized joint angle for $(\alpha_1, \alpha_4) = \pm\, 10°$

The rate of change in joint torque over joint angle is shown below in Figures A-55 and A-56 for $(\alpha_1, \alpha_4) = (-20°, 20°)$.

Figure A-55: Normalized elbow joint torque over normalized joint angle for $(\alpha_1, \alpha_4) = \pm\,20°$
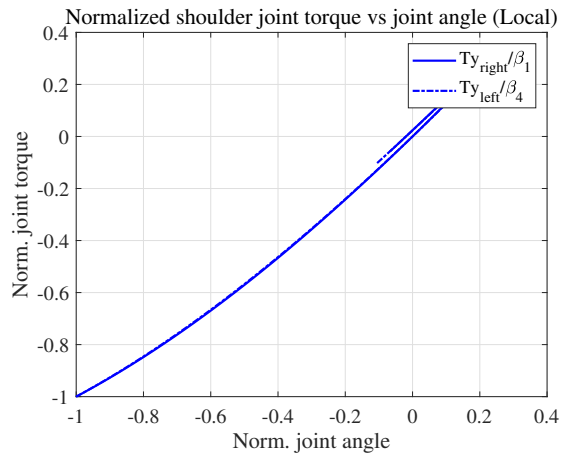

Figure A-56: Normalized shoulder joint torque over normalized joint angle for $(\alpha_1, \alpha_4) = \pm\,20°$

Appendix B

Experimental investigation

This chapter contains more detailed information about the experimental investigation and the accompanying results. The first experiment compares driving posture for varying steering wheel angles, estimating the musculoskeletal arm admittance parameters (J_{arm}, b_{arm} & c_{arm}). The goal of the second experiment is to analyze changes in muscle activity during a low frequency sinus motion applied to the steering wheel by the driver. The vitaport (i.e. EMG activity) and torque sensor data is shown for both experiments.

B-1 Vitaport EMG activity data

This section contains the EMG activity data as well as some more elaborate results graphs. All EMG electrodes were placed according to SENIAM standards. The measured currents were recorded by Vitaport using eight channels. The four measured muscles are listed in Table B-1 below, including their functionalities for the left arm and their corresponding channels.

Table B-1: Measured muscles and their functionalities [32]

Muscle name	Location	Functionality left arm	Channel #
Biceps Brachii (BB)	Upper arm	Aids in steering left	1 (L) 2 (R)
Flexor Carpi Radialis (FC)	Lower arm	Gripping the wheel	3 (L) 4 (R)
Deltoideus Anterior (DA)	Front shoulder	Aids in steering right	5 (L) 6 (R)
Deltoideus Posterior (DP)	Back shoulder	Aids in steering right	7 (L) 8 (R)

B-1-1 Experiment 1: Position task for varying steering wheel angles

The first experiment includes a position task in which the participant tries to maintain the same angular position for the entire measurement. This way, driving posture can be compared for varying steering wheel angles. The disturbance signal is a sinus sweep (input) signal as

can be seen in Figure B-1. The signal was applied by exciting the motor and the maximum torque was set to 1 Nm and the signal is linearly increasing from 0.1 to 20 Hz.
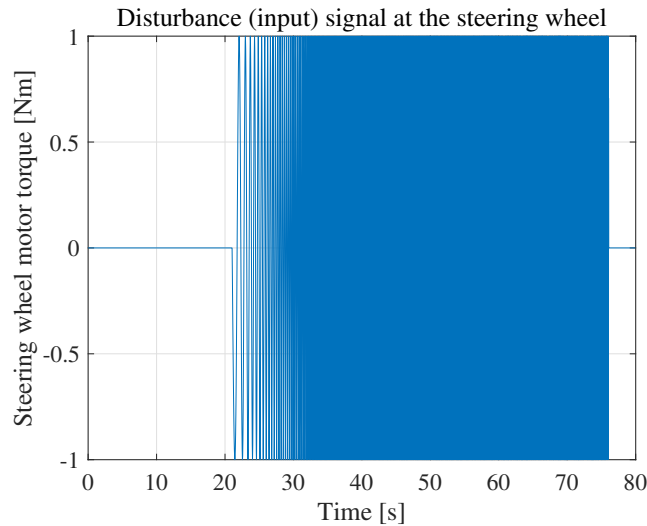

Figure B-1: Disturbance (input) signal consisting of a frequency sweep with a steering wheel torque of 1 Nm

The EMG activity remains relatively constant over time. However, there is measurement noise and some low frequency drift involved, as can be seen in Figures B-2, B-3 and B-4 for SWA positions equal to respectively 0°, 45° and 90°. The raw data is filtered using a low-pass butterworth filter.
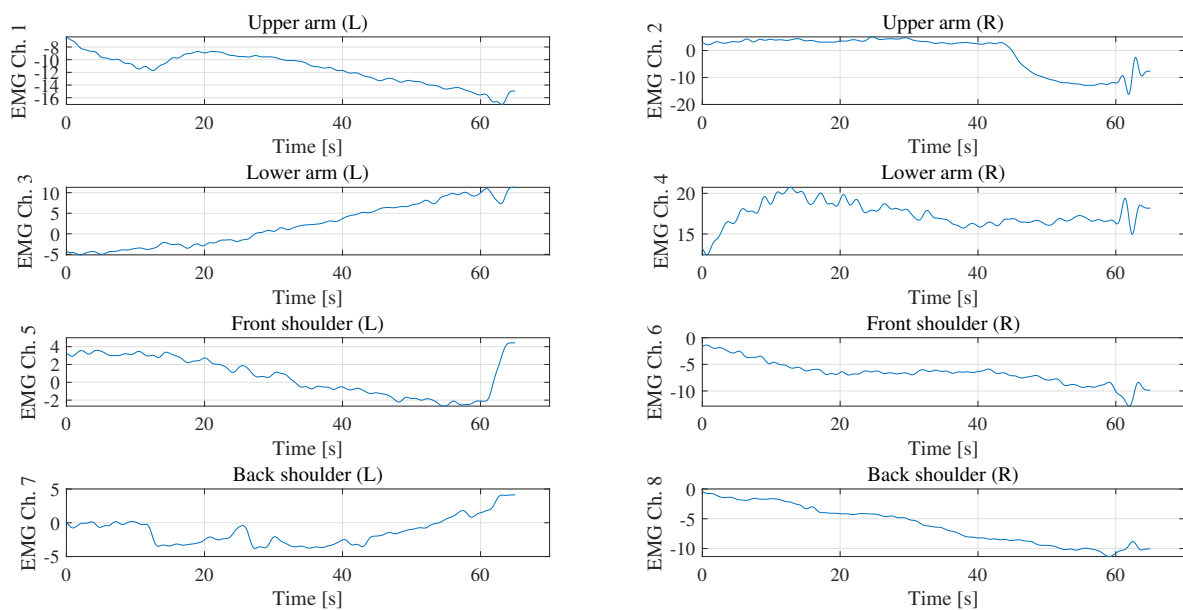
Figure B-2: EMG activity of all four measured muscles for both left and right arm over time for SWA = 0°

EMG activity of all four measured muscles for both arms over time (SWA = 45°)
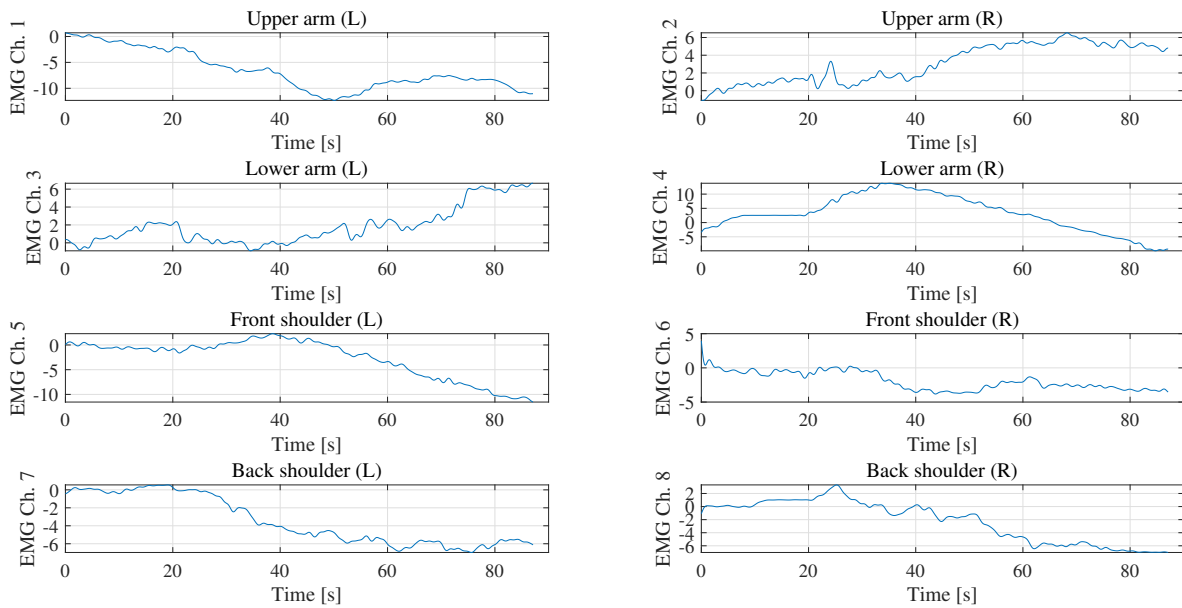
Figure B-3: EMG activity of all four measured muscles for both left and right arm over time for SWA = 45°

EMG activity of all four measured muscles for both arms over time (SWA = 90°)
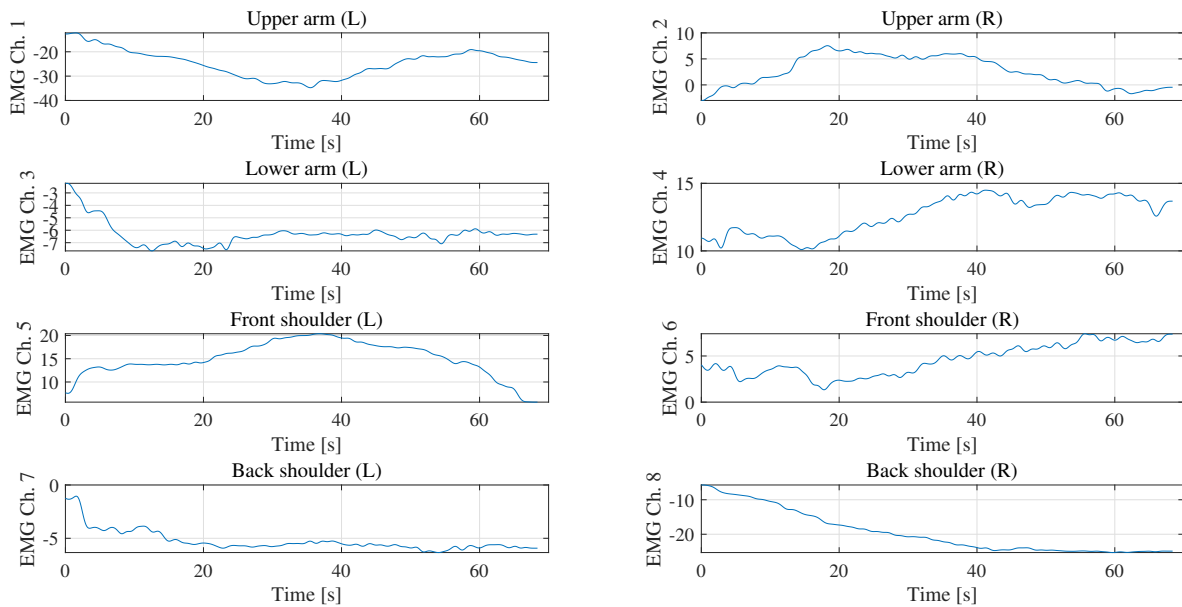

Figure B-4: EMG activity of all four measured muscles for both left and right arm over time for SWA = 90°

In an attempt to compare the various steering wheel angular positions, the bar chart of Figure B-5 was constructed. The maximum contraction during steering is used for each muscle to get to the relative muscle activity.
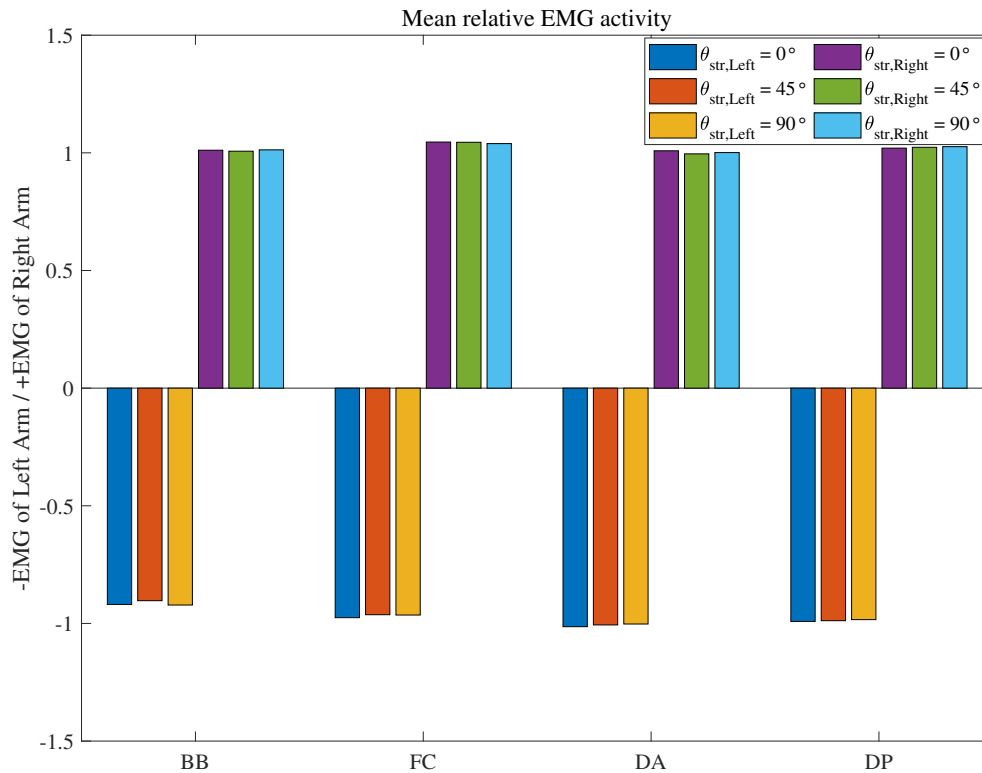
Figure B-5: Mean relative EMG activity of all four measured muscles for both left and right arm for the various steering wheel angular positions

As can be seen from Figure B-5, there is no notable difference in relative EMG activity when comparing the average relative muscle contraction. In order to conclude on experiment 1, the torque sensor data in appendix B-2 should be analyzed.

B-1-2   Experiment 2: Sinus motion applied by driver

During the second experiment, the driver applies a low frequency sinus motion on the steering wheel and therefore the different muscles are actuated and the EMG activity varies over time, refer Figure B-6.
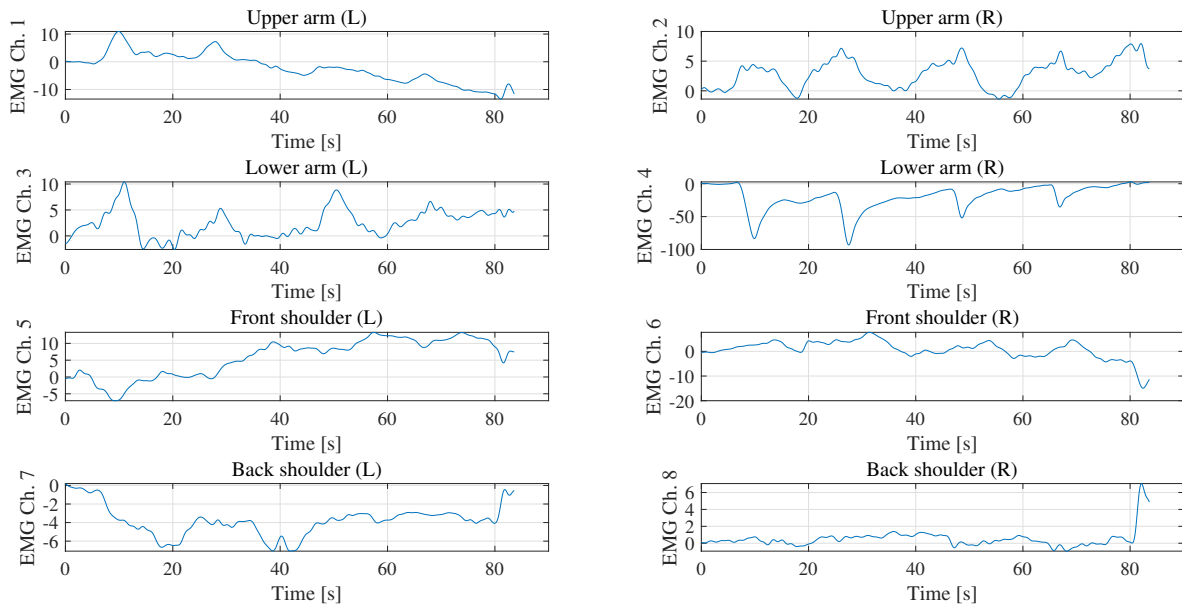
Figure B-6: EMG activity of all four measured muscles for both left and right arm over time

The EMG signals of all separate muscles are visualized as well as the normalized version of each signal over normalized steering wheel torque and normalized steering wheel angle. The BB (i.e. upper arm) muscle results are visualized in Figure B-7.
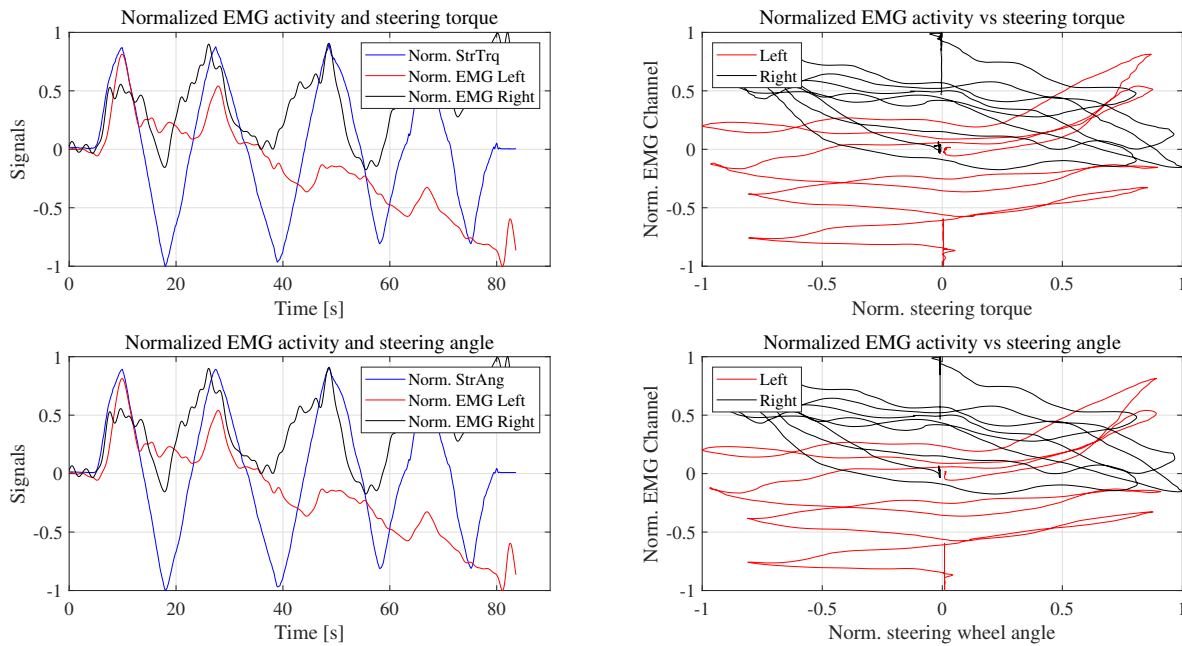

Figure B-7: EMG activity, steering torque and steering angle BB muscle (i.e. upper arm) over time, SWA and steering torque

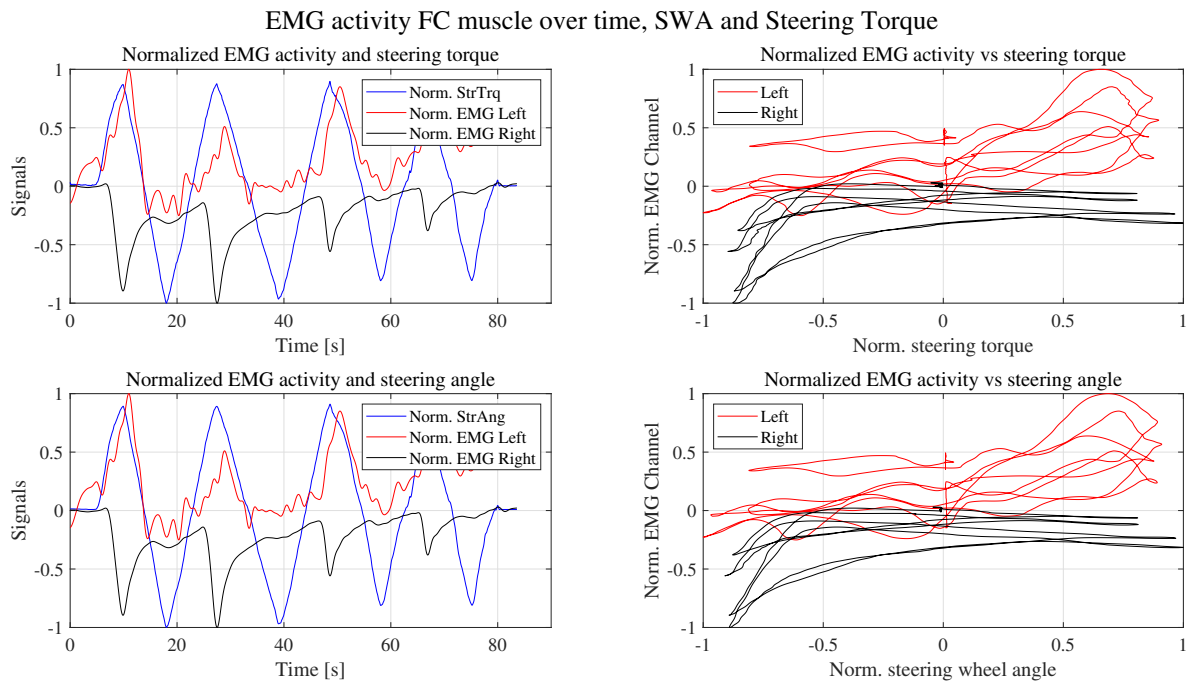The FC (i.e. lower arm) muscle results are visualized in Figure B-8.

EMG activity FC muscle over time, SWA and Steering Torque

Figure B-8: EMG activity, steering torque and steering angle FC muscle (i.e. lower arm) over time, SWA and steering torque

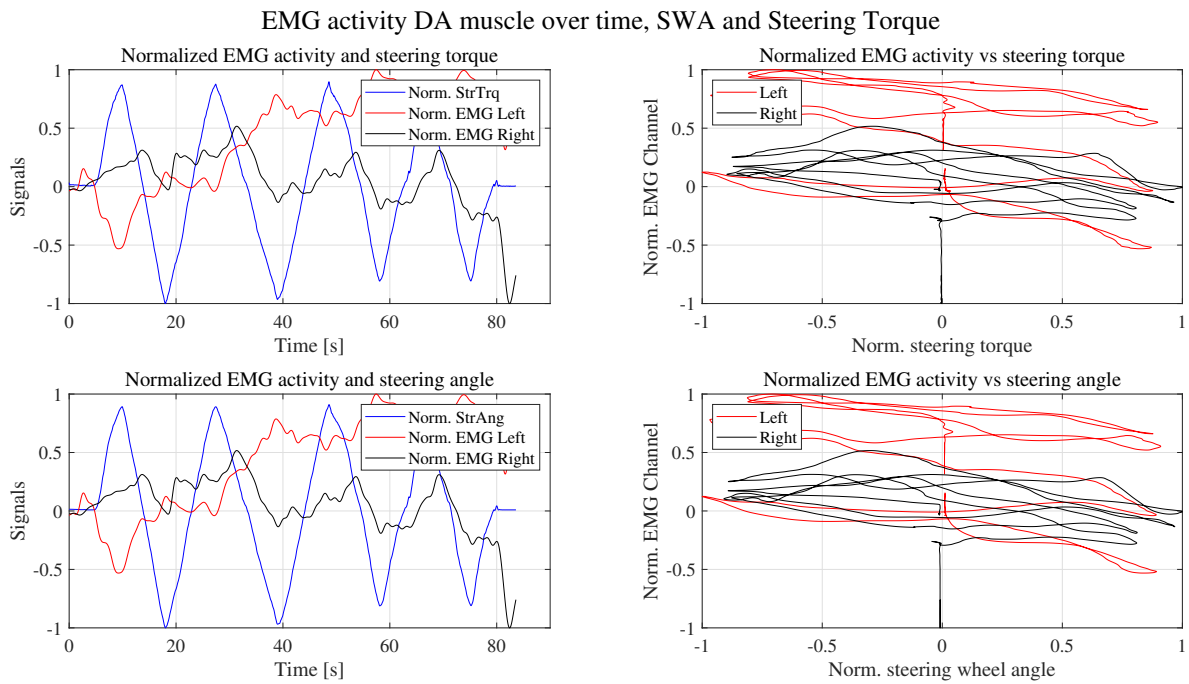The DA (i.e. front shoulder) muscle results are visualized in Figure B-9.

Figure B-9: EMG activity, steering torque and steering angle DA muscle (i.e. front shoulder) over time, SWA and steering torque

The DP (i.e. back shoulder) muscle results are visualized in Figure B-10.
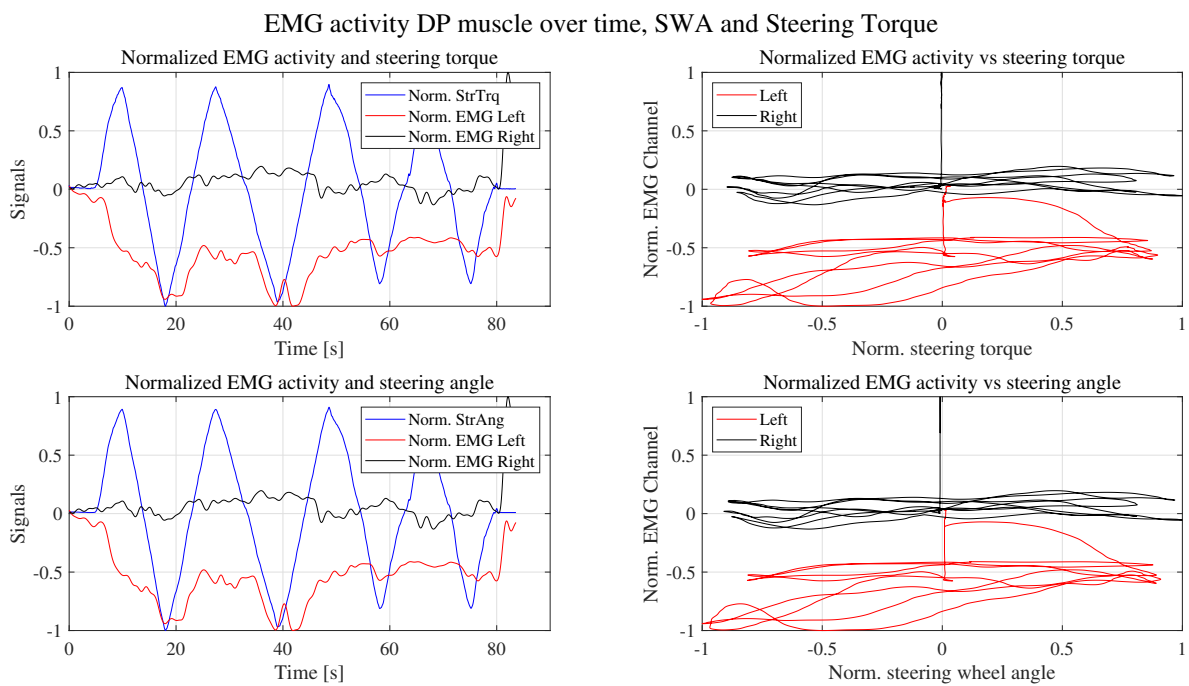

Figure B-10: EMG activity, steering torque and steering angle DP muscle (i.e. back shoulder) over time, SWA and steering torque

The elbow and shoulder EMG activity over joint angles is calculated using the model results for the joint angles for every SWA. These results are really noisy and go up to a steering wheel angle of 60° as this is the model limit, refer Figures B-11 and B-12. The results are normalized for qualitative comparison purposes.
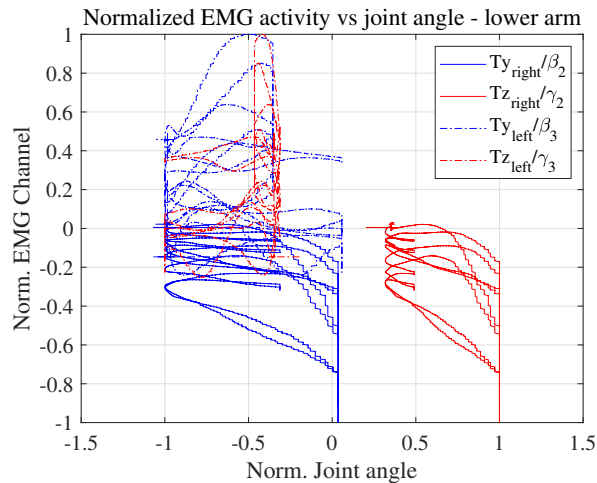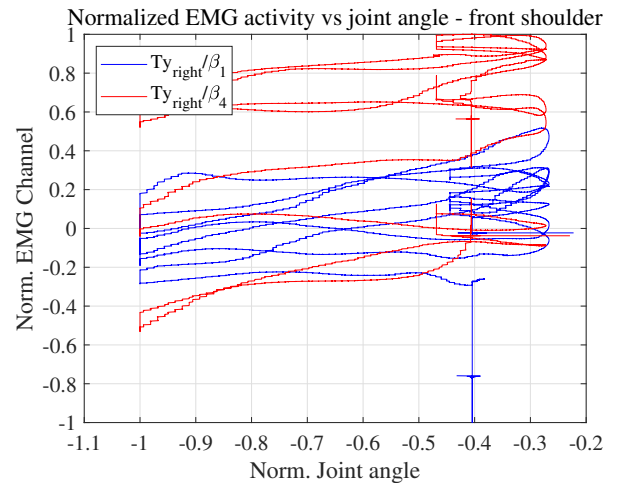

Figure B-11: elbow joint

Figure B-12: shoulder joint

B-2   Torque sensor data

This section contains the Frequency Response Function for measured torque sensor data from experiment 1. This is the experiment involving the position task for varying steering wheel angles.

B-2-1   FRF results measurement 1

The FRF results from measurement 1 involving participant 1 are shown in Figures B-13 and B-14 for positive SWA (anti-clockwise) and Figures B-15 and B-16 for negative SWA (clockwise).
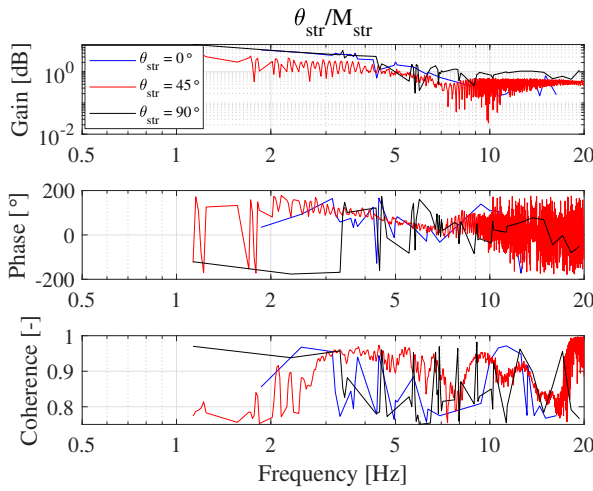
Figure B-13: Measured FRF for three steering angular positions (0°; 45° and 90°) from steering wheel angle to steering torque.

Figure B-14: Measured FRF for three steering angular positions (0°; 45° and 90°) from steering angular speed to steering torque.

Figure B-15: Measured FRF for three steering angular positions (0°; -45° and -90°) from steering wheel angle to steering torque.

Figure B-16: Measured FRF for three steering angular positions (0°; -45° and -90°) from steering angular speed to steering torque.

B-2-2 FRF results measurement 2

The FRF results from measurement 2 involving participant 2 are shown in Figures B-17 and B-18 for positive SWA (anti-clockwise) and Figures B-19 and B-20 for negative SWA (clockwise).

Figure B-17: Measured FRF for three steering angular positions (0°; 45° and 90°) from steering wheel angle to steering torque.
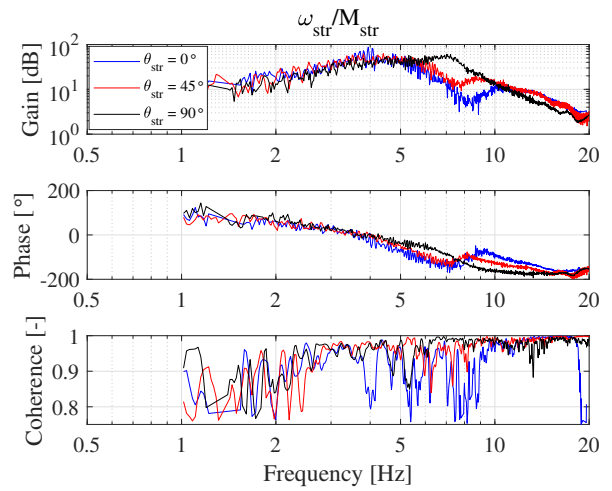

Figure B-18: Measured FRF for three steering angular positions (0°; 45° and 90°) from steering angular speed to steering torque.
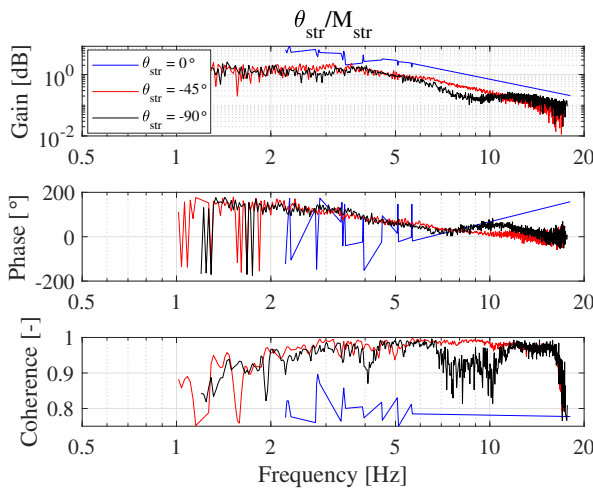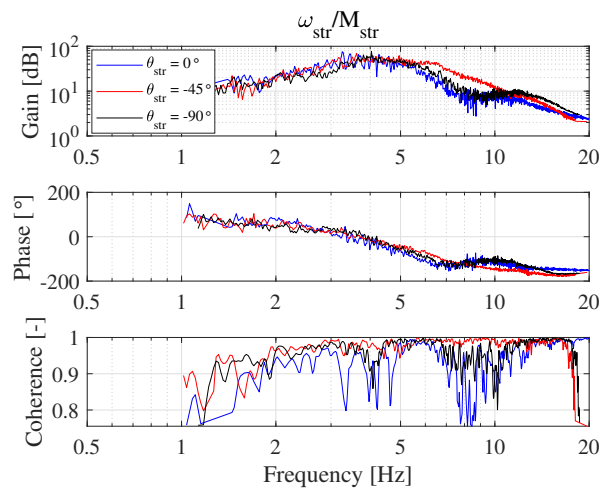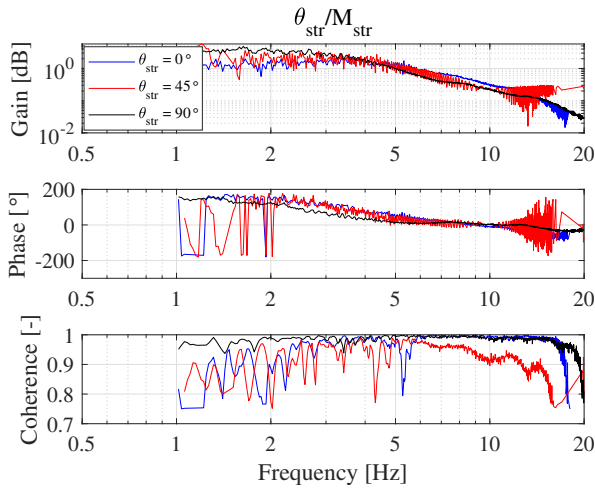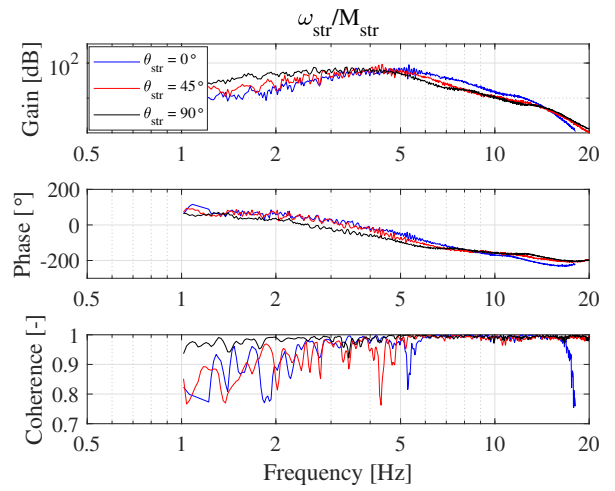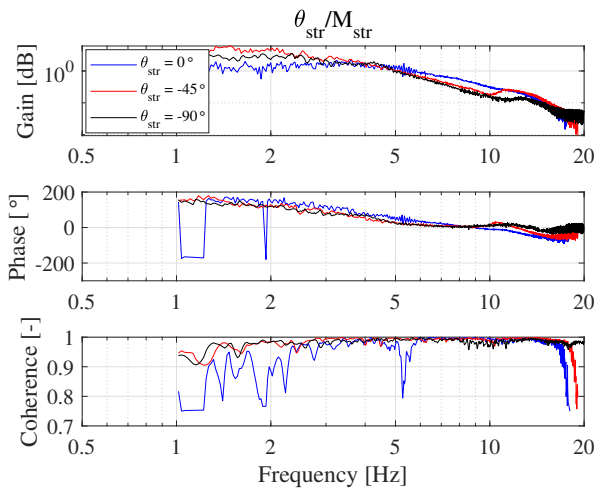

Figure B-19: Measured FRF for three steering angular positions (0°; -45° and -90°) from steering wheel angle to steering torque.
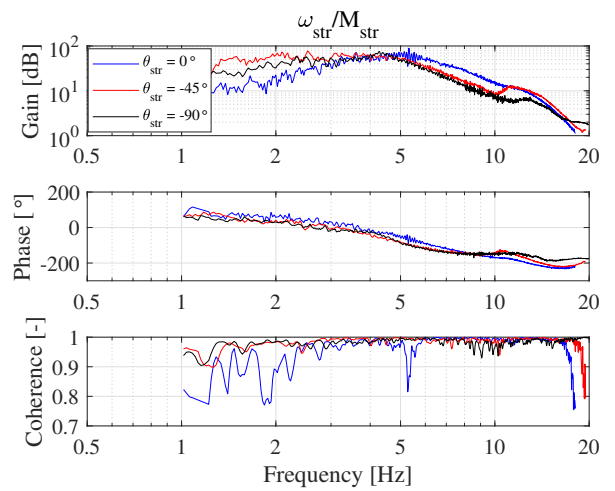

Figure B-20: Measured FRF for three steering angular positions (0°; -45° and -90°) from steering angular speed to steering torque.

Bibliography

[1] T. Chugh, "Haptic feedback control methods for steering systems," *Chalmers University of Technology*, 2019.

[2] B. Shyrokau, "Lecture slides me41100 vehicle dynamics a: Steering assist, steering feel and assessment," 2019.

[3] T. Takamatsu and T. Tomita, "Parameter design and tuning tools for electric power steering system," *KOYO engineering journal No165E*, pp. 49–53, 2004.

[4] H. Wolf, "Untersuchung des lenkgefühls von personenkraftwagen unter besonderer berücksichtigung ergonomischer erkenntnisse und methoden," *Technische Universität München, Diss*, 2008.

[5] T. P. Witsenboer, "Influence of steering system imperfections on truck steering feel," Master's thesis, Delft University of Technology, 2015.

[6] D. G. Farrer, "An objective measurement technique for the quantification of on-centre handling quality," SAE Technical Paper, Tech. Rep., 1993.

[7] C. Zong, Z. Zhang, L. Mai, C. Wang, and Z. Wu, "Study on objective evaluation index system of on-center handling for passenger car," SAE Technical Paper, Tech. Rep., 2013.

[8] C. G. Fernandes, L. Passos, K. P. de Mello, and E. Peres, "A new approach to improve steering response development using bode diagrams," SAE Technical Paper, Tech. Rep., 2007.

[9] S. Amberkar, F. Bolourchi, J. Demerly, and S. Millsap, "A control system methodology for steer by wire systems," SAE technical paper, Tech. Rep., 2004.

[10] T. Sezer, "Electric power steering: recreating steering feel," Master's thesis, Delft University of Technology, 2015.

[11] M. Nybacka, X. He, G. Gómez, E. Bakker, and L. Drugge, "Links between subjective assessments and objective metrics for steering," *International Journal of Automotive Technology*, vol. 15, no. 6, pp. 893–907, 2014.

[12] D. T. McRuer and H. R. Jex, "A review of quasi-linear pilot models," *IEEE transactions on human factors in electronics*, no. 3, pp. 231–249, 1967.

[13] M. Kondo and A. Ajimine, "Driver's sight point and dynamics of the driver-vehicle-system related to it," SAE Technical Paper, Tech. Rep., 1968.

[14] O. Benderius, "Driver modeling: Data collection, model analysis, and optimization," 2012.

[15] G. Markkula, O. Benderius, K. Wolff, and M. Wahde, "A review of near-collision driver behavior models," *Human factors*, vol. 54, no. 6, pp. 1117–1143, 2012.

[16] S. Kolekar, W. Mugge, and D. Abbink, "Modeling intradriver steering variability based on sensorimotor control theories," *IEEE Transactions on Human-Machine Systems*, vol. 48, no. 3, pp. 291–303, 2018.

[17] G. Markkula, "Modeling driver control behavior in both routine and near-accident driving," in *Proceedings of the human factors and ergonomics society annual meeting*, vol. 58, no. 1.   SAGE Publications Sage CA: Los Angeles, CA, 2014, pp. 879–883.

[18] A. Pick and D. J. Cole, "Dynamic properties of a driver's arms holding a steering wheel," *Proceedings of the Institution of Mechanical Engineers, Part D: Journal of Automobile Engineering*, vol. 221, no. 12, pp. 1475–1486, 2007.

[19] M. Mulder, D. M. Pool, D. A. Abbink, E. R. Boer, P. M. Zaal, F. M. Drop, K. van der El, and M. M. van Paassen, "Manual control cybernetics: State-of-the-art and current trends," *IEEE Transactions on Human-Machine Systems*, vol. 48, no. 5, pp. 468–485, 2017.

[20] J. Rasmussen, "Skills, rules, and knowledge; signals, signs, and symbols, and other distinctions in human performance models," *IEEE transactions on systems, man, and cybernetics*, no. 3, pp. 257–266, 1983.

[21] C. C. MacAdam, "An optimal preview control for linear systems," *ASME-Journal of Dynamic Systems, Measurement and Control*, 1980.

[22] ——, "Development of a driver model for near/at-limit vehicle handling," *Transportation Research Institute (UMTRI)*, 2001.

[23] E. de Vlugt, A. C. Schouten, and F. C. van der Helm, "Closed-loop multivariable system identification for the characterization of the dynamic arm compliance using continuous force disturbances: a model study," *Journal of neuroscience methods*, vol. 122, no. 2, pp. 123–140, 2003.

[24] F. C. Van der Helm, A. C. Schouten, E. de Vlugt, and G. G. Brouwn, "Identification of intrinsic and reflexive components of human arm dynamics during postural control," *Journal of neuroscience methods*, vol. 119, no. 1, pp. 1–14, 2002.

[25] B. Carlsen. (2013, May) Kinesiology: Jargon. webpage. Jiu Jitsu. [Online]. Available: https://bicarlsen.wordpress.com/2013/05/27/kinesiology-background/

[26] K. R. Senior *et al.*, *Bone and Muscle: Structure, Force, and Motion.* The Rosen Publishing Group, Inc, 2010.

[27] A. Nikooyan, H. Veeger, P. Westerhoff, F. Graichen, G. Bergmann, and F. Van Der Helm, "Validation of the delft shoulder and elbow model using in-vivo glenohumeral joint contact forces," *Journal of biomechanics*, vol. 43, no. 15, pp. 3007–3014, 2010.

[28] J. Won and N. Hogan, "Stability properties of human reaching movements," *Experimental Brain Research*, vol. 107, no. 1, pp. 125–136, 1995.

[29] H. van der Kooij, B. Koopman, and F. C. van der Helm, "Human motion control," *Reader for Delft University course wb2407 and Twente University course*, vol. 115047, pp. 211–220, 2008.

[30] R. Shadmehr and F. A. Mussa-Ivaldi, "Adaptive representation of dynamics during learning of a motor task," *Journal of Neuroscience*, vol. 14, no. 5, pp. 3208–3224, 1994.

[31] A. A. Puzi, S. Sidek, and F. Sado, "Mechanical impedance modeling of human arm: A survey," in *IOP Conference Series: Materials Science and Engineering*, vol. 184, no. 1. IOP Publishing, 2017, p. 012041.

[32] D. A. Abbink, M. Mulder, and M. M. Van Paassen, "Measurements of muscle use during steering wheel manipulation," in *2011 IEEE International Conference on Systems, Man, and Cybernetics.* IEEE, 2011, pp. 1652–1657.

[33] D. Cole, "Neuromuscular dynamics and steering feel," *Proceedings of SteeringTech, TU Munich, Germany*, 2008.

[34] A. V. Hill, "The heat of shortening and the dynamic constants of muscle," *Proceedings of the Royal Society of London. Series B-Biological Sciences*, vol. 126, no. 843, pp. 136–195, 1938.

[35] J. Martins, E. Pires, R. Salvado, and P. Dinis, "A numerical model of passive and active behavior of skeletal muscles," *Computer methods in applied mechanics and engineering*, vol. 151, no. 3-4, pp. 419–433, 1998.

[36] D. J. Cole, "A path-following driver–vehicle model with neuromuscular dynamics, including measured and simulated responses to a step in steering angle overlay," *Vehicle system dynamics*, vol. 50, no. 4, pp. 573–596, 2012.

[37] A. J. Pick and D. J. Cole, "A mathematical model of driver steering control including neuromuscular dynamics," *Journal of Dynamic Systems, Measurement, and Control*, vol. 130, no. 3, p. 031004, 2008.

[38] W. Hoult, "A neuromuscular model for simulating driver steering torque," Ph.D. dissertation, University of Cambridge, 2009.

[39] W. Hoult and D. J. Cole, "A neuromuscular model featuring co-activation for use in driver simulation," *Vehicle System Dynamics*, vol. 46, no. S1, pp. 175–189, 2008.

[40] D. I. Katzourakis, D. A. Abbink, E. Velenis, E. Holweg, and R. Happee, "Driver's arms' time-variant neuromuscular admittance during real car test-track driving," *IEEE Transactions on Instrumentation and Measurement*, vol. 63, no. 1, pp. 221–230, 2013.

[41] C. Sentouh, P. Chevrel, F. Mars, and F. Claveau, "A human-centered approach of steering control modeling," in *Proceedings of the 21st IAVSD Symposium on Dynamics of Vehicles on Roads and Tracks, Stockholm, Sweden.* Citeseer, 2009, pp. 1–12.

[42] E. Donges, "A two-level model of driver steering behavior," *Human factors*, vol. 20, no. 6, pp. 691–707, 1978.

[43] E. De Vlugt, A. C. Schouten, and F. C. Van Der Helm, "Quantification of intrinsic and reflexive properties during multijoint arm posture," *Journal of neuroscience methods*, vol. 155, no. 2, pp. 328–349, 2006.

[44] D. A. Abbink, "Neuromuscular analysis of haptic gas pedal feedback during car following," 2006.

[45] C. Droogendijk, "A new neuromuscular driver model for steering system development," Master's thesis, Delft University of Technology, 2010.

[46] D. A. Abbink, M. Mulder, F. C. Van der Helm, M. Mulder, and E. R. Boer, "Measuring neuromuscular control dynamics during car following with continuous haptic feedback," *IEEE Transactions on Systems, Man, and Cybernetics, Part B (Cybernetics)*, vol. 41, no. 5, pp. 1239–1249, 2011.

[47] F. C. van der Helm, "A three-dimensional model of the shoulder and elbow," in *First Conference of the International Shoulder Group.* Shaker Publishing BV Delft, The Netherlands, 1997, pp. 65–70.

[48] J. Steen, H. J. Damveld, R. Happee, M. M. van Paassen, and M. Mulder, "A review of visual driver models for system identification purposes," in *2011 IEEE international conference on systems, man, and cybernetics.* IEEE, 2011, pp. 2093–2100.

[49] C. J. Nash, D. J. Cole, and R. S. Bigler, "A review of human sensory dynamics for application to models of driver steering and speed control," *Biological cybernetics*, vol. 110, no. 2-3, pp. 91–116, 2016.